Hybrid Nanostructured Materials

for Bioengineering Applications

By

Rui Wang

Dissertation

Submitted to the Faculty of the

Graduate School of Vanderbilt University

in partial fulfillment of the requirements

for the degree of

DOCTOR OF PHILOSOPHY

in

Physics

June 30, 2018

Nashville, Tennessee

Approved:

Yaqiong Xu, Ph.D.

Ronald D. Schrimpf, Ph.D.

Sait A. Umar, Ph.D.

Deyu Li, Ph.D.

Sharon M. Weiss, Ph.D.

To my beloved family.

ACKNOWLEDGEMENTS

TABLE OF CONTENTS

LIST OF TABLES

CHAPTER 1

INTRODUCTION TO NANOMATERIALS

Nanomaterial research is developed from material science to broad nanotechnology, which leverages advances in material metrology and synthesis in support of microfabrication research. Particularly, materials with certain nanoscale structures process their own optical, electronic or mechanical properties [1]. In this chapter, I will introduce the structure of each nanomaterial. Then I will present various synthesis methods to create each nanomaterial in all scales, from nanometer-size to wafer-size. Finally, their outstanding electronic and optoelectronic properties as well as their applications will be discussed.

1.1 Carbon Nanotube
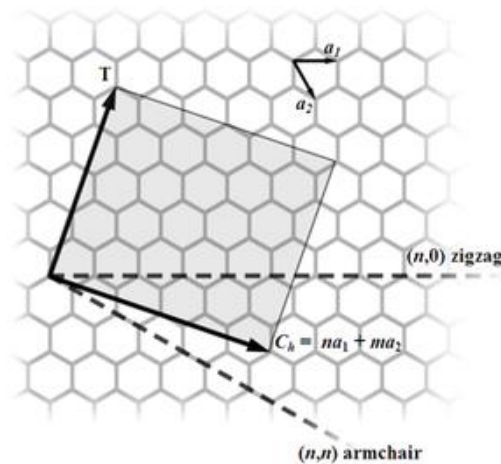
Figure 1.1 Schematic of rolling graphene into CNT by (n, m) chirality. Image reprinted with permission from Ref [2]. Copyright © 2018 Wikipedia Foundation, Inc.

In nature there exist many crystalline forms of pure carbon, like diamond and graphite. Diamond's solid hardness is due to sp^3 hybridization of carbon atoms while graphite is much softer and smoother because the sp^2 set forms the hexagonal or honeycomb

lattice [3]. Beside diamond and graphite, carbon nanotubes (CNTs) are another allotrope of carbon which can be visualized as a tubular shape of graphite. The chirality is used to describe how the carbon atoms arrange along the circumference of CNT. As shown in Figure 1.1, the chiral vector C_h is represented as a combination of a_1 and a_2, which are the unit vectors of graphene in real space. Depending on the chiral indices (n, m), we can classify CNTs as zigzag and armchair structures. For zigzag CNTs, n or m is equal to zero while n is equal to m for armchair CNTs [4]. CNTs can also be classified as either metallic or semiconducting depending on whether $n - m$ is a multiple of 3 [5]. Based on the counts of rolled-up graphene sheets, we can further classify CNTs as single-walled carbon nanotubes (SWNTs) or multiple-walled carbon nanotubes (MWNTs). Table 1.1 presents a comparison between SWNT and MWNT [6].

Table 1.1 Comparison between SWNT and MWNT

SWNT	MWNT
Single layer of graphene.	Multiple layer of graphene.
Catalyst is required for synthesis.	Can be produced without catalyst.
Bulk synthesis is difficult as it requires proper control over growth and atmospheric condition.	Bulk synthesis is easy.
Not fully dispersed, and form bundled structures.	Homogeneously dispersed with no apparent bundled formation.
Resistivity usually in the range of 10^{-4}~10^{-3} $\Omega \cdot m$.	Resistivity usually in the range of 1.8×10^{-5}~6.1×10^{-5} $\Omega \cdot m$.
Purity is poor. Typical SWCNT content in as-prepared samples by chemical vapor deposition (CVD) method is about 30–50 wt%. However high purity up to 80% has been reported by using arc discharge synthesis method.	Purity is high. Typical MWCNT content in as-prepared samples by CVD method is about 35–90 wt%.
A chance of defect is more during functionalization.	A chance of defect is less especially when synthesized by arc-discharged method.
Characterization and evaluation is easy.	It has very complex structure.
It can be easily twisted and are more pliable.	It cannot be easily twisted.

1.1.1 Growth Mechanism

High-quality nanotube materials play an important role in both fundamental and technological applications. There are four main remaining challenges regarding the synthesis of CNT. The first is mass production of CNTs with low cost, which significantly affects the industrious utilization and marketing development [7]. The second issue is selective production, considering the distribution of nanotubes in terms of various structures and

properties. The third is orientated production, control over the location on a flat substrate. Lastly, the growth mechanism, a key component of a thorough understanding of the CNT production.
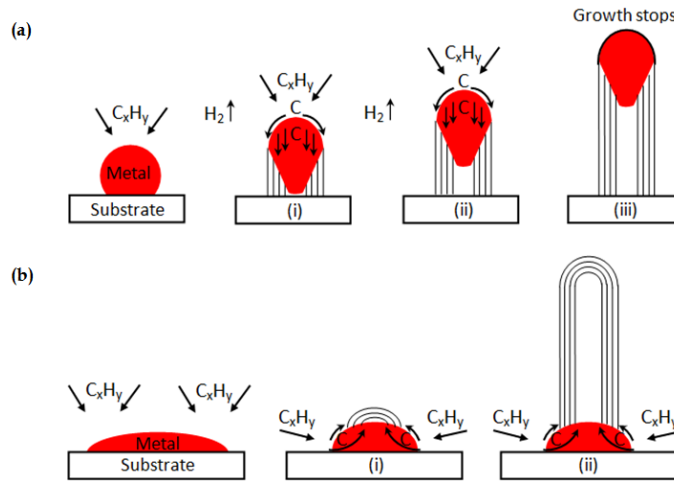
Figure 1.2 Growth mechanism of CNTs: (a) tip-growth model and (b) base-growth model. Image (a) and (b) reprinted with permission from Ref [8]. Copyright © 2011 Mukul Kumar.

In the recent decades, many techniques have been developed to produce nanotubes for a variety of structures and morphologies. The formation of nanotubes can be affected by several important elements: the catalysts such as iron or cooper particles, carbon source such as methane or ethanol, and sufficient energy from laser or furnace. Currently, three main methods have been developed to synthesize nanotubes: arcdischarge [9, 10], laser ablation [11], and chemical vapor deposition (CVD) [12-16]. Compared with arcdischarge and laser ablation, CVD methods have demonstrated to be a potential technique for mass production [17-19]. Here I briefly introduce three main stages involved in a typical CVD process: (a) a gaseous or volatile compound of carbon source is decomposed at a high temperature; (b) metallic nanoparticles are pretreated on certain substrates; (c) these metallic nanoparticles serve as seeds to initiate the growth of nanotubes. The growth mechanism of interactions

4

between each stage is not well established until now. However, there are two widely-accepted mechanism: tip-growth model and base-growth model [8]. As shown in Figure 1.2a, decomposed carbon diffuses down through the metal catalyst until there is excess carbon for the growth. The metal's top is open for decomposition of carbon because of the weak interaction between catalyst and substrate. While a strong catalyst-substrate interaction exists, decomposed carbon will diffuse upward in the opposite direction and CNTs can continue to grow longer (Figure 1.2b).
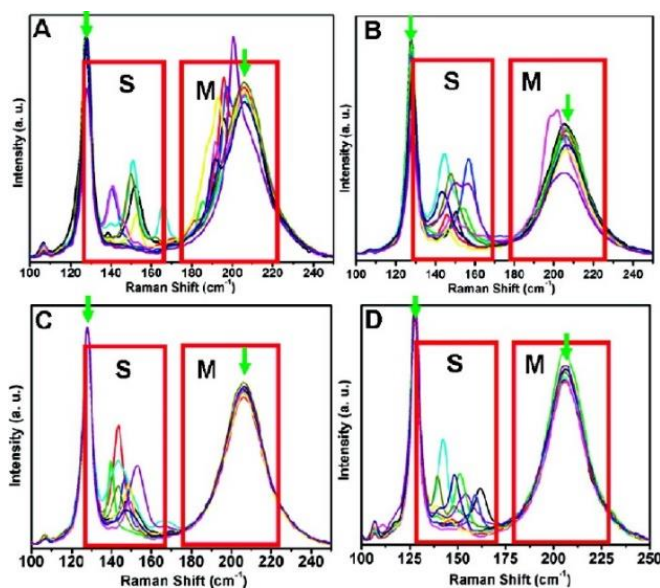
Figure 1.3 Radical breath modes (RBMs) of SWNTs on quartz with different methanol/ethanol ratios. The flow rate of ethanol was fixed at 150 sccm while the flow of methanol was controlled to (a) 0 sccm, (b) 150 sccm, (c) 450 sccm and (d) 600 sccm, respectively. The green arrows mark the Raman spectra of the quartz. S denotes the expected mode range of semiconducting SWNTs while M represents the expected mode range of metallic SWNTs. Images (a)-(d) reprinted with permission from Ref [12]. Copyright © 2009 American Chemical Society.

At each stage of the CVD process, many parameters are investigated to control the

quality of nanotubes. Here I introduce three key factors strongly associated with the growth of horizontally aligned SWNTs on quartz substrates: precursor compounds, metallic catalysts and multiple cycles of growth. In Figure 1.3, with the increasing ratio of methanol/ethanol, a higher percentage of semiconducting SWNTs is obtained in the growth outcome [12]. In addition, metallic catalysts play an important role in controlling the quality of aligned nanotubes. Figure 1.4 demonstrates that high density is achieved by manganese (Mn) or molybdenum (Mo) catalysts while the morphologies and aligned directions of nanotubes can be affected by using other catalysts such as nickel (Ni) or chromium (Cr) [20].
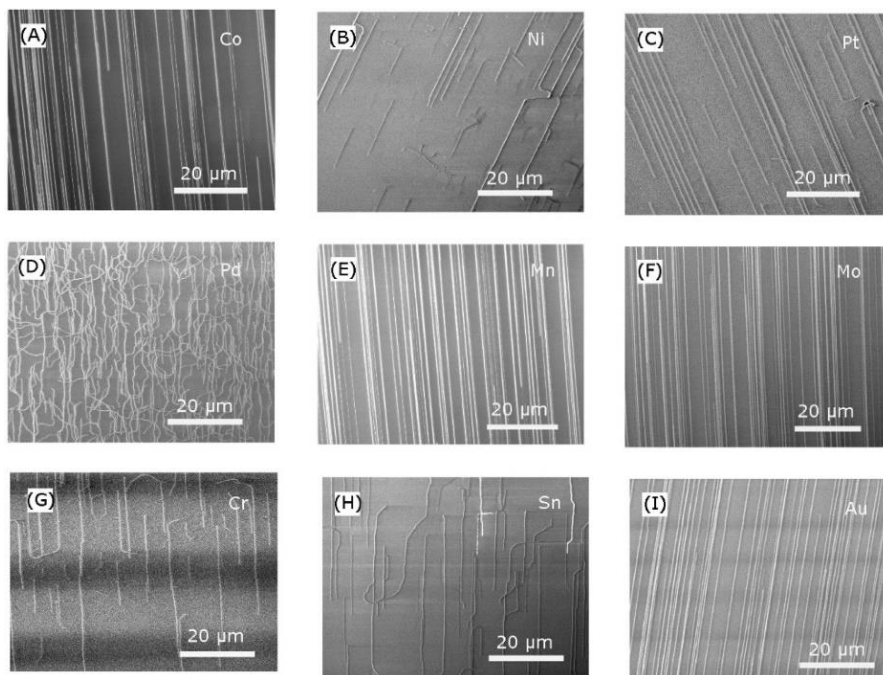
Figure 1.4 Scanning electron microscopy (SEM) images of horizontally aligned SWNTs growth by different catalysts: (a) Co, (b) Ni, (c) Pt, (d) Pd, (e) Mn, (f) Mo, (g) Cr, (h) Sn and (i) Au. Images (a)-(i) reprinted with permission from Ref [20]. Copyright © 2008 American Chemical Society.

Furthermore, the post growth or multiple cycles of growth can also alter the density and diameter of nanotubes both of which significantly determine the device performance. A

multiple-cycle CVD method [21] has been applied to the growth of horizontally aligned SWNTs. It turns out that both the density and diameter of SWNTs are much higher than that of SWNTs obtained from one-time growth, resulting in improved electronic properties [21].
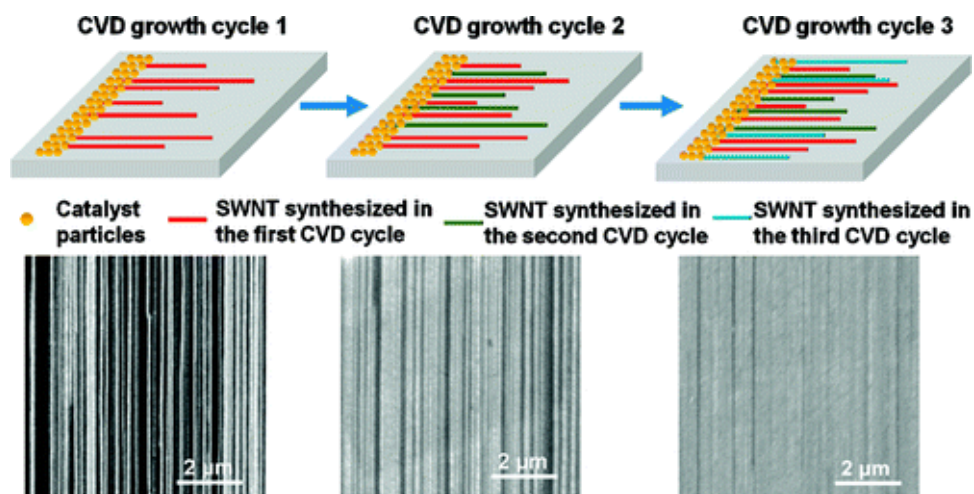
Figure 1.5 Schematic (top) and SEM images of a multiple-cycle CVD process of horizontally aligned SWNTs. Image reprinted with permission from Ref [21]. Copyright © 2011 American Chemical Society.

1.1.2 1D Geometry

The electronic properties of CNTs are investigated through CNT field-effect transistors (FETs) on thick gate dielectrics such as 300 nm of silicon dioxide (SiO_2). To form an intimate contact, metal electrodes with relatively high work function are deposited on top of CNT and the entire transistor is subsequently annealed at a high temperature under vacuum [22]. Figure 1.6 illustrates the characteristic of a back-gated CNT transistor at room temperature [23]. To minimize the Schottky barrier at the contacts between metal and nanotubes [24], two palladium (Pd) electrodes form the source and drain and the p-doped silicon (Si) substrate is applied as a back gate. The output indicates a typical p-type CNT transistor with an on-off current ratio $\geq 10^5$.
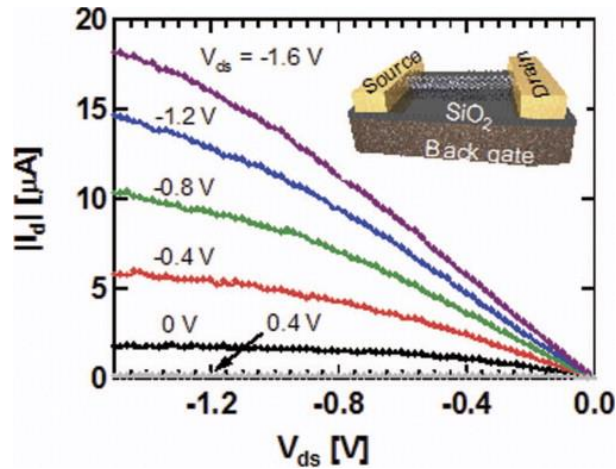
Figure 1.6 The transfer characteristic I_{ds} vs V_{ds} of a 600 nm long, 1.8 nm diameter, back-gated CNT transistors. Inset: schematic of a CNT transistor. Image reprinted with permission from [23]. Copyright © 2005 IEEE.

Under ambient conditions, CNT transistors usually display a p-type characteristic. It has been found that a p-type CNT transistor can be converted to ambipolar and further to n-type by an annealing process [25, 26]. In Figure 1.7, the initial p-type device is first converted into an unipolar n-type transistor by the thermal annealing process at 600 K [25]. With increasing oxygen doses, the device is converted back to p-type, indicating the potential application as a gas sensor. Two growth approaches of doping CNTs that alter many properties of nanotubes are presented in CHAPTER 2 and CHAPTER 3.
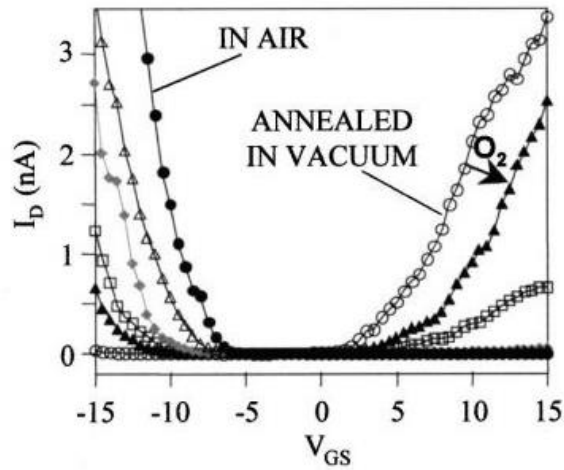
Figure 1.7 Effect of oxygen on an n-type CNT transistor by thermal annealing. Image reprinted with permission from Ref [25]. Copyright © 2002 AIP Publishing LLC.

CNTs not only exhibit superior electronic properties, but also own a variety of interesting optoelectronic properties. It can be used as a nanoscale photodetector that converts light into current or voltage. When the energy of photons is above the bandgap of CNTs, the excitons are generated and then decay into free electrons and holes, which can be separated by an external bias [27] or the internal fields associated with Schottky barriers [28, 29], p-n junctions [30] or defects [31, 32]. As shown in Figure 1.8, two spots in terms of positive and negative photocurrent can be clearly observed with the introduction of one defect in a CNT transistor [31].
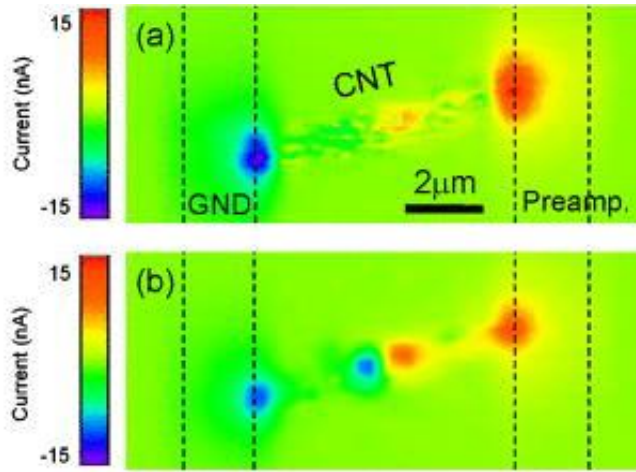
Figure 1.8 Photocurrent plots of (a) a CNT transistor without defects at $V_G = 0V$ and (b) the same transistor with one defect in the middle at $V_G = 0V$. Image reprinted with permission from Ref [31]. Copyright © 2007 AIP Publishing LLC.

Owning to the one-dimensional (1D) geometry of CNTs (Figure 1.9a), the effect of polarization on the photocurrent response at p-n junction is investigated when the excitation laser is polarized. Figure 1.9b illustrates that the photocurrent is maximized when the incident light is parallel to the nanotube axis (black arrow in Figure 1.9a) while it is minimized at the perpendicular direction (red arrow in Figure 1.9a), indicating a smaller proportion of the incident electrical field coupling into CNT [33]. The polarization-dependent study shows great potential of CNT photodetectors in telecommunications.
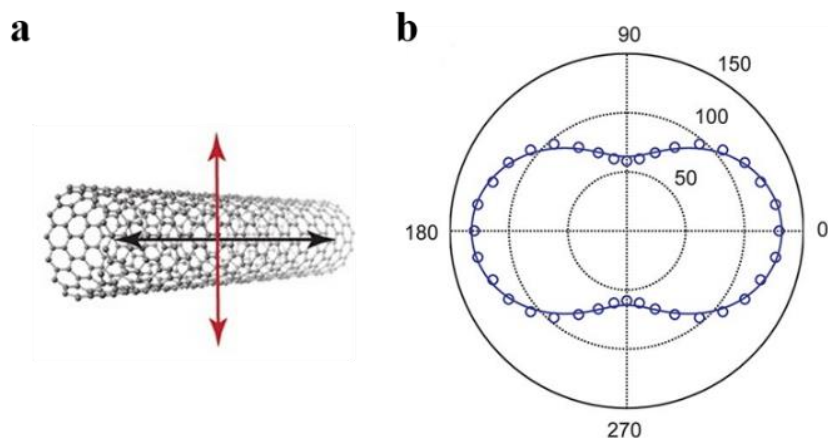
Figure 1.9 (a) Polarization dependence of the photocurrent of a CNT transistor. (b) Schematic of nanotube selection rule. Images (a) and (b) reprinted with permission from Ref [33]. Copyright © 2012 American Chemical Society.

1.1.3 Large-scale Circuits

Owing to its high mechanical flexibility [34, 35], low reflection [36, 37], feasibility of bulk production [38, 39] and compatibility with different solutions [40, 41], doping chemicals [42] and nanomaterials [43], CNTs have been applied in a large range of fields, such as chemical sensors [44-46], solar cells [47, 48], displays [49, 50], batteries [51, 52] and supercapacitors [53, 54]. For example, SWNT integrated digital circuits fabricated on flexible plastic substrates can achieve the high mobility as $80\ cm^2V^{-1}s^{-1}$ and possess excellent mechanical flexibility [55] (Figure 1.10a). Furthermore, complex CNT-based transistors integrated as a computer can run an operating system with multitasking [56] (Figure 1.10b). This is a tremendous breakthrough, indicating that CNT can be added as a prominent component among contemporary semiconductor technologies. In summary, the fabrication of circuits based on CNT transistors in circuit-level and system-level will provide potential directions of future work.
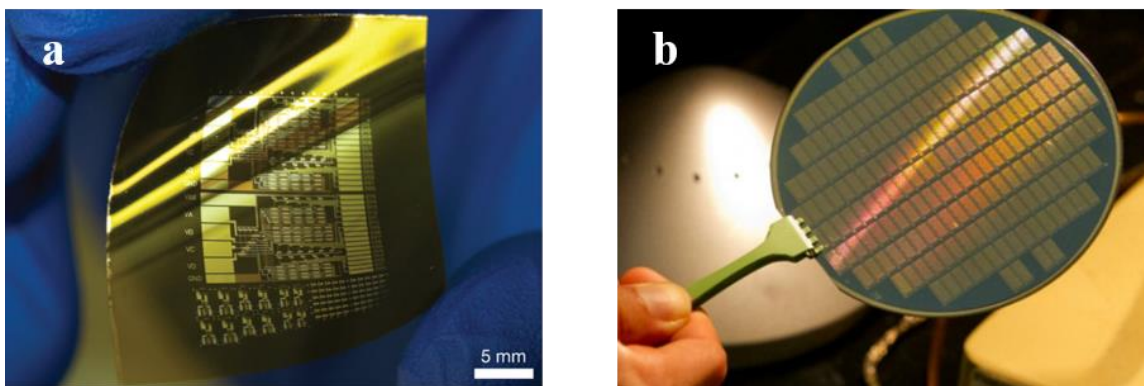
Figure 1.10 Photographs of SWNT transistors and circuits on (a) a thin sheet of plastic and (b) a 4-inch wafer. Image (a) reprinted with permission from Ref [55]. Copyright © 2008 Nature Publishing Group; image (b) reprinted with permission from Ref [56]. Copyright © 2013 Nature Publishing Group.

1.2 Graphene

Graphene consists of a single layer of tightly bonded carbon atoms in hexagonal patterns. Due to its exceptional electrical [57-59], optical [60-62] and mechanical properties [63-66], the experimental and theoretical studies of graphene have become a rapidly growing field in condensed matter research. In graphene, carbon atoms are bonded in honeycomb structures with sp^2 hybridization. As illustrated in Figure 1.11a, each carbon atom has three covalent bonds, with a separation of 1.42 angstrom (Å) in the x-y plane. Graphene is normally considered as semi-metal, since the conduction band and valence band meet at certain points in k-space. Figure 1.11b shows the band structure obtained by using the tight binding-approximation. The points where the conduction band and valence band meet are referred to as the Dirac points, or the K points. At the Dirac points, the band gap is zero and the conductivity reaches the minimum. The band structures near the Dirac points disperse linearly as cones, which are very similar to the energy dispersion of massless photons. This unique band structure of graphene provides an ideal platform for electron transportation,

12

which allows the electron mobility of graphene to be as high as 15000 cm^2 V^{-1} s^{-1} at room temperature [67].
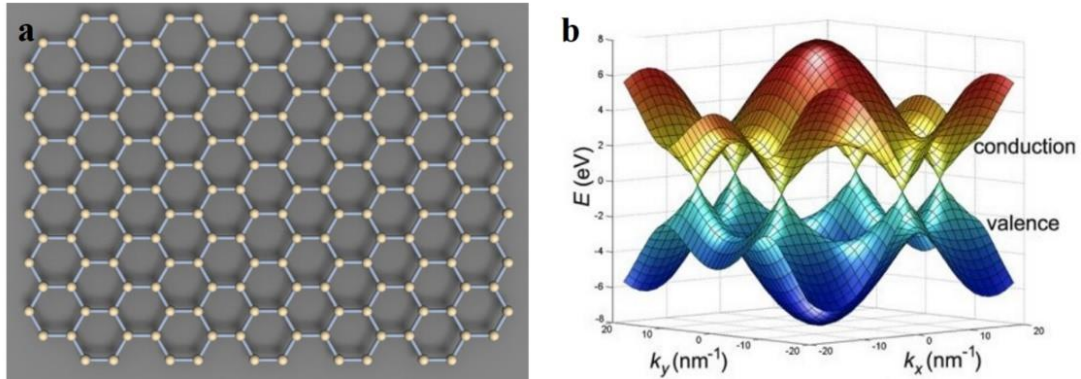
Figure 1.11 (a) The carbon atom arrangement in graphene and (b) the band structure of graphene in k-space. Image (a) reprinted with permission from Ref [68]. Copyright © 2015 James Hedberg; image (b) reprinted with permission from Ref [69]. Copyright © 2011 Arend van der Zande.

There are a few main production categories to make graphene, in various shapes, size, and attributes, for practical applications. First, graphene or reduced graphene oxide films for composite materials can be created by liquid phase and thermal exfoliation. Typically, graphite in the aqueous solution will split into multiple platelets and then produce a large amount of monolayer films after a prolonged sonication [70]. After that, the density of graphene or graphene oxide can be enriched by centrifugation. Second, for device usage, one or few layers of graphene is obtained by either mechanical exfoliation or CVD approaches. The performance or application of graphene is highly associated with a variety of factors such as quality, defects, domain size and substrates [71]. Last, other methods such as unzipping SWNTs into graphene nanoribbons, are much more expensive for commercial development. Figure 1.12 generalizes several current production methods as discussed.
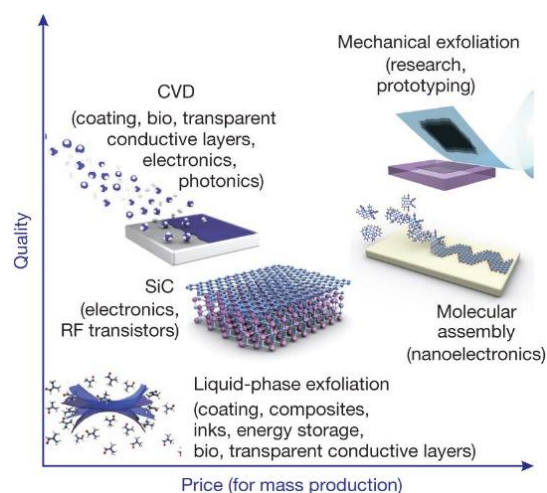
Figure 1.12 Current methods of obtaining graphene in terms of size, quality and price for applications. Image reprinted with permission from Ref [71]. Copyright © 2012 Nature Publishing Group.

1.2.1 Monolayer Films in Centimeters

Like CNTs, there are three key factors that control graphene growth in terms of domain size, quality and mass production: (a) carbon precursors, (b) catalysts and (c) pressure. Precursors can be solid, liquid or gas. Compared to liquid and solid precursors, hydrogen gas such as methane can generate graphene films in higher purity and quality [72]. Second, many metallic platforms such as platinum (Pt), cobalt (Co), nickel (Ni) and copper (Cu) have been used to synthesize high-quality graphene. For lab-based usage, copper foil is commonly used to develop monolayer graphene while the growth outcome leads to a higher percentage of multilayer graphene than using Ni as a catalyst. Recently, an optimized Cu-Ni alloy has been developed to achieve large-area single-crystalline graphene from a controlled single nucleus at a fast rate [73]. As shown in Figure 1.13, the domain size of monolayer graphene can be as large as 1.5 inch under an optimized growth condition.
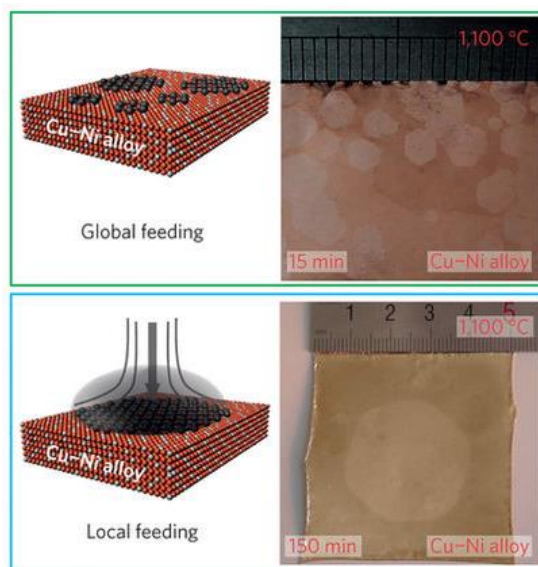
Figure 1.13 Multiple nucleation of ultrafast growth (top) and one single nucleation of long-time growth (bottom) on Cu-Ni alloy. Image reprinted with permission from Ref [73]. Copyright © 2015 Nature Publishing Group.

Graphene synthesized under atmospheric pressure presents a mixture of single-layer and multiple-layer films [74]. In contrast, low pressure can help grow graphene films with uniform thickness and fewer defects [75]. Figure 1.14 illustrates that single crystalline graphene in centimeter scale can be achieved by controlling the pressure of surface oxygen on a Cu substrate [76]. This is due to the exposure of oxygen which can decrease the nucleation density and accelerate the growth. Also, the electrical conductivity of graphene produced via this method is comparable to that of high-quality graphene using mechanical exfoliation. These CVD methods will significantly help drive the marketing application of graphene.
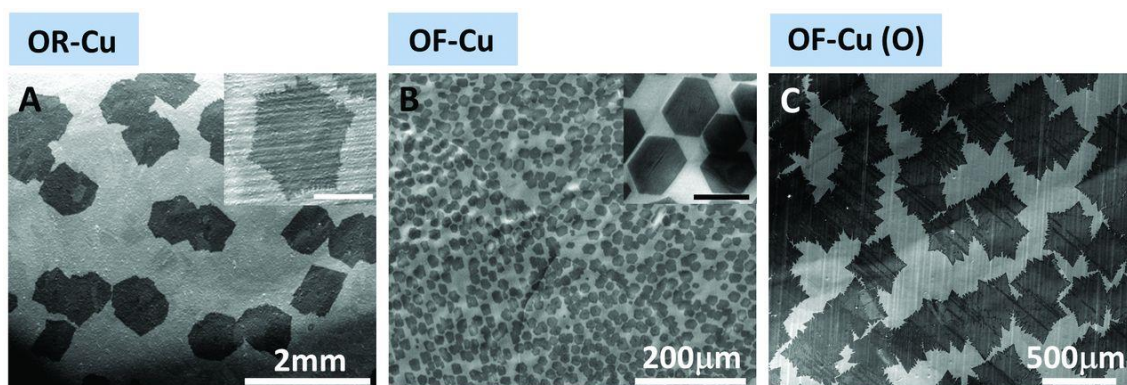
Figure 1.14 Scanning electron microscopy (SEM) images of graphene domains growth on (a) oxygen-rich Cu, (b) oxygen-free Cu and (c) oxygen-limited Cu substrates. Image (a)-(c) reprinted with permission from Ref [76]. Copyright © 2013 The American Association for the Advancement of Science.

1.2.2 Switching Dirac Point
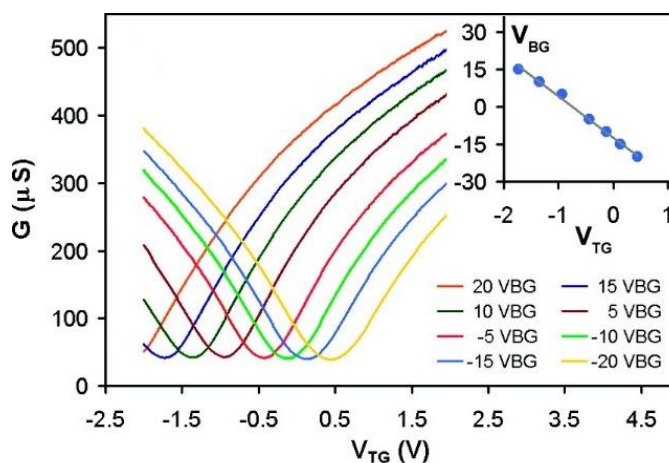
Figure 1.15 Conductance of a graphene transistor as a function of the top-gate bias voltage at different back-gate voltages. Inset: a plot of back-gate voltage versus top-gate voltage. Image reprinted with permission from Ref [77]. Copyright © 2009 American Chemical Society.

Different from semiconducting nanotubes that have band gaps inversely associated

with their diameter, graphene does not have a band gap to allow for a high on-off current ratio. Most studies have found that the on-off current ratio of a graphene transistor is less than 10, a few orders of magnitude lower than that of a semiconducting nanotube transistor [78]. However, switching in graphene can be controlled by changing the density of state with the fermi level. Figure 1.15 illustrates the variation of the conductance of a graphene transistor as the back-gate bias changes [77]. It also indicates that the location of Dirac point can be switched.
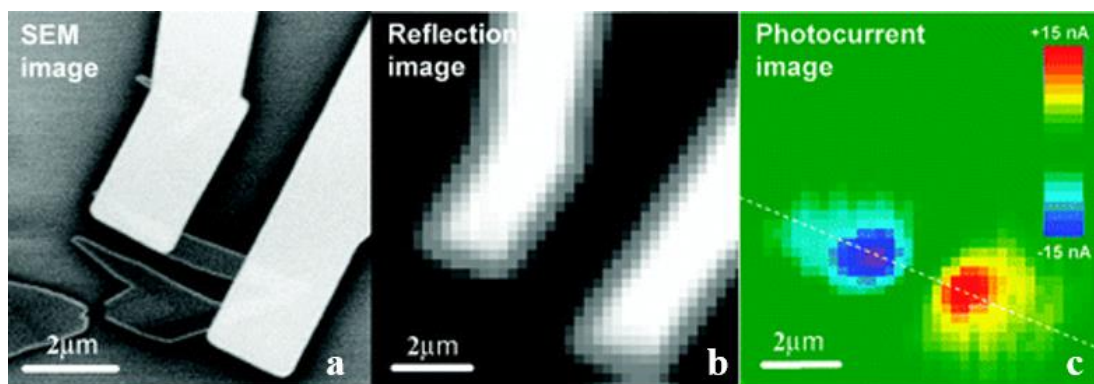
Figure 1.16 (a) SEM image, (b) reflection image and (c) photocurrent image of a graphene transistor. Images (a)-(c) reprinted with permission from Ref [60]. Copyright © 2009 American Chemical Society.

Scanning photocurrent microscopy can also be utilized to study the unique optical properties and possible applications of graphene. As discussed previously, photocurrent can be generated due to a local in-plane electric field within the graphene transistor. In Figure 1.16, the largest photocurrent of about ± 15 nA occurs near the metal contacts, indicating a strong local electrical field close to the contacts [60].

1.2.3 Toward Touch Screens

Due to its outstanding properties, graphene has many applications such as display

screens [79], electric/photonics circuits [80, 81], solar cells [82, 83] and chemical/biological sensors [84-86]. Figure 1.17 illustrates an industrial process of graphene-based touch screens, which includes CVD synthesis, transfer by thermal release, and assembling steps [79]. The production of large-scale transparent graphene electrodes demonstrates the feasibility of commercial applications in the future.
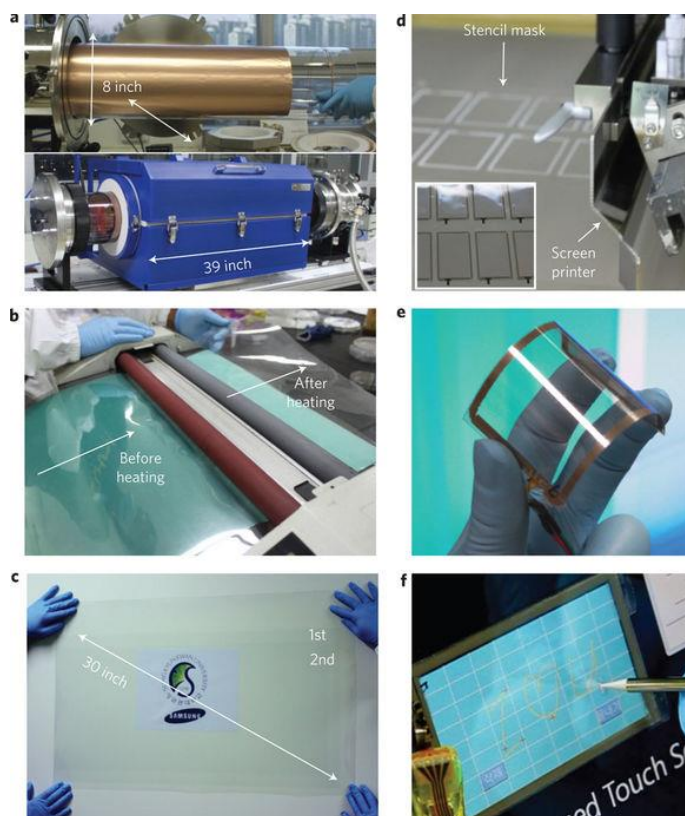
Figure 1.17 Photographs of the roll-based production of graphene films. (a) Copper foils and 7.5 quartz furnace. (b) Graphene transfer by a thermal release. (c) A large-area graphene film. (d) Screen printing process. (e) An assembled graphene/PET touch panel. (f) A graphene-based touch screen. Images (a)-(f) reprinted with permission from Ref [79]. Copyright © 2010 Nature Publishing Group.

1.3 Molybdenum disulfide

Two-dimensional materials have attracted great attention for use in the next-generation nanoelectronic devices. Transition metal dichalcogenide (TMDC) monolayers

are the recent emerging semiconducting materials with a lot of excellent properties [87-89], which are distinctly different from that of non-bandgap graphene. Due to a direct band gap, they can be used in a variety of fields such as electronic transistors, optical emitters and detectors [87].
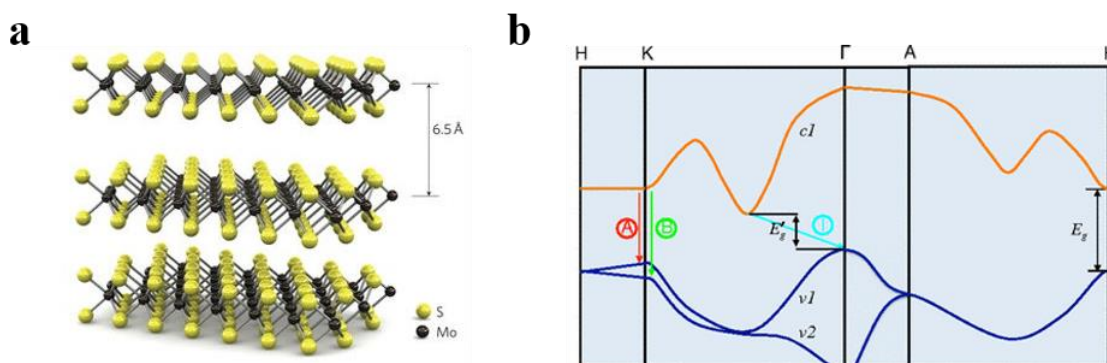
Figure 1.18 (a) Three-dimensional representation of the structure of MoS_2 and (b) simplified band structure of bulk MoS_2. Image (a) reprinted with permission from Ref [90]. Copyright © 2011 Nature Publishing Group; image (b) reprinted with permission from Ref [91]. Copyright © 2010 American Physical Society.

As a member of the TMDC family, molybdenum disulfide (MoS_2) consists one sandwiched layer of Mo atoms between two layers of S atoms [90] (Figure 1.18a). The thickness of monolayer MoS_2 is about 6.5 Å [90]. Similar to graphite, the van der Waals interactions between stacked layers allow MoS_2 to be used as a solid lubricant [92]. Earlier experiments have shown that the indirect bandgap for bulk MoS_2 is 1.29 eV while the direct bandgap is 1.90 eV for a monolayer structure [91] (Figure 1.18b).

To obtain high-quality MoS_2 layers, exfoliation methods were developed in the early research. The first is the typical mechanical exfoliation such as Scotch tape microcleavage or the anodic bonding method [93]. Even though this method is not suitable to produce MoS_2

in a large scale for commercial applications, it can yield high-quality and a defect-free MoS_2 layer with the controlling size and thickness. Another exfoliation method is via chemical approaches such as ion intercalation [94] or sonication [95]. Large quantities of MoS_2 layers can be obtained by chemical exfoliation but this method is limited for large-scale integrated circuits and electronic devices due to the small size with a higher percentage of defects.

1.3.1 Progress in Preparation

We have discussed the synthesis methods for CNT and graphene in the previous sections as well as the advantages of CVD approaches in terms of controllability and uniformity. CVD methods can also create TDMC films in wafer-size scale for future electronic applications. Typically, several main types of Mo-based precursors are involved in the preparation to grow monolayer or few-layer MoS_2 films. First, compound powders such MoO_3 or $MoCl_5$ as solid precursor [96-98], together with sulfur solid reactants are introduced into the furnace system to grow MoS_2 films. The characteristic of devices based on this approach displays typical n-type behavior with a high on-off current ratio [98]. Another method is to deposit Mo-based film on the substrates and growth MoS_2 films by the reaction with sulfur vapor at a high temperature [99]. In addition, thermal decomposition of $(NH_4)_2MoS_4$ [100] and vapor-solid growth from MoS_2 powder [101] are also used to synthesize thin films of MoS_2. However, controlling the nucleation and thickness is limited via these two methods.

Furthermore, a recent approach based on metal-organic chemical vapor deposition (MOCVD) has been used to grow TMDC layers [102]. Not only can MOCVD achieve large-scale and uniform growth, it also allows researchers to precisely control the composition and morphology of TMDC layers by preparing the metal and chalcogen precursors [103]. For MoS_2 growth, the process involves $Mo(Co)_6$ and $(C_2H_5)_2S$ and H_2 or Ar gas (Figure 1.19a).

20

Wafer-size films of monolayer and few-layer MoS_2 (Figure 1.19b) have been obtained with the field-effect mobility as high as 30 $cm^2V^{-1}s^{-1}$ at room temperature [102]. In general, these CVD approaches of synthesizing TMDC will pave the way for next-generation electronics and optoelectronics devices.
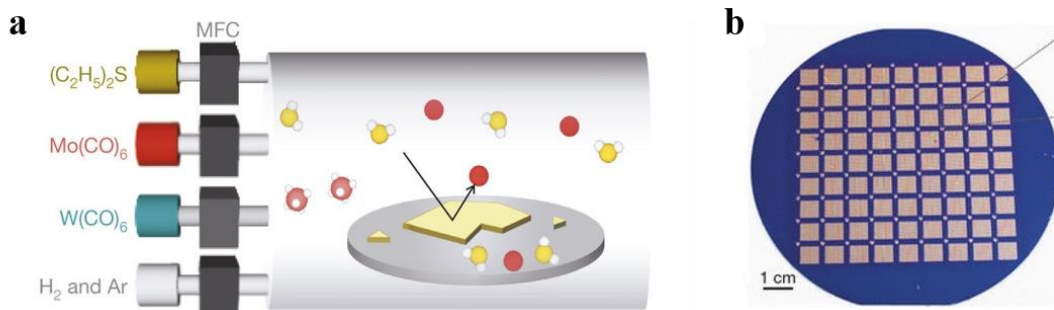
Figure 1.19 (a) Diagram of setup for metal-organic chemical vapor deposition. (b) Photograph of MoS_2 transistors on a 4-inch SiO_2/Si wafer. Images (a)-(b) reprinted with permission from Ref [102]. Copyright © 2015 Nature Publishing Group.

1.3.2 Tuning On-off Current Ratio and Photocurrent
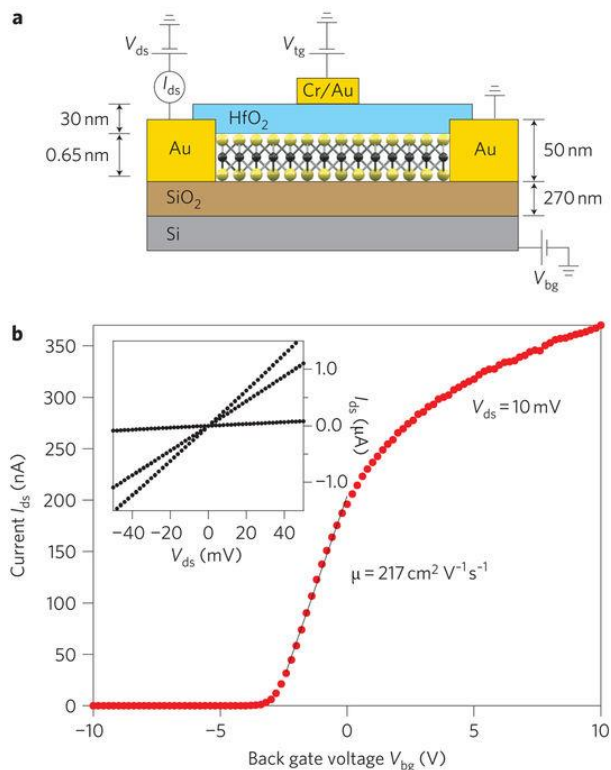
Figure 1.20 (a) Schematics of a monolayer MoS_2 transistor with the HfO_2 top-gate dielectric layer. (b) The transfer characteristic of this MoS_2 transistor. Inset: I_{ds}-V_{ds} curve with V_g at 0 V, 1 V or 5 V. Image (a)-(b) reprinted with permission from Ref [90]. Copyright © 2011 Nature Publishing Group.

The intrinsic band gap allows MoS_2 to be used in semiconducting devices. However, the reported mobility of MoS_2 transistors range from 0.1 to 30 $cm^2V^{-1}s^{-1}$ is still too low for practical applications. A HfO_2 gate dielectric integrated on top of monolayer MoS_2 devices can help increase the field-effect mobility to 200 $cm^2V^{-1}s^{-1}$ at room temperature [90] (Figure 1.20). The on-off current ratio of this device can achieve as high as 10^8, a several order of magnitude improvement over typical transistors based on exfoliated or CVD-grown MoS_2 films.

In addition, the intriguing optical properties of MoS_2 layers have been studied for

optoelectronic and energy conversion applications. As shown in Figure 1.21, photocurrent scanning microscopy is used to explore the enhancement and suppression of the current with the variation of source-drain biases (V_{DS}) [104]. When there is a positive V_{DS}, the band at the source contact bends, leading to an increase of photocurrent. In contrast, the photocurrent increases at the drain contacts when V_{DS} is negative. This photocurrent study will help guide the future development of optoelectronic devices based on MoS_2.
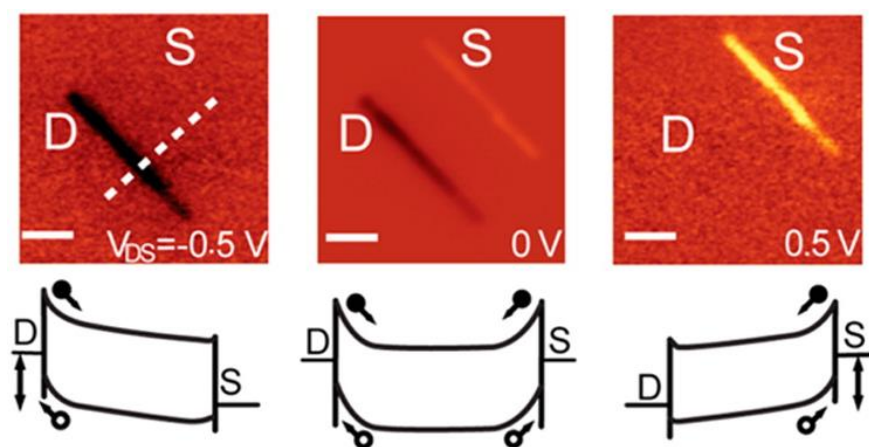
Figure 1.21 Photocurrent images of a 4-layer MoS_2 transistor under zero back-gate bias ($V_G = 0$ V) with drain-source bias at -0.5 V, 0 V and 0.5 V. Below shows the corresponding band diagrams. Image from reprinted with permission from Ref [104]. Copyright © 2013 American Chemical Society.

1.3.3 Flexible and Ultrasensitive Devices

We have introduced several advantages of MoS_2 due to its scalability via CVD approaches, large intrinsic bandgap and outstanding electronic and optoelectronic properties. Currently, MoS_2 layers integrated with many other nanomaterials or preexisting devices, have been utilized in many ways such as in lubricants [92], flexible devices [105], gas sensors [106] and lithium ion batteries [107, 108]. For example, MoS_2 transistors integrated with ion gel dielectrics on polyimide substrates have shown excellent transport properties

with a mobility of 12.5 $cm^2V^{-1}s^{-1}$ and an on-off current ratio of 10^5 as well as remarkable mechanical flexibility [105] (Figure 1.22a). The MoS_2 device also displays a fast response in the change of drain-source current when it is exposed to NO gas [106] (Figure 1.22b). This high sensitivity is consistent with CNT and graphene, indicating the potential application of nanomaterials in gas sensing in the future.
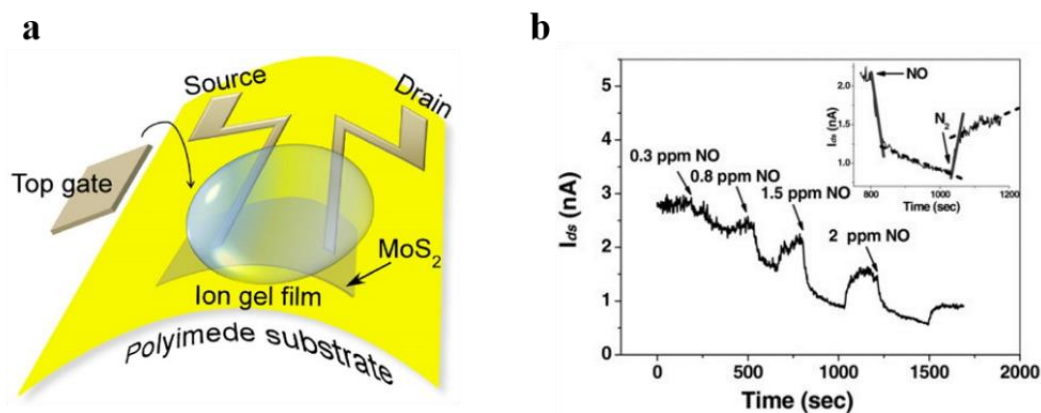
Figure 1.22 (a) Schematic of a flexible MoS_2 transistor with ion gel film on the top and (b) Current response of a 2-layer MoS_2 transistor under NO exposure. Image (a) reprinted with permission from Ref [105]. Copyright © 2012 American Chemical Society; image (b) reprinted with permission from Ref [106]. Copyright © 2011 John Wiley and Sons.

CHAPTER 2

CONTROLLING GROWTH OF CARBON-BASED MATERIALS

In this chapter, I first discuss CVD approaches to synthesize graphene in two dimensional (2D) and three dimensional (3D) structures, transfer techniques and related characterizations. In the end, I discuss the extended research about combining CNT networks and graphene films. The novelty of this hybrid shows excellent mechanical and electronic properties.

2.1 CVD Synthesis of Graphene

We have introduced a plethora of methods to obtain graphene materials such as mechanical exfoliation or CVD approaches. The graphene devices I present in this dissertation are based on the CVD method, which usually involves the use of carbon-containing gases and catalytic substrates. Depending on the conditions, the CVD method could produce either single-layer or few-layer graphene by optimizing the parameters of growth condition such as the ratio of CH_4 and H_2.

Here I adopt a standard CVD method to synthesize monolayer graphene (more experimental steps are listed in the appendix). Copper foils (Alfa Aesar 0.025 mm, 99.8%) with a grain size of ~ 100 μm were cut into a slide of 10 cm in length and 1.5 cm in width, which were pretreated with 5% nitric acid bath for 5 minutes and then deionized water for 3 minutes twice to eliminate the oxide layer and the contamination on the surface of copper foils [109]. For the growth, we loaded copper foils onto a quartz boat and transferred them to a horizontal furnace system by a magnetic bar. We started to flow 200 sccm Ar to purge the system before it was pumped down to 10 mTorr. Then we annealed the samples with a flow of 100 sccm H_2 at the temperature of 1000 ℃ for 1 hour and continued to flow H_2 along

with 20 sccm of CH_4 to fulfill the growth. The growth was conducted at the same temperature for 30 min. After that, CH_4 and H_2 flow were terminated while 200 sccm Ar starts to purge the system. At the same time, the sample was quickly pulled out of the furnace by a magnetic bar and placed on the downstream of the quartz tube at room temperature. For 3D multilayer graphene, we replaced copper foils with nickel foam and apply 200 sccm H_2 and 10 sccm CH_4 in the growth for 20 minutes.

After growth, we need to get graphene off the catalytic substrates and transfer it to the target substrates. A common method is the wet transfer technique (Figure 2.1). The general transfer process involves three parts. First, spin coat or drop the polymer such as poly (methyl methacrylate) (PMMA) onto the sample substrates. Second, place your sample into the etching solution for a reasonable time and whether we need to heat the etching solution or not depends on the substrates. Finally, we remove the polymer before transferring onto the desired substrates.
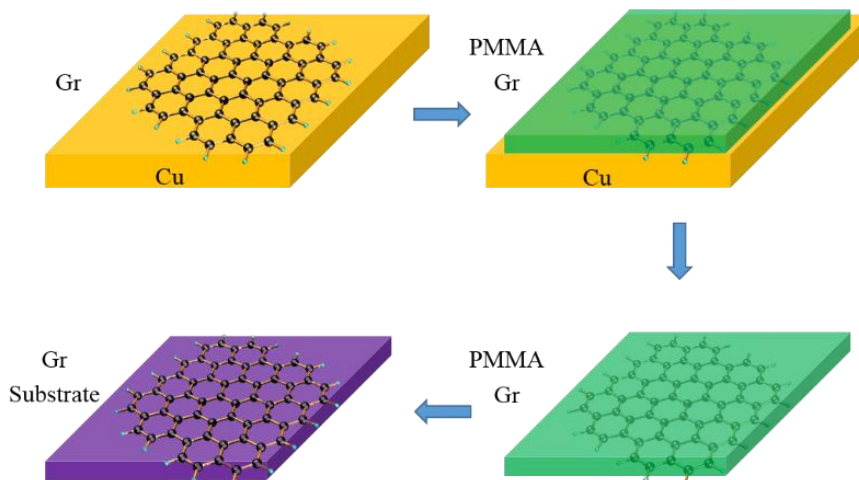
Figure 2.1 Schematic of graphene transfer processes.

For most materials discussed in this dissertation, the general transfer techniques are summarized in Table 2.1. To obtain high-quality material, it is better to spin coat polymer

onto samples without baking and allow for a long etching process if possible. For quartz and SiO$_2$/Si substrates, a hot KOH solution will be used to remove the oxide layer and then the films can be peeled off from the surface. Special preparations are listed in the appendix.

Table 2.1 Summary of transfer techniques

	Polymer	**Etch**	**Cleaning**
2D graphene	PMMA A2	FeCl$_3$	Acetone
3D graphene	PMMA A2	FeCl$_3$ + HCl	Acetone
Aligned CNTs	PMMA A2	KOH (70 °C)	Acetone (70 °C)
MoS$_2$	PMMA A2	KOH (70 °C)	Acetone (70 °C)
CNT-graphene hybrids	No polymer	FeCl$_3$	Deionized water
SWNT-MoS$_2$ hybrids	PMMA A2	KOH (70 °C)	Acetone (70 °C)

* Transfer instructions for graphene, aligned CNTs, MoS$_2$ and various hybrids discussed in this dissertation.

2.1.1 Monolayer and Few-layer Graphene
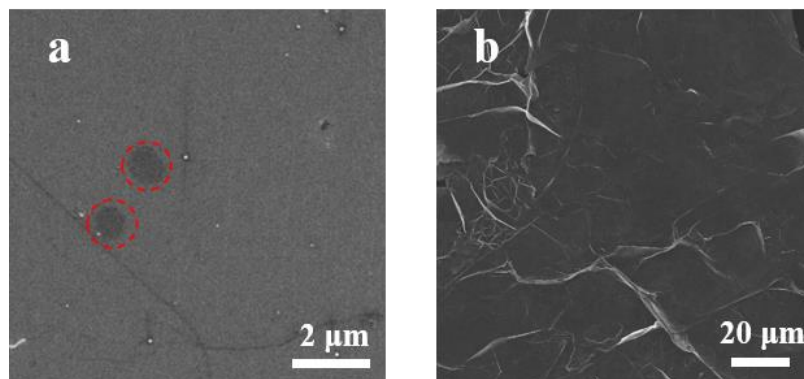
Figure 2.2 SEM images of 2D graphene and 3D graphene.

Scanning electron microscopy (SEM) can help visualize the morphology of our material by scanning the surface with a focused beam of electrons. It has been widely used to characterize the material discussed in this dissertation. Figure 2.2a shows 2D graphene on SiO$_2$/Si substrates, where the areas circled by red dash lines imply more than one layer. Different from 2D graphene, we can observe more wrinkles on the surface of 3D graphene (Figure 2.2b) after the etching process, which are likely to be multilayer.

Raman spectroscopy is a spectroscopic technique used to observe vibrational, rotational, and other low-frequency modes in a system [110]. It has been used to reveal many intrinsic properties of graphene, such as quality and thickness. As shown in Figure 2.3, there are three strong bands: D peak at ~ 1350 cm^{-1}, the G peak at ~ 1580 cm^{-1}, and 2D peak at ~ 2680 cm^{-1} and ~ 2730 cm^{-1} for monolayer and multilayer graphene, respectively. The D band is related with a significant number of defects or impurities and normally is rarely seen in pure graphene [111]. Here the D band is likely due to the defects produced in the CVD process or the remaining residues of chemical solvents during the transfer process.The G band feature is common to all sp^2 carbon systems owing to the doubly degenerate zone center

28

E_{2g} mode [111] while the 2D peak is the second order of zone-boundary phonons [112]. The intensity of the 2D peak in Figure 2.3a and Figure 2.3b is ~ 1.5 times and ~ 0.3 times as high as that of the G peak, indicating that the as-produced graphene is single-layer and multilayer [113].
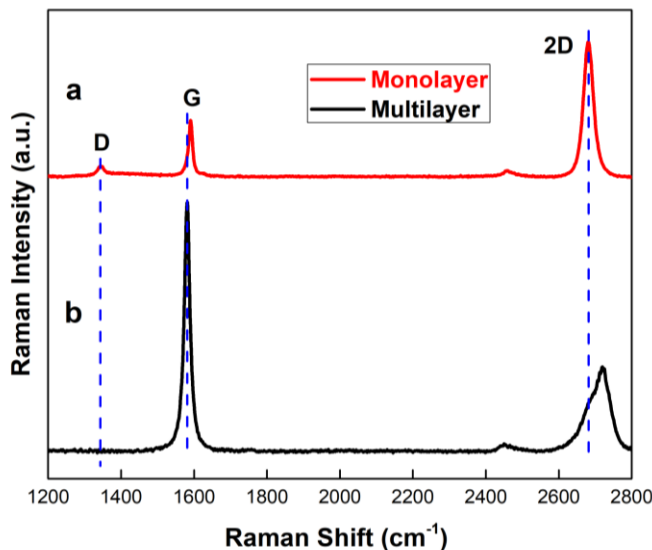
Figure 2.3 Raman spectrum of graphene from copper foils and nickel foams.

2.1.2 Graphene Transistors

In conventional three-probe FET structure, the drain current I_D defined as the current measuring the drain electrode is controlled by the strength of the gate potential V_G while biasing the source-drain voltage V_{DS}. Figure 2.4a illustrates a schematic diagram of the electrolyte-gated graphene FET. An 8-mm diameter cylinder was attached to the substrate and filled with 1X phosphate buffered saline (PBS) solution (~ 150 mM). A gold wire was used as a gate to set the electrochemical potential of solution. When the gate voltage swept from 0 V to 1.6 V (black curve) or in the opposite direction (red curve), the conductance of a graphene transistor was recorded at a source-drain voltage of 50 mV (Figure 2.4b). This

figure shows ambipolar behavior with Dirac point close to $V_G = 0.8V$. The hysteresis in the transfer characteristics is likely due to the time delay for the potential to be distributed in solution, which can be reduced by decreasing the rate at which the gate voltage is swept or by increasing the concentration of ions in the solution. Several key features can be gleaned from the transport characterization: (1) The sensitivity of the graphene FET device can be readily calculated as the slope at a specific V_G value. (2) The sensitivity can be varied by changing the electrolyte gate offset value. (3) The sign of the recorded signal can be inverted while graphene FET is operated from p- to n-branch.
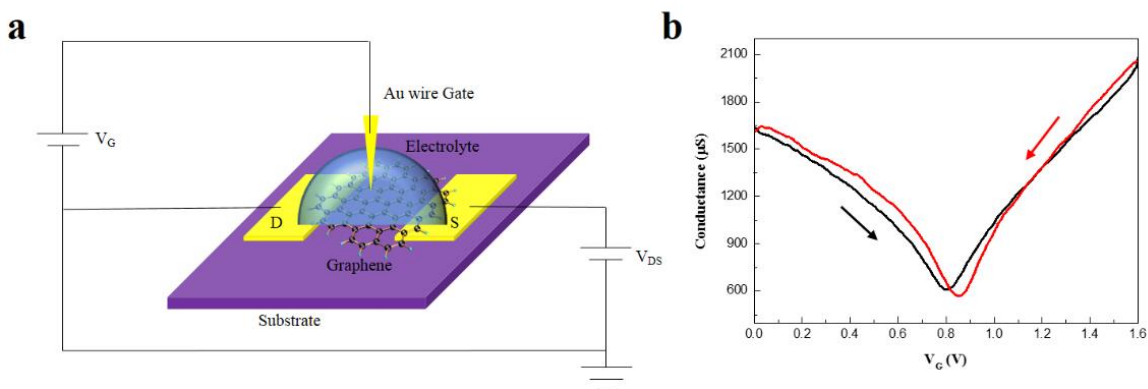
Figure 2.4 (a) Schematic of an electrolyte-gated graphene FET and (b) corresponding gate-dependence of monolayer graphene in two directions marked as a black curve and a red curve.

The setup we applied to detect the local photocurrent response from a graphene transistor is illustrated in Figure 2.5a. A collimated laser beam ($\lambda = 785$ nm) was expanded and focused onto a diffraction-limited laser spot (< 1 µm) via a 60x water/oil inversion objective. The laser beam scanned over graphene transistors by a two-axis scanning mirror with nanometer spatial resolution (Figure 2.5a and Figure 2.5b). The photocurrent signals were collected by using a preamplifier. A pronounced photocurrent response at the two edges of graphene results from Schottky-like barriers between metal electrodes and graphene

(Figure 2.5c). Simultaneously, the reflected light from the device was recorded by a Si photodetector, which can be overlapped with the photocurrent image to locate the position of the photocurrent response (Figure 2.5d). This system is also combined with a fluorescence microscope, which can be used to detect electrical activity of individual synapses by scanning photocurrent measurements and simultaneously visualize the dynamics of synapse formation and maturation through fluorescence microscopy.
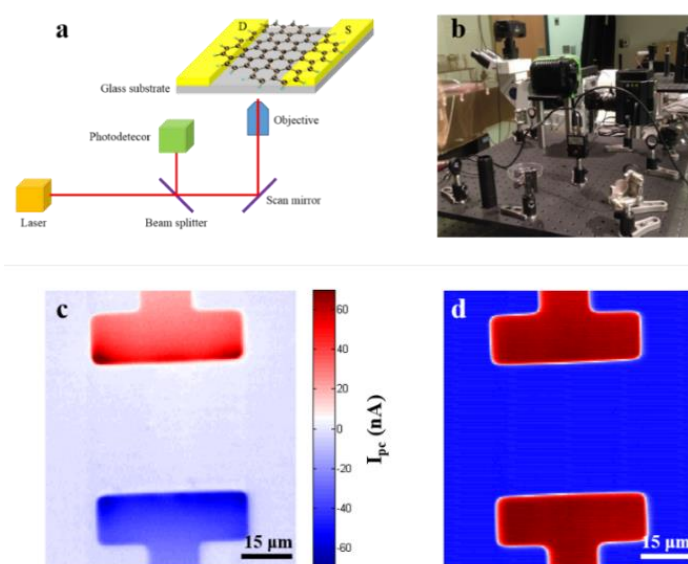
Figure 2.5 The optical setup of scanning photocurrent measurement including the schematic (a) and experimental part (b). (c) A typical photocurrent mapping of graphene transistor and (d) a corresponding reflection image of electrodes.

2.2 Ultrathin SWNT Network Framed Graphene Hybrids

Graphene and SWNTs have shown superior potential in electronics and optoelectronics due to their excellent thermal, mechanical, electronic, and optical properties. Here, a simple method is developed to synthesize single-layer CNT-graphene films through CVD. These novel two-dimensional hybrids show excellent mechanical strength that allows

them to float in water without polymer supporting layers. Characterizations by Raman spectroscopy and transmission electron microscopy (TEM) indicate that CNTs are partially unzipped into nanoribbons, interlacing as a concrete backbone for the sequential growth of the graphene layer. Electrical transport measurements further show that the CNT-graphene hybrids maintain similar electronic behaviors as the CVD-grown monolayer graphene, suggesting the structural integrity of the 2D hybrids. We also find strong photocurrent response in the CNT-graphene junctions, which may result from the stacked graphene structures between graphene grains and unzipped-nanoribbons. Our method provides a new way to fabricate robust graphene hybridized structures for future applications in electronics and optoelectronics.

2.2.1 Motivation

Graphene and carbon nanotubes have gained great interest due to their unique properties such as high charge carrier mobility, remarkable thermal conductivity, and large surface-area-to-volume ratio [67, 114-123]. Various methods have been developed to integrate CNTs with graphene to form new hybrids materials. For example, combination of graphene oxide and CNTs has been demonstrated to be high-performance, flexible, and transparent materials as conductors, electrodes and supercapacitors [124-126]. Metal catalysts such as copper or iron nanoparticles have been deposited onto graphene for out-of-plane growth of CNTs through CVD. Recently, vein-like CNT network layers have been stacked onto graphene to improve its mechanical strength [127]. However, the thickness of such hybrids ranges from 200 nm to a few micrometers, leading to a lower transparency (~ 53% at 600 nm) than that of single-layer graphene (97.7% at 600 nm) [128]. Moreover, rebar graphene has been developed by partially unzipping CNTs into graphene nanoribbons (GNRs) through high temperature annealing with a hydrogen flow [129]. It exhibits good

32

mechanical performance but appears porous-like and lacks structural integrity because partially unzipped CNTs cannot fill in the two-dimensional plane as a complete film. Therefore, it is desirable to develop a method to produce ultra-thin CNT-graphene films with not only enhanced mechanical strength, but also high optical transmission and good electrical conductivity.

Here we introduce a simple method to synthesize 2D CNT-graphene hybrids. We first spin-coat single-layer CNTs on a copper foil as a network of supporting frame, and then introduce methane as a feeding gas for single-layer graphene growth. Without utilizing the mechanical support from PMMA, large-area CNT-graphene hybrids can be transferred onto arbitrary substrates. Results from Raman spectroscopy and transmission electron microscopy indicate that CNTs are partially unzipped into nanoribbons, gluing graphene grains together to form highly-transparent 2D CNT-graphene hybrids. Electrical transport measurements show that CNT-graphene hybrids maintain similar electrical properties as CVD-grown monolayer graphene and exhibit higher turn-on electrical conductance than CNT networks alone. By comparing scanning photocurrent measurements and SEM images, we find that strong photocurrent signals are generated in the junction regions between different graphene grains, which may result from the stacked nanoribbon-graphene structures in these areas as reported in previous literatures [130-132].

2.2.2 Experimental Methods
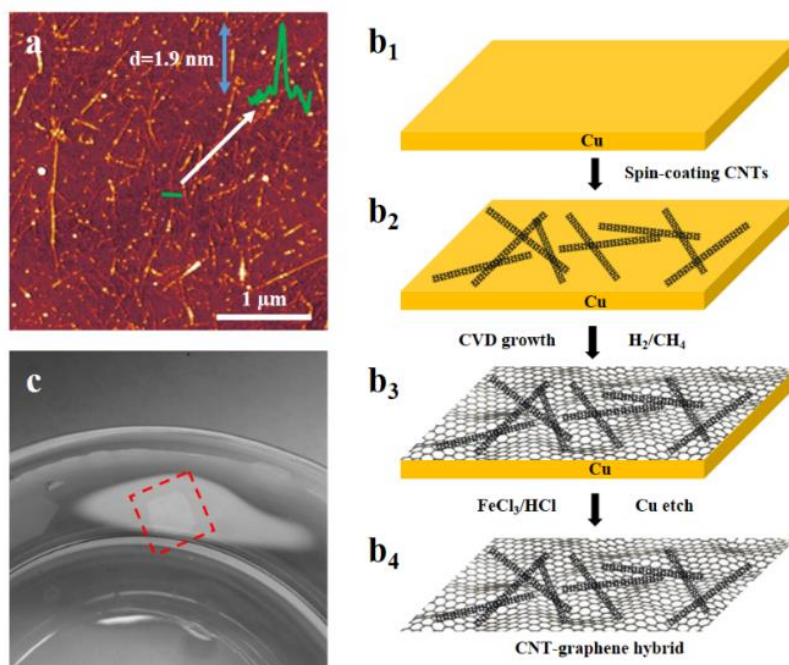
Figure 2.6 (a) An AFM image of individual CNTs, randomly-distributed on the SiO$_2$/Si substrate to form an ultra-thin network. Inset: The height of a CNT is about 1.9 nm, which is the typical diameter of individual functionalized-CNTs. (b) Schematic diagram of the synthesis process of CNT-graphene hybrids. (c) A photograph of polymer-free CNT-graphene hybrids suspending in the deionized water bath.

Figure 2.6 shows the fabrication process of CNT-graphene hybrids. In our experiment, as-produced high-pressure CO (HiPco) SWNTs were functionalized via reductive alkylation using lithium and alkyl halides in liquid ammonia [133]. The functionalized CNTs were resuspended in chloroform and spin-coated on the targeted substrates (Figure 2.6a) to form single-layer randomly-distributed CNT networks, whose morphology can be characterized by atomic force microscopy (AFM). The height of the functionalized CNTs ranges from 1 nm to 2 nm (the inset of Fig. 1a: $d = 1.9 \ nm$), which is

higher than the typical diameter (~ 1 nm) of as-produced HiPco CNTs [134] due to the sidewall functional groups [133].

To form CNT-graphene hybrids, we adopted a standard CVD method that was developed to synthesize graphene [132, 135]. Copper foils (Alfa Aesar, 0.025 mm, 99.8%) with a grain size of ~ 100 µm were cut into squares of 1.5 cm in length. The copper foils were pretreated with 5% nitric acid bath for 1-2 minutes and then with deionized water bath for 3 minutes twice to remove the oxide layer and surface contamination (Figure 2.6b$_1$) [109]. After that, a 50 µL functionalized CNT chloroform solution was spin-coated on top of a copper foil square at 4000 rpm for 45 seconds (Figure 2.6b$_2$). For comparison, a copper foil square with CNTs and one without CNTs were both loaded onto a quartz boat simultaneously, which was transferred to a horizontal furnace system by a magnetic bar [136]. After the system was pumped down to 10 mTorr, the temperature was raised to 1000 °C and the samples were annealed in 50 sccm H$_2$ for 1 hour. The spin-coated CNTs were partially unzipped into nanoribbons during hydrogen-inducing process as reported in previous experimental work [129] and theoretical simulation [137]. 10 sccm CH$_4$ was then added to conduct the graphene synthesis for 30 minutes (Figure 2.6b$_3$). The boat was quickly pulled out of the furnace by a magnetic bar and placed on the downstream of the quartz tube at room temperature when the graphene growth was finished. During the subsequent transferring process, the as-produced CNT-graphene hybrid can hold the surface tension and float in the copper etchant (FeCl$_3$) solution by itself (Figure 2.6c), while the graphene only films synthesized at the same time needs the assistant of a PMMA layer. After a wet etching process with FeCl$_3$ solution, we transferred samples to hydrochloric acid bath and then deionized water bath for several times to remove copper and chemical residues produced during the transfer (Figure 2.6b$_4$).

2.2.3 Results and Discussion

Raman spectroscopy was performed to characterize the CNT networks, CNT-graphene hybrids, and graphene only films on SiO_2/Si substrates by a 532 nm laser (Figure 2.7a). For SWNT networks, three typical strong bands were observed (Figure 2.7a, *blue*): a diameter-dependent radial breathing mode (RBM) at ~ 237 cm^{-1}, a disorder mode (D) at ~ 1330 cm^{-1}, and a tangential mode (G) at ~ 1590 cm^{-1}. According to the $\omega_{RBM}(cm^{-1}) = 234/d_t\,(nm) + 10$ relation [138, 139], we obtain the diameter of randomly-distributed CNTs to be ~ 1.03 nm, a typical diameter of as-produced HiPco CNTs [134]. A strong disorder band at ~ 1330 cm^{-1} appears because of the covalent side-wall functionalization [133]. The Raman spectrum of graphene grown on a clean copper foil square shows that the intensity of the 2D mode (~ 2680 cm^{-1}) is ~ 1.5 times as high as that of the G mode (Figure 2.7a, *black*), indicating that the as-produced graphene is single-layer [113]. However, the intensity of the 2D mode of CNT-graphene hybrids synthesized simultaneously is less than or equal to the G mode intensity, a typical spectrum of few-layer graphene [113]. The relatively high D peak for CNT-graphene hybrids (Figure 2.7a, *red*) might be related to the interactions between graphene and unzipped CNTs.
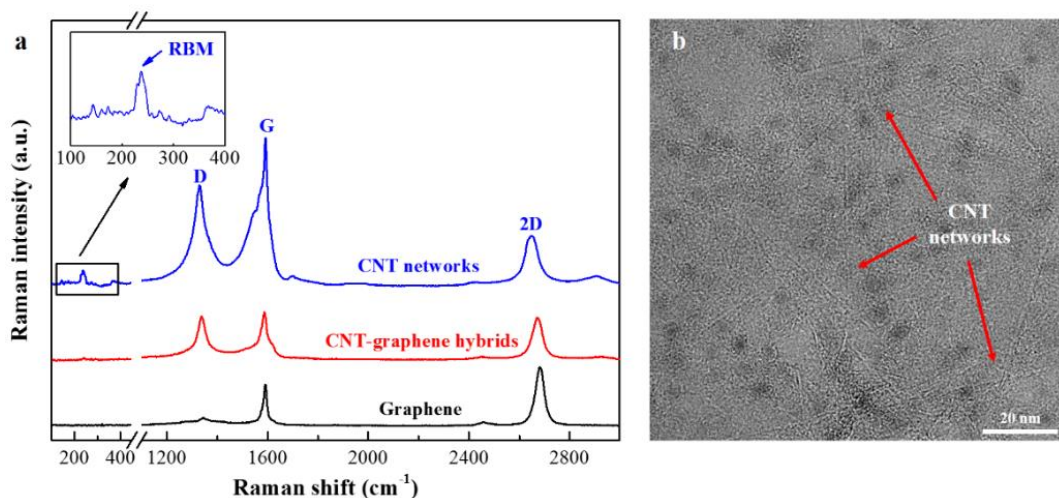
Figure 2.7 (a) Raman spectra of the CNT networks (blue), CNT-graphene hybrids (red), and graphene only films (black). Inset: Detailed spectrum of RBM for the CNT networks. (b) A TEM image of the CNT-graphene hybrids shows that graphene is undergirded by CNT networks, where CNTs are marked by red arrows.

In addition, the strong RBM of CNTs disappears after the hybrid growth process. This indicates that randomly-distributed CNTs unzip into GNRs, which is in good agreement with the previous experiment [129]. The unzipped CNTs can stack onto the graphene surface to form few-layer graphene structures, resulting in a reduced intensity ratio of the 2D to G band (<1).

FEI Tecnai Osiris Transmission Microscope (operated at 200 kV) was used to characterize the structure of CNT-graphene hybrids. Polymer-free CNT-graphene hybrids were transferred onto lacey carbon grids, which were fixed on the clean glass by a small-volume drop of ethanol. The samples were pre-treated with 100 sccm Ar and 10 sccm H_2 flow at 350 ℃ for 30 minutes, which is intended to remove the amorphous carbon on the surface. As shown in Figure 2.7b, single-layer randomly-distributed CNT networks interlace

with each other and form a solid backbone to support the graphene layer and to enhance the connection between different graphene grains. This 2D hybrid film exhibits better mechanical strength than the graphene only films since it can float in water and can be transferred to any substrate without polymer support layers. Interestingly, there are a few black nanoparticles on the CNT-graphene hybrid films, which may result from copper residues during the transfer process or iron catalysts in as-grown HiPco CNTs. More experiments need to be performed to further clean CNT-graphene hybrid films in the future.

Electrical transport measurements were also performed to characterize the electrical performance of single-layer CNT networks, CNT-graphene hybrids, and graphene only films respectively. Single-layer CNT networks were spin-coated at 4000 rpm for 45 seconds on a glass substrate and then annealed at 350 ℃ in the furnace for 30 minutes to remove surface functional groups from CNTs, while the other two samples were transferred onto the glass substrates after a wet etching process as described in the previous section. All glass substrates were pre-patterned with source and drain electrodes (5nm Cr and 40 nm Au). An 8mm diameter cylinder was attached to the substrate and filled with 1x phosphate buffered saline (PBS) solution (~ 150 mM). A gold wire was used as a gate electrode to modulate the electrochemical potential of the PBS solution. When the gate voltage swept from 0 V to 1.2 V, the conductance of different samples was recorded at a source-drain voltage of 50 mV.
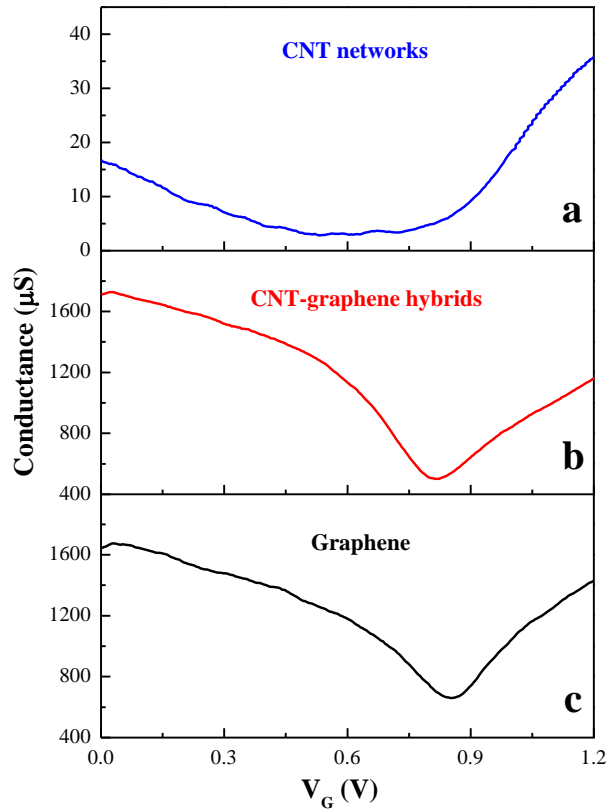
Figure 2.8 Gate-dependence of (a) CNT networks, (b) CNT-graphene hybrids, and (c) graphene only films.

As shown in Figure 2.8a, single-layer randomly-distributed CNT networks exhibit a predominately p-type behavior at a gate voltage of 0 V, typical for CNTs. On the other hand, the CNT-graphene hybrid device shows higher conductance than pure CNT networks when turned on, suggesting that the conductance of CNT networks have been improved by the introduction of graphene. By comparing the conductance of the CNT-graphene hybrids (Figure 2.8b) with that of graphene only films (Figure 2.8c) simultaneously synthesized from the same growth process, it is obvious that the CNT-graphene hybrids inherit the electrical transport properties from monolayer graphene since they show similar Dirac points (V_{Dirac} ~ 0.8V) and gate-dependent behavior.

While the electrical transport properties of CNT-graphene hybrids and graphene are similar as a whole film, it is also interesting to explore the local conductance distribution through scanning photocurrent microscopy, especially in the CNT-graphene hybridized structure. In our experiments, a 785 nm diffraction-limited laser spot (~ 1 µm) was scanned over a CNT-graphene hybrid transistor by a piezo-controlled mirror with nanometer-scale spatial resolution. A photocurrent signal occurs wherever the CNT-graphene hybrid electronic band structure bends: the built-in electric field separates the photo-excited electron and hole pairs and thus produces a current [140]. This current is measured as a function of position, as shown in Figure 2.9a. To locate the position of photocurrent signals, the reflected light from the device was simultaneously recorded by a Si photodetector, which was then overlapped with the corresponding photocurrent image.

Strong photocurrent responses were observed in some regions, corresponding to the junctions between graphene grains in the CNT-graphene hybrids as illustrated in the SEM images (Figure 2.9b-d). The cracked areas observed in the SEM images are due to the surface tension of water during the transferring process, even though graphene is framed by the randomly-distributed CNT networks. As discussed above, the CNT networks might be partially unzipped into nanoribbons, which can stack onto the graphene surface and glue graphene grains together. Such strong photocurrent response, as demonstrated in previous reports [130-132], may contribute to the unzipped nanoribbons stacking on top of graphene, where the band misalignment occurs due to the coupling between the edges of the nanoribbons and the graphene layer underneath [141].
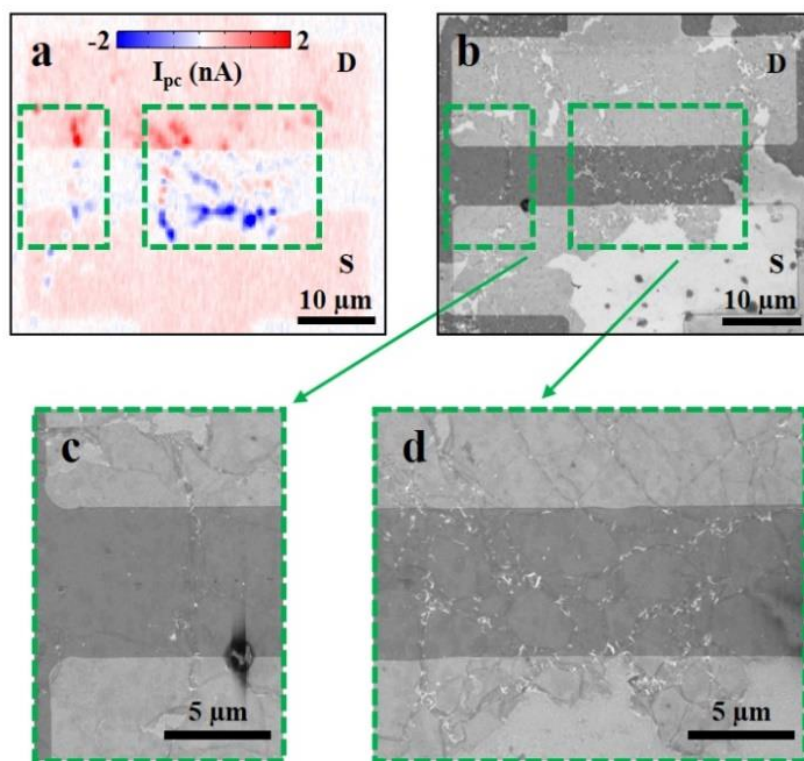
Figure 2.9 (a) An overlay image of photocurrent and reflection of a CNT-graphene hybrid transistor; (b) the corresponding SEM image; and (c)-(d) the zoom-in SEM images of regions marked by green dashed rectangles in (b).

We developed a simple method to synthesize ultra-thin CNT-graphene hybrids, in which single-layer randomly-distributed CNT networks are partially unzipped into nanoribbons that can act as glue to connect different graphene grains together to improve their mechanical strength. Gate-dependent studies indicate that CNT-graphene hybrids inherit the remarkable electrical properties from graphene and have relatively higher turn-on conductance than the CNT networks. Scanning photocurrent measurements show that there are strong photocurrent signals in the junction area between different graphene grains, which may result from the stacking between graphene and CNT-unzipped nanoribbons. Introduction of CNT frames into graphene to enhance the linkage between different graphene

41

grains may provide a new way toward a producing promising graphene hybrid structures for future applications in electronics and optoelectronics.

CHAPTER 3

INTEGRATION OF ALIGNED SWNTs AND MoS$_2$

In this chapter, I first discuss CVD approaches to synthesize aligned SWNTs and related characterizations. Particularly, I report a method of fabricating suspended aligned SWNT transistors on coverslips, which might be suitable for future applications. Then I describe the CVD approach for monolayer MoS$_2$ on two different substrates, quartz and SiO$_2$/Si. Lastly, I report the extended research of synthesizing aligned SWNTs and MoS$_2$ films together to form hybrids. The hybrids can be visualized under the microscope and have outstanding optoelectronic properties in a wide wavelength.

3.1 CVD Synthesis of Aligned SWNTs

Many techniques have been developed to produce carbon nanotubes with specific alignment, density, and even chirality in a large scale [142-144]. Among them, CVD has been widely used for CNT synthesis due to the low cost and the simplicity for wafer-scale production. For instance, slow vacuum filtration has been used to obtain wafer-scale monodomain films of highly-packed aligned SWNTs with a density of 10^6 nanotubes in a cross-sectional area of 1 µm^2 [142]. These thickness-controllable and chirality-enriched SWNT films can be made as semiconductor-enriched devices with polarized electronic and optoelectronic properties [142]. Another approach with novel catalysts called Trojan or Trojan-Mo has recently been developed to synthesize high-ratio (> 91%) and high-density (>100 nanotubes per µm) semiconducting-SWNT arrays through CVD [143].

During a typical CNT synthesis, a sample with catalyst, will be put in a furnace and heated up to the desired temperature with the presence of carbon-containing gases like CH$_4$ or C$_2$H$_2$. Depending on the conditions and the substrate used, the resulting CNTs could be in

43

different forms, such as randomly-distributed CNT network, vertically-aligned CNT forests, or horizontally-aligned CNT arrays. My research is centered on the synthesis and application of horizontally-aligned CNT arrays.

Here I adopted a CVD method [20, 145] to synthesize high-density and super aligned CNT arrays of relatively long SWNTs on stable temperature (ST)-cut quartz substrates obtained from Hoffman Material Inc [12, 145]. To be better applied in the wet transfer process, we cut the 4-inch quartz wafer into 1 cm square pieces through dicing saw. The catalyst solution consists of $CuCl_2$ and polyvinylpyrrolidone (PVP) in the alcohol solution. We patterned a mask by attaching Scotch tapes on the substrate and cutting lines with a flat steel blade. Then the catalyst solution was glued onto the mask with a sponge swap and evaporated. Finally, the line-shape patterns of catalyst were left on the surface after removal of Scotch tapes (Figure 3.1a). The substrate was pre-annealed at 685 ℃ in the air for 30 minutes to oxidize the copper composites. The atmospheric growth was first followed with a flow of 200 sccm H_2 at 685 ℃ for 30 minutes and later with an additional flow of 50 sccm Ar through one alcohol bubbler at a higher temperature 815 ℃ for another 30 minutes (Figure 3.1b). The samples were naturally cooled down to room temperature. More experimental details are given in the appendix.
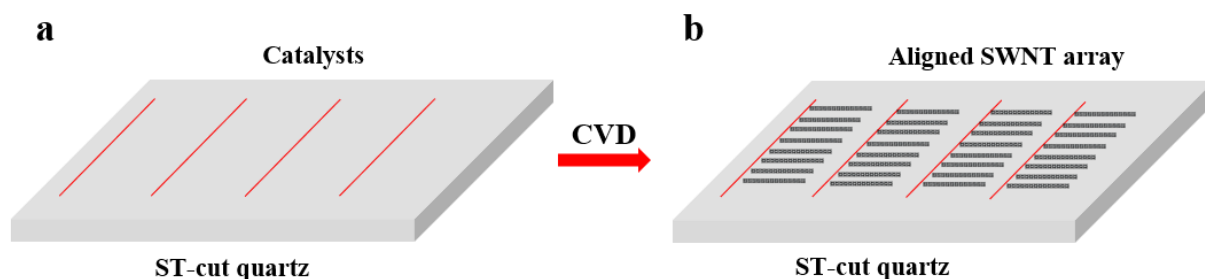
Figure 3.1 Schematic illustrations of the catalyst preparation (a) and synthesis of horizontally-aligned SWNT arrays (b).

After growth, we spin-coated a thin layer of PMMA at 4000 rpm for 45 seconds on top of the ST-cut quartz substrate. Dry the sample in the air for at least 2 hours before the wet transfer process. After that, the sample was etched in a hot KOH solution (1 mol/l) for 5 minutes. Then the PMMA/CNT film was easily peeled off from the substrate to the DI water. The DI water bath was repeated at least 3 times to completely clean the film. Lastly, we transferred the PMMA/CNT film to the target substrate and dried it in the air. Again, PMMA can be removed by either annealing in furnace at 400 °C, or soaking in acetone/IPA/DI water. The direction of aligned SWNT film is usually parallel to the sides of quartz substrates so I can easily control the directions of SWNTs in the transfer process. Here we transferred two SWNT films on a Si/SiO$_2$ substrate at perpendicular directions to form networks (Figure 3.2).
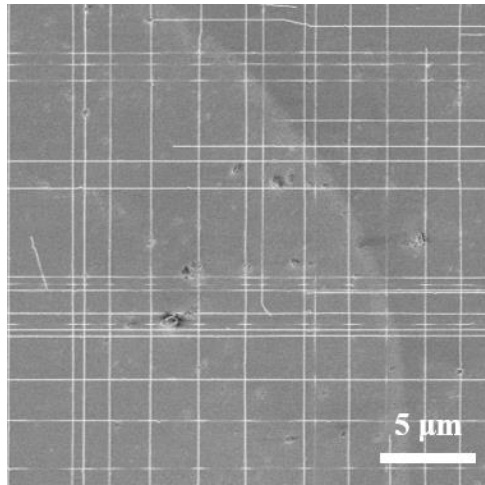
Figure 3.2 a SEM image of SWNT network.

3.1.1 SEM, Raman and AFM Characterizations

The growth condition of SWNTs on each quartz substrate is investigated through SEM. Figure 3.3a shows two high-density SWNT arrays grown on ST-cut quartz substrates. The length of SWNT can reach more than 0.5 mm. In a small scale, we can estimate that the density of SWNT films is about 1~5 nanotubes/µm (Figure 3.3b).
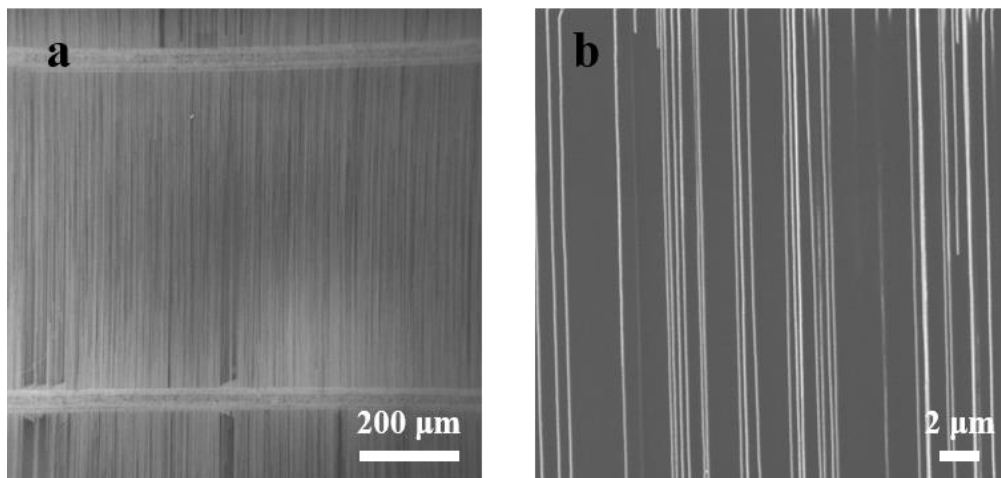
Figure 3.3 SEM images of high-density SWNT arrays in (a) large and (b) small scale.

Like graphene, there are many features for SWNTs that can be identified with

46

specific Raman spectra. It can provide abundant information about the exceptional 1D properties which includes the electronic structure, diameter of nanotubes and sample defects. To avoid the influence of peaks from ST-cut quartz substrate (~127 cm^{-1} and ~ 205 cm^{-1}), we directly transferred the SWNT arrays onto Si substrate with 300 nm SiO$_2$ layer, and later conducted Raman spectroscopy.
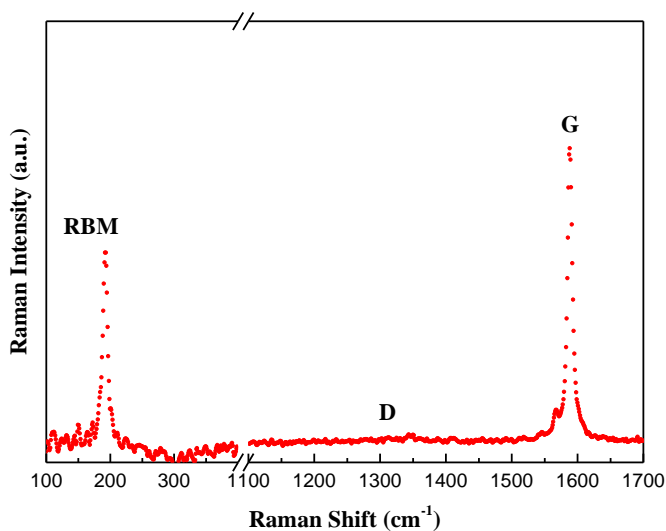
Figure 3.4 A typical Raman spectrum of SWNT.

For SWNTs, two typical strong bands were observed (Figure 3.4): a diameter-dependent radial breathing mode (RBM) at ~ 194 cm^{-1}, a disorder mode (D) at ~ 1330 cm^{-1}, and a tangential mode (G) at ~ 1590 cm^{-1}. According to the $\omega_{RBM}(cm^{-1}) = 234/d_t\ (nm) + 10$ relation [138, 139], we obtain the diameter of randomly-distributed CNTs to be ~ 1.27 nm, which is the typical diameter of SWNT grown on ST-cut quartz substrates as reported [20, 145]. Also, Raman spectra at multiple excitation laser can be used to distinguish the semiconducting and metallic SWNTs [12]. In our experiment, most of SWNTs are semiconducting nanotubes via this adopted method.

AFM is a powerful tool of measuring the morphology and roughness of a sample

surface at a high resolution. Here we show an AFM image of SWNTs on ST-cut quartz substrate (Figure 3.5a). From the profile in Figure 3.5b, we can estimate that the diameter of SWNTs ranges from 0.7 nm to 2.2 nm.
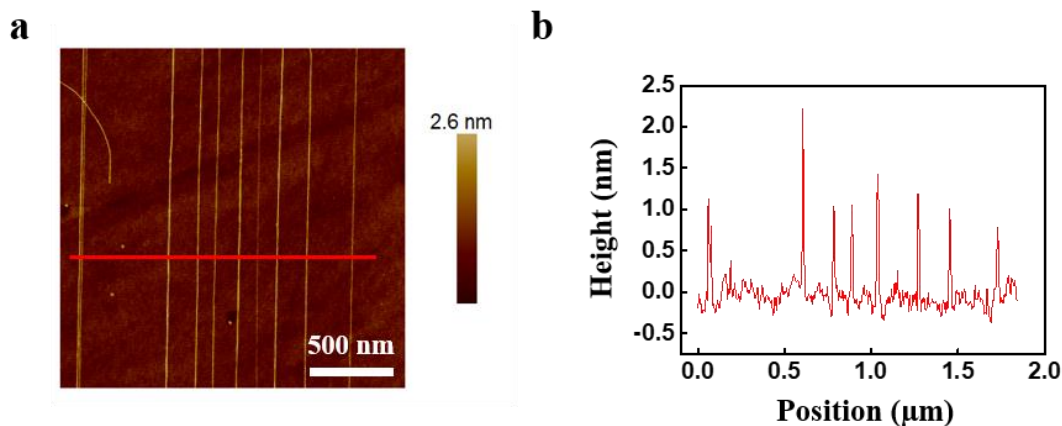
Figure 3.5 (a) AFM image of aligned SWNTs on ST-cut quartz substrate. (b) A profile of SWNTs marked in (a).

3.1.2 Electronic and Optoelectronic Properties

After we obtain the aligned SWNT film, we transfer it onto a transistor, in which the gap between two prepatterned electrodes is 5 µm (Figure 3.6a). To form a better contact, the device goes through an annealing process with 100 sccm Ar at 150 °C. After that, we performed the electrical transport measurements for SWNT transistors. As shown in Figure 3.6b, when the gate voltage swept from -3 V to 4 V, the conductance of horizontally-aligned SWNTs was collected at a source-drain bias of 50 mV. It displays p-type characteristics at zero gate bias, which is consistent with other reports [12].
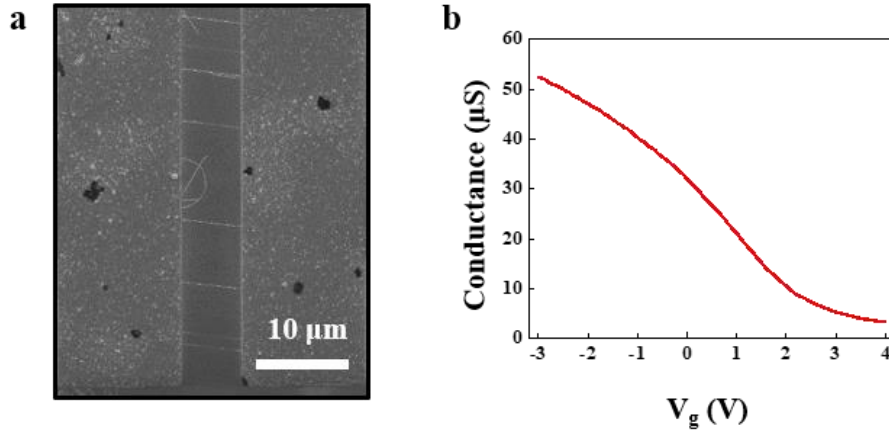
Figure 3.6 (a) SEM image and (b) gate-dependent measurements of an aligned SWNT transistor.

To avoid the interactions between SWNTs and SiO_2/Si substrate, we also performed initial experiments with aligned SWNTs in suspension and measured the electronic and optoelectronic properties. To suspend the SWNT off the SiO_2/S_i substrate, we soaked the device into Buffered Oxide Etch (BOE, 1:10) solution for 2 minutes to etch the 300 nm thin films of SiO_2. Then we cleaned it through water bath twice to remove the residual of BOE. Finally, the device went through an IPA bath and dry in the air before any measurements. To avoid breaking any nanotube, we applied the alcohol solution in the final step, the surface tension of which is relatively smaller than that of water [146]. Note that BOE residual is collected under supervision.
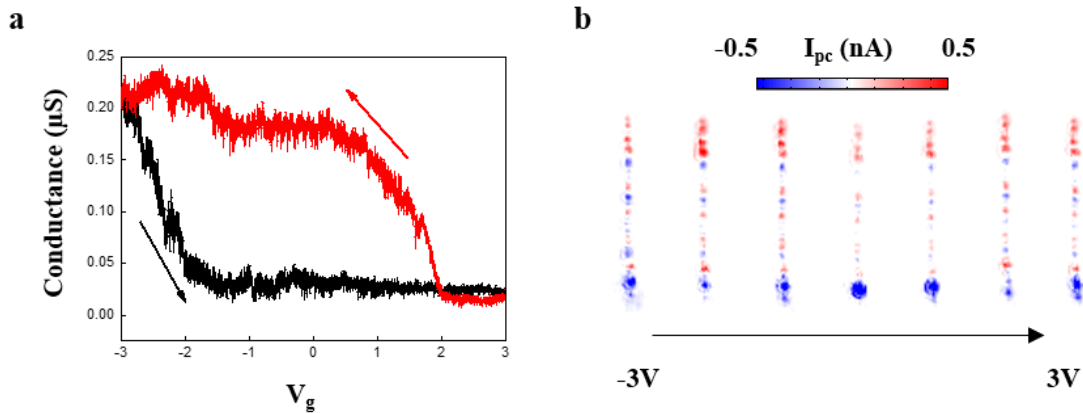
Figure 3.7 Gate-dependent (a) electronic measurements and (b) optoelectronic measurements of a suspended SWNT transistor.

Similar gate-dependent measurements have been performed on suspended SWNT transistors. As shown in Figure 3.7a, when the gate voltage swept from -3 V to 3 V, the conductance curve still shows a p-type characteristic at zero gate bias. The red curve is different from the black curve because of hysteresis [147]. When the SWNTs are suspended and exposed to the air, there exist significant environmental interactions. Because the density of SWNTs between the electrodes is relatively low, the environmental noise is high in the electronic measurements.

Additionally, it is interesting to explore the optoelectronic properties of suspended SWNT transistors. Figure 3.7b presents the change in photoresponse when we swept the gate from -3 V to 3 V. Following the blue dot in negative scale as an example, it increased in intensity from -3 V to 0 V and decreased from 0 V to 3 V. As discussed, we can control the directions of SWNT arrays at transfer and further produce SWNT networks in two directions. Some initial efforts have been made to produce suspended SWNT network transistor as shown in Figure 3.8. Even though suspended SWNTs are arduous to handle in the

experiments, there is a great potential that we can extend the SWNT network transistor to other work such as biosensors.
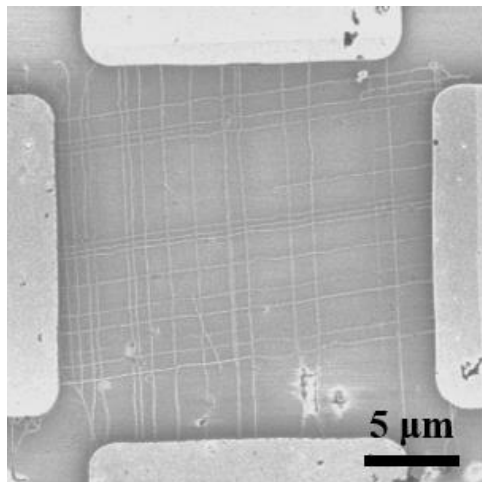
Figure 3.8 SEM image of a suspended SWNT network transistor.

Not only can we transfer SWNT arrays onto SiO_2/Si substrates, we can also fabricate SWNT transistors on coverslips for bioengineering applications. The transparency of glass substrates is convenient for collaboration with other groups. Figure 3.9 illustrates the photoresponse of aligned SWNT on the coverslips. Here we take advantage of the bioengineering design that will be discussed in CHAPTER 4. Briefly, the electrode arrays were fabricated on coverslips. At transfer, there is a high chance that we can obtain 1 ~ 15 aligned SWNTs on each transistor, which is suitable for biosensing applications. Note that we have combined these transistors with cancer cells in the initial experiments.
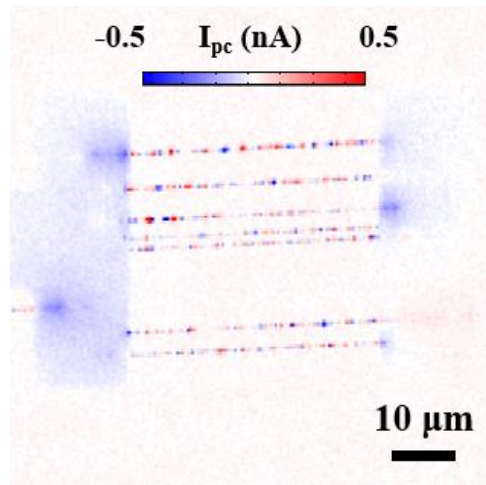
Figure 3.9 Photoresponses of a SWNT transistor on coverslip substrate.

After we obtained many SWNT transistors on one coverslip, a channel was built above the device to suspend SWNTs by flowing the etching solution. The rate of flow of the solution into the channel is controlled by a valve, which is a key component that affects how SWNTs will be suspended in the channel. As shown in Figure 3.10a, the conductance curve at a gate voltage between -1 V and 1 V shows consistent p-type characteristic of SWNTs. Figure 3.10b illustrates that strong photoreponses of suspended SWNTs occur after the etching. It is possible that the flow of solution inside the channel can enable the bundling of aligned SWNTs, leading to a strong photoresponse. Previous work in our lab has shown strong photoresponses when the graphene ribbons were curled [130]. This initial work can be extended as a future project. Furthermore, we can observe the bundled SWNTs from the reflection signals (Figure 3.10c), which helps advance our research of SWNT-MoS$_2$ hybrids later. We can also coat sulfur balls onto SWNTs films by heating sulfur powder, which can also help us visualize aligned SWNTs under microscope. This could be future work regarding the mechanical properties of SWNTs.
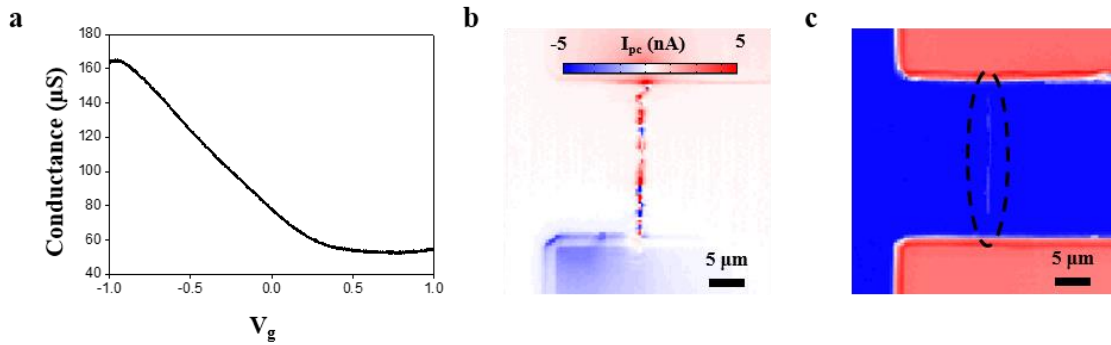
Figure 3.10 (a) Gate-dependent measurements (b) photoresponses and (c) reflection image of a suspended SWNT transistor on coverslip substrate.

3.2 CVD Synthesis of Monolayer MoS$_2$

Many techniques have been developed to produce MoS$_2$ in sizable quantities. Here we adopted a standard method to synthesize MoS$_2$ on SiO$_2$/Si substrates and extend it to quartz substrates. The SiO$_2$/Si substrates have been pre-treated by a piranha solution mixed by 30 mL H$_2$SO$_4$ (98%) and 10 mL H$_2$O$_2$ (30%) on a heat template at 150 °C. Stir the mixed solution at slow rate will help avoid overheating. The oxidation process usually takes ~ 1h to remove the surface residuals. Later, deionized water and nitrogen gas were used to clean and dry the substrates before MoS$_2$ synthesis.
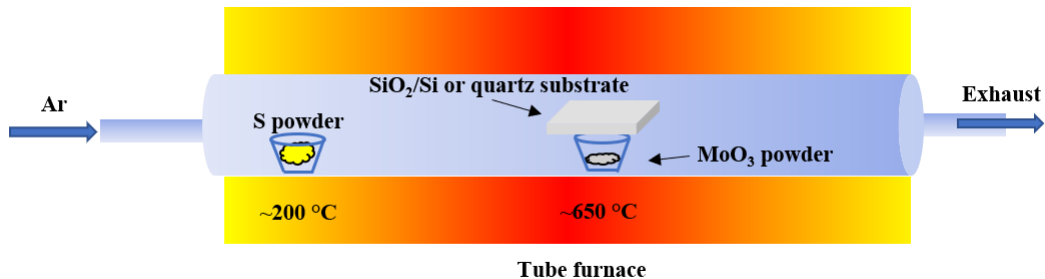
Figure 3.11 Schematic of MoS$_2$ synthesis.

After the pre-treatment, substrates were loaded into a one-inch quartz tube and placed

53

face-down above a quartz boat containing 10 mg of MoO_3 (99.95% Alfa Aesar #11837) with another boat containing 300 mg sulfur (99.5% Alfa Aesar #43766) located in the upstream area (Figure 3.11). The distance between sulfur and MoO_3 was 18 ~ 21 cm for SiO_2/Si and 16 ~ 18 cm for quartz substrates, which was optimized for monolayer MoS_2 growth. The furnace was first pumped down to 0.8 Torr, refilled with ultrapure Ar until 550 Torr, and repeated once. Later, the furnace was heated up to 650 °C at 30 °C per min with a 10 sccm Ar flow. The sulfur was about to sublime at ~ 200 ℃, while the temperature of the middle part of the furnace ramped up to 650 °C for 5 min and then cooled down to 500 °C for 10 min. Finally, we opened the furnace lid and added a 500 sccm Ar flow for rapid cooling.
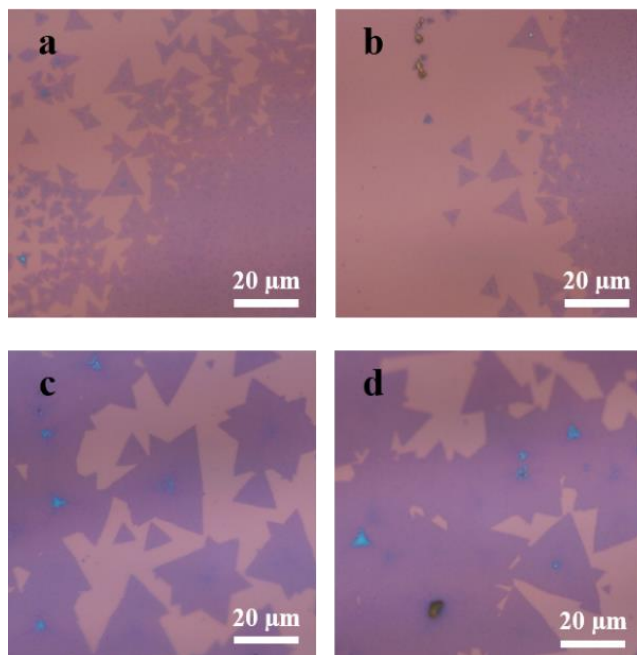
Figure 3.12 (a) – (d) Optical images of MoS_2 films synthesizing with different growth conditions. Large-area MoS_2 flakes were obtained by tuning the parameters such as flow rate, growth temperature, and locations of sulfur and MoO_3 powders.

The substrates were examined with an optical microscope. It is interesting to see that

monolayer MoS_2 films are located near the edges of the substrates. Figure 3.12 shows optical images of MoS_2 films under adjusted growth conditions. The side length of MoS_2 films can reach 20 µm.

3.2.1 Raman and Photoluminescence Spectra
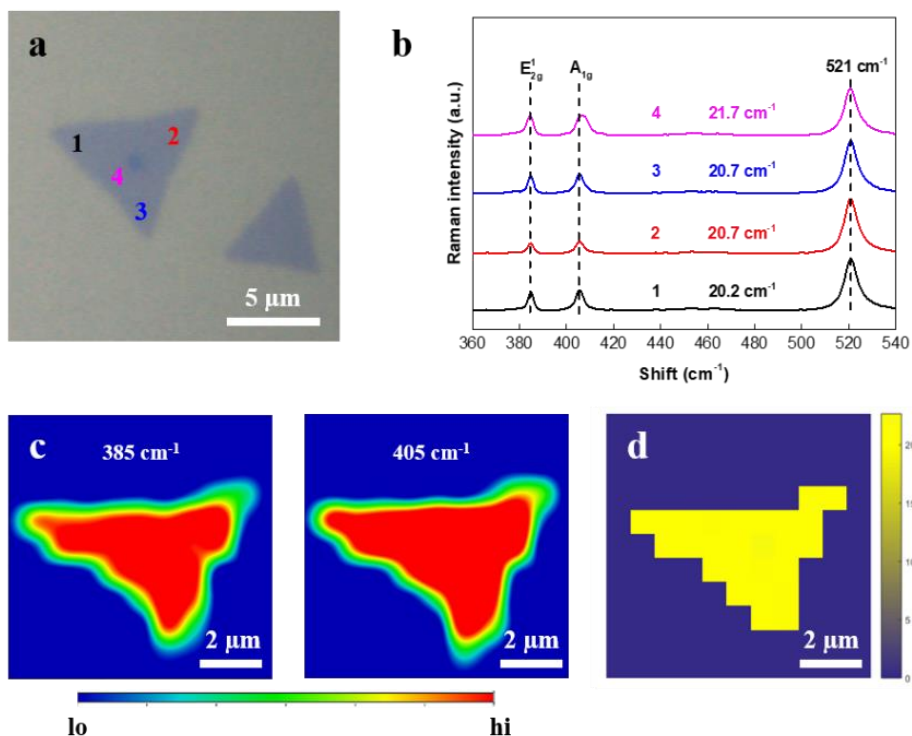
Figure 3.13 (a) Optical image of a triangular MoS_2 flake. The three corners and center part were marked as 1,2,3,4. (b) Raman spectrum for each point was recorded through a 532 nm laser. (c) Mapping images in terms of intensity for two peaks at 385 cm^{-1} and 405 cm^{-1}. (d) A mapping image for peak distance at each spectrum.

Raman microscopy can be applied to explore many features of MoS_2 such as thickness and photoluminescence. To begin with, we conducted Raman spectra mapping of a triangular MoS_2 films with ~ 8 µm side length (Figure 3.13a). To compare the Raman spectrum at different locations, we choose the corner and central part of this triangular film.

Figure 3.13b shows the Raman spectra of these 4 locations by a 532nm laser under ambient conditions. For MoS$_2$, two typical strong bands were observed (Figure 3.13b): E$_{2g}^1$ mode at ~ 385 cm^{-1} and A$_{1g}$ mode at ~ 405 cm^{-1}. The distance between two peaks can identify the thickness of MoS$_2$ films [148]. For corner locations, we observed the distance between E$_{2g}^1$ and A$_{1g}$ ranges from 19.8 cm^{-1} to 20.7 cm^{-1}, which is consistent with CVD-grown monolayer MoS$_2$ as reported [149]. However, we observed the distance between two modes is 21.7 cm^{-1}, which is typical for multilayer MoS$_2$. From the optical image, we can see some dots at the center of this triangular films in Figure 3.12c and Figure 3.13a, which might be seen as seeds that help grow large-area and uniform MoS$_2$ films [98]. In addition, we plot the spectra mapping in terms of E$_{2g}^1$ mode, A$_{1g}$ mode and distance between two modes as shown in Figure 3.13c and Figure 3.13d. These mapping images shows our CVD-grown MoS$_2$ is uniform.

Not only can we see Raman scattering to investigate the thickness and quality of MoS$_2$ film, we can also conduct photoluminescence spectroscopy on the four locations shown in Figure 3.13a. As shown in Figure 3.14a, the spectrum peak is observed at ~ 673 nm corresponding 1.84 eV photon energy, which is consistent with reported results [150]. Similarly, a photoluminescence mapping has been conducted for this film in Figure 3.14d, indicating a uniform monolayer MoS$_2$ film except the multilayer at the center with a relatively low photoluminescence intensity. These results agree with our previous Raman spectra, which implies the uniform distribution of CVD-grown MoS$_2$ films. Furthermore, the growth mechanism about seeds helps explain the extended research of SWNT-MoS$_2$ hybrids discussed in CHAPTER 3.
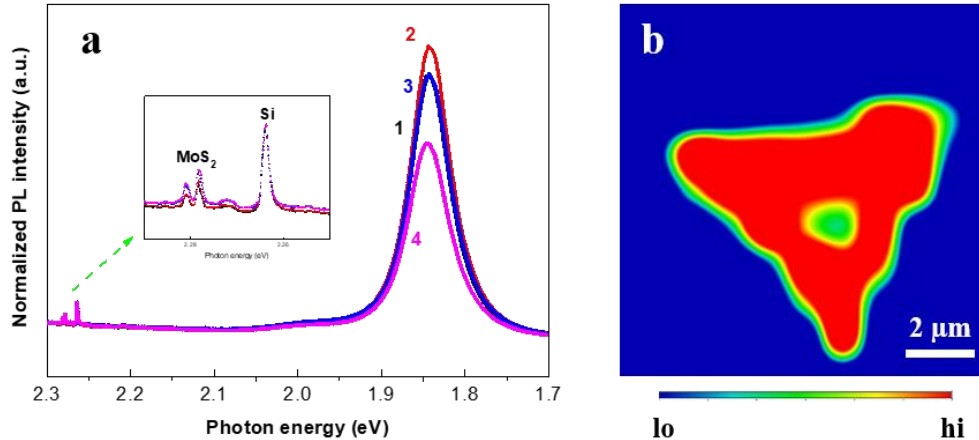
Figure 3.14 (a) Photoluminescence spectrum for each point shown in Figure 3.13a. A zoom-in image is consistent with Raman spectrum above. (b) A mapping image of peak intensity at 673 nm.

3.2.2 CVD-grown Single-layer MoS_2 Transistor

After verifying the quality MoS_2 by Raman and photoluminescence spectroscopy, MoS_2 transistors were fabricated to explore its electronic and optoelectronic properties. As shown in Figure 3.15a and Figure 3.15b, we can observe strong photoresponses at the junctions between metal and MoS_2 films [151]. To test the mobility of this transistor, we swept the gate voltage from -20 V to 50 V at $V_{sd} = 100$ mV. The conductance curve indicates an n-type characteristic at zero bias. By calculating the conductance slope between 35 V and 50 V, we are able to calculate the mobility to be ~ 0.34 $cm^2 V^{-1} s^{-1}$, which is consistent with CVD-grown MoS_2 transistors as reported [149, 152-154].
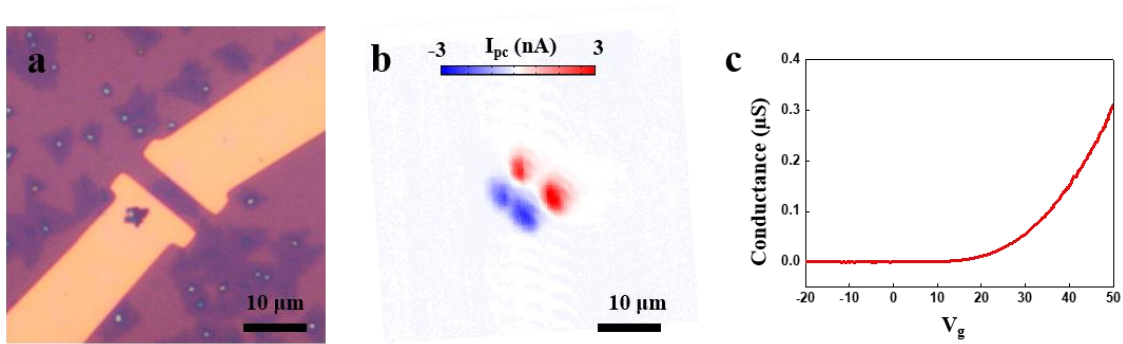
Figure 3.15 (a) Optical image, (b) photoresponses and (c) gate-dependent measurements of a MoS_2 transistor.

3.3 Probing Aligned SWNTs Doped Ultrathin MoS_2

In this section, I report a facile method to produce ultrathin MoS_2 hybrids with polarized near-infrared (NIR) photoresponse, in which horizontally-aligned SWNTs are integrated with single- and few-layer MoS_2 through a two-step CVD process. The photocurrent generation mechanisms in SWNT-MoS_2 hybrids are systematically investigated through wavelength- and polarization-dependence scanning photocurrent measurements. When the incident photon energy is above the direct bandgap of MoS_2, isotropic photocurrent signals are observed, which can be primarily attributed to the direct band gap transition in MoS_2. In contrast, if the incident photon energy in the NIR region is below the direct bandgap of MoS_2, the maximum photocurrent response occurs when the incident light is polarized in the direction along the SWNTs, indicating that photocurrent signals mainly result from anisotropic SWNTs absorption. More importantly, these 2D hybrid structures inherit the electrical transport properties from MoS_2, displaying n-type characteristics at zero gate bias. These fundamental studies provide a new way to produce ultrathin MoS_2 hybrids with inherited electrical properties and polarized NIR photoresponse,

opening doors for engineering various 2D hybrid materials for future broadband optoelectronic applications.

3.3.1 Motivation

Two-dimensional materials with a layered structure such as TMDC family have attracted a large amount of interest owing to their unique properties [88, 91, 150] and advancement in synthesis techniques [102, 155]. As a member of the TMDC family, MoS_2 shows promising transistor performance with a room-temperature current on/off ratio of 10^8 [90]. The intrinsic direct bandgap for monolayer MoS_2 is 1.9 eV, whereas bulk MoS_2 is an indirect-bandgap semiconductor with a bandgap of 1.2 eV [90, 91, 150], which is suitable for optoelectronic applications in the visible spectral region [156]. For example, metal-MoS_2-metal devices have exhibited a high photoresponsivity of 880 A/W at a wavelength of 561 nm, where strong photocurrent signals are generated at the metal-MoS_2 junctions [156].

However, the sizeable bandgap (> 1 eV) of MoS_2 restricts its optoelectronic applications in the NIR spectral region. The photoresponse of MoS_2 photodetectors would decrease drastically under the illumination of 785 nm (1.6 eV) and 1550 nm (0.8 eV) lasers, where the phonon energies are not enough to excite electrons from the valence band to the conduction band of MoS_2 [151]. Various hybrid structures have been developed to extend the optoelectronic applications of MoS_2 in the NIR fields [157-159]. Atomic p-n heterojunctions between MoS_2 and black phosphorus (BP) have been fabricated as photodiodes, where BP, a novel semiconducting material with a thickness-dependent direct bandgap from 0.3 eV to 2 eV [160, 161], has been utilized to enhance the photoresponses of photodiodes in the NIR spectral region [157-159]. However, the mechanical exfoliation as well as complicated transfer processes involved in the fabrication of these devices limit their potential applications for mass production. It is, therefore, desirable to develop a method of

producing 2D hybrid materials that inherit the electrical performance from TMDCs and exhibit enhanced photoresponse in the NIR spectral region.

SWNTs, 1D carbon-based nanomaterials, have gained much attention due to their fascinating features [120, 122, 162, 163]. Recently, highly-efficient generation of electron-hole pairs (EHPs) have been reported in SWNT p-n junctions, where a single photon can induce multiple EHPs [164]. Moreover, carbon nanotubes can absorb light with wavelengths ranging from 200 nm to 200 µm due to a wide distribution of nanotube diameters that leads to various bandgaps for individual nanotubes [165]. Thus, carbon nanotubes are promising add-on components for future broadband optoelectronics [166].

Here we report a two-step CVD method to synthesize ultrathin SWNT-MoS_2 hybrids with enhanced NIR photoresponses. This hybrid material can easily be visualized under an optical microscope, making the subsequent optical and electrical characterization much easier. Interestingly, enhanced Raman intensities of MoS_2 modes are observed in the areas where aligned SWNTs are located, indicating MoS_2 aggregation or graphitic substrate may influence the Raman spectra of MoS_2. We also find that the hybrid material possesses similar electrical property as MoS_2 and inherits the optoelectronic properties from both MoS_2 and SWNTs. Under 650 nm illumination, the hybrid displays isotropic photoresponses, suggesting the photocurrent signals are mainly attributed to MoS_2 absorption. However, the photocurrent response is polarized along the SWNT direction when the wavelength of the incident light is 850 nm, a typical behavior for SWNT absorption. This indicates SWNT arrays can help enhance the photoresponse of MoS_2 in the NIR spectral region. Combining unique properties from two materials, these SWNT-MoS_2 hybrids may provide new avenues to the development of 2D hybrid materials toward future broadband optoelectronic applications.

3.3.2 Experimental Methods

Based on the growth method discussed previously, we first synthesize high-density aligned SWNT arrays on quartz. Subsequently, MoS_2 was synthesized atop horizontally-aligned SWNTs to form hybrid structures. The distance between sulfur and MoO_3 was 16-18 cm, which was optimized for monolayer MoS_2 growth on ST-cut quartz. Note that this distance is different from the optimized distance of monolayer MoS_2 growth discussed in page 53. In addition, we did not apply piranha solution in the preparation process to avoid the oxidation of SWNT arrays. The hybrid films are transferred from quartz to SiO_2/Si substrates by using a hot KOH solution.

3.3.3 Results and Discussion

At each stage of the synthesis, the samples were visually characterized under an optical microscope (Olympus BX51WI). On nearly transparent quartz substrates, SWNTs cannot be observed after the first growth. However, they can be clearly imaged as white lines under optical microscope after the subsequent growth of MoS_2 (Figure 3.16a). Similar results have been reported previously, where nanotubes can be observed under optical microscopes with the help of either TiO_2 nanoparticles [167] or water vapor [168]. SEM was also used to investigate these SWNT-MoS_2 hybrids for detailed information. As shown in Figure 3.16b, aggregated MoS_2 flakes were observed along each SWNT, leading to the 'line-shape' contrast and allowing us to observe them under an optical microscope. Recently, researchers have obtained large-area MoS_2 films by utilizing different molecules as seeding promoters [98]. Here SWNTs may act as seeds for initial nucleation of MoS_2 films, likely resulting in the aggregation of MoS_2 flakes along the nanotubes.
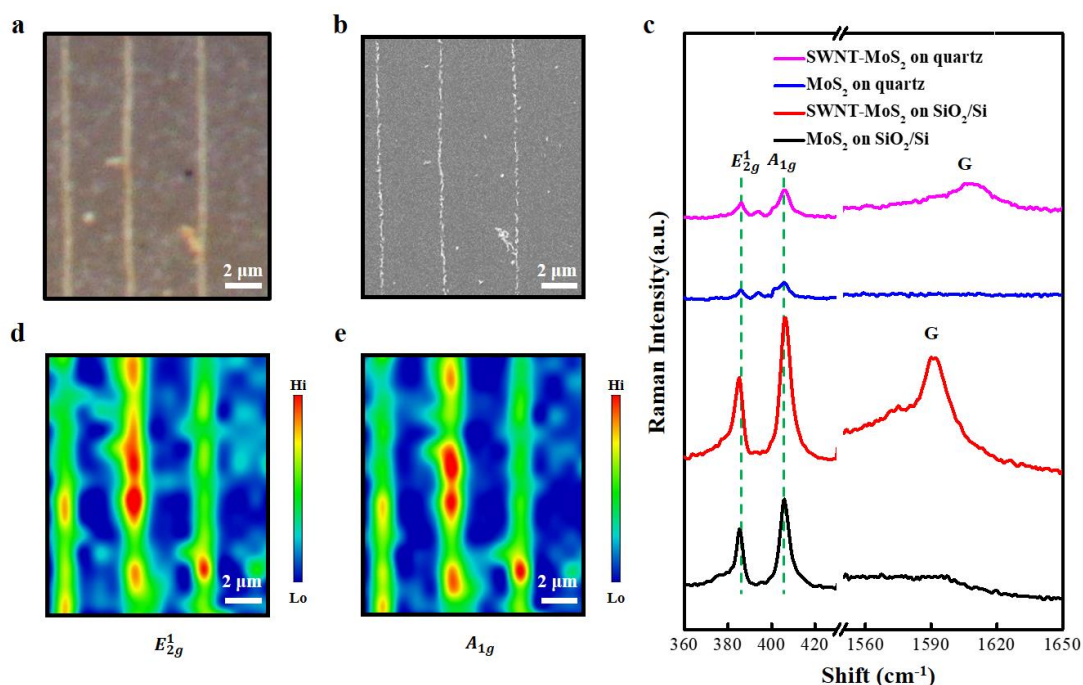
Figure 3.16 (a) Optical and (b) SEM images of SWNT-MoS$_2$ hybrids on quartz substrates. (c) Raman spectra of SWNT-MoS$_2$ hybrids on different substrates. Raman mapping images of (d) E$_{2g}^1$ and (e) A$_{1g}$ modes of SWNT-MoS$_2$ hybrids on quartz substrates, respectively.

Moreover, the visually-recognizable SWNT-MoS$_2$ hybrids make the subsequent Raman characterization much easier. Raman spectra were collected at room temperature through a Thermo Scientific DXR Raman spectrometer from 100 to 1800 cm^{-1}. A 532 nm laser beam was focused into a diffraction-limited spot (~ 1 µm) by a 100X Olympus objective. Figure 3.16c displays that the intensities of MoS$_2$ mode (E$_{2g}^1$ and A$_{1g}$) are higher at the locations where G peaks of SWNTs are observed than those of other spots. Similar results are also presented in the Raman mapping of the hybrid, where strong E$_{2g}^1$ and A$_{1g}$ modes are present in the 'line-shape' areas (Figure 3.16d and Figure 3.16e), suggesting that the Raman enhancement is likely due to the aggregated MoS$_2$ flakes along SWNTs. The

SWNT substrate may also facilitate the charge transfer between MoS_2 and SWNTs and influence the Raman spectra of MoS_2. Previous Raman studies of MoS_2 films on graphene plate have demonstrated that the photoelectrons could easily transfer between two layered materials and then affect the Raman signals [169, 170]. Another possible reason for enhanced Raman signals is that SWNT substrates could help enhance the Raman signals of MoS_2 films by reducing the substrate interference [171]. Also, layered MoS_2 is a hexagonal arrangement of Mo and S atoms in a sandwich structure, which is similar to the honeycomb structure of graphene and SWNTs. The structural similarity between SWNTs and MoS_2 may add to the vibrational coupling at such interfaces and lead to the Raman enhancement [172]. Interestingly, the G band of SWNTs is observed at 1605 cm^{-1} on quartz substrates, an "up-shift" band compared with 1590 cm^{-1} on SiO_2/Si substrates. This "up-shift" behavior may result from the strong interaction between SWNTs and quartz substrates, which can deform the C-C bonds in SWNTs and thus affect the atomic vibration during Raman spectroscopy [173]. After the hybrids were transferred from quartz to SiO_2/Si substrates, the structural deformation disappeared at interfaces and thus G band returned to 1590 cm^{-1} (Figure 3.16c), a typical frequency for SWNTs.

Next, we investigated the electrical transfer performance of SWNT-MoS_2 hybrids in two different directions. As shown in Figure 3.17, when the gate voltage swept from -20 V to 80 V, the conductance of the hybrid in the direction perpendicular to SWNT arrays was recorded under a source-drain bias of 100 mV. The device exhibits n-type electrical characteristics at 0 V gate voltage, a typical electrical transport property of CVD-grown MoS_2 [149, 174]. Similar electrical behavior was also observed for the hybrid in the direction parallel to SWNTs (black curve, Figure 3.17), indicating that the electrical transport property of the hybrid is dominated by MoS_2 films. As discussed, a horizontally-aligned SWNT arrays

based transistor displays p-type characteristics at zero gate bias, which is consistent with other reports [12], but different from our SWNT-MoS$_2$ hybrids. With the second growth of an ultrathin MoS$_2$ layer on top of SWNTs, the electrical transfer characteristics changes from p-type to n-type and becomes dominated by MoS$_2$ films, likely due to the relatively low density of 1D SWNTs in comparison with 2D MoS$_2$ films. It is obvious that these SWNT-MoS$_2$ hybrids inherit the electrical transport properties from MoS$_2$.
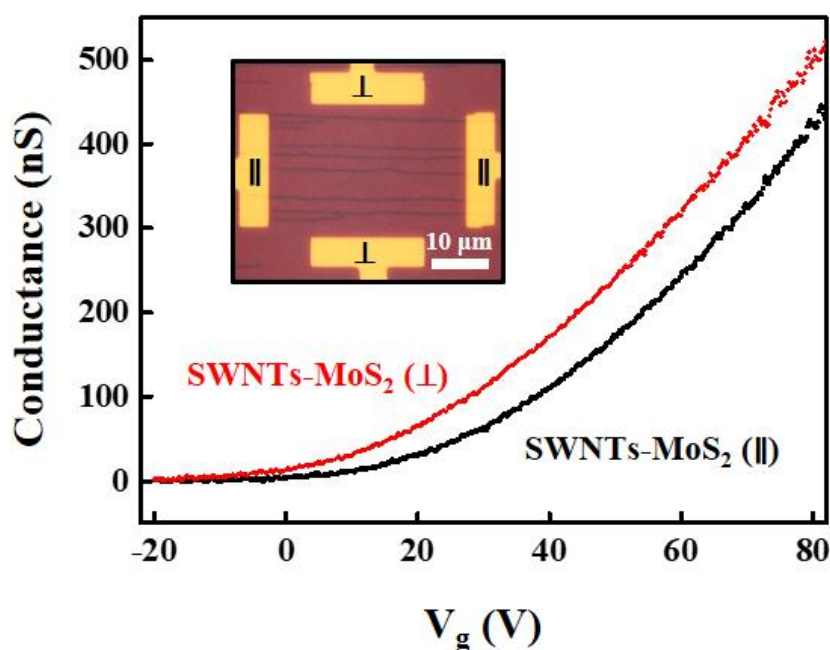
Figure 3.17 Gate-dependent measurements of a SWNT-MoS$_2$ transistor in the directions: perpendicular (black curve) and parallel to (red curve) the aligned SWNTs, respectively. Insets: optical image of a SWNT-MoS$_2$ hybrid transistor.

To study the optoelectronic properties of SWNT-MoS$_2$ hybrids, we performed spatially resolved scanning photocurrent measurements with an Olympus BXWI51 microscope (Figure 3.18a). A diffraction-limited laser spot (~ 1 µm) scanned over a SWNT-MoS$_2$ hybrid device by two-axis scanning mirrors with a nanometer spatial resolution and

photocurrent signals were recorded as a function of position, resulting in a spatially-resolved photocurrent map of the device. The reflection of the incident laser beam was simultaneously collected by a Si photodetector to locate the position of photocurrent signals on the device (Figure 3.18b). Under 850 nm illumination (1.46 eV), strong photoresponses were generated in the areas where aligned SWNTs were located (Figure 3.18c), which is likely due to the SWNT absorption since the photon energy is not enough to excite the electron from the valence band to the conduction band of MoS_2.
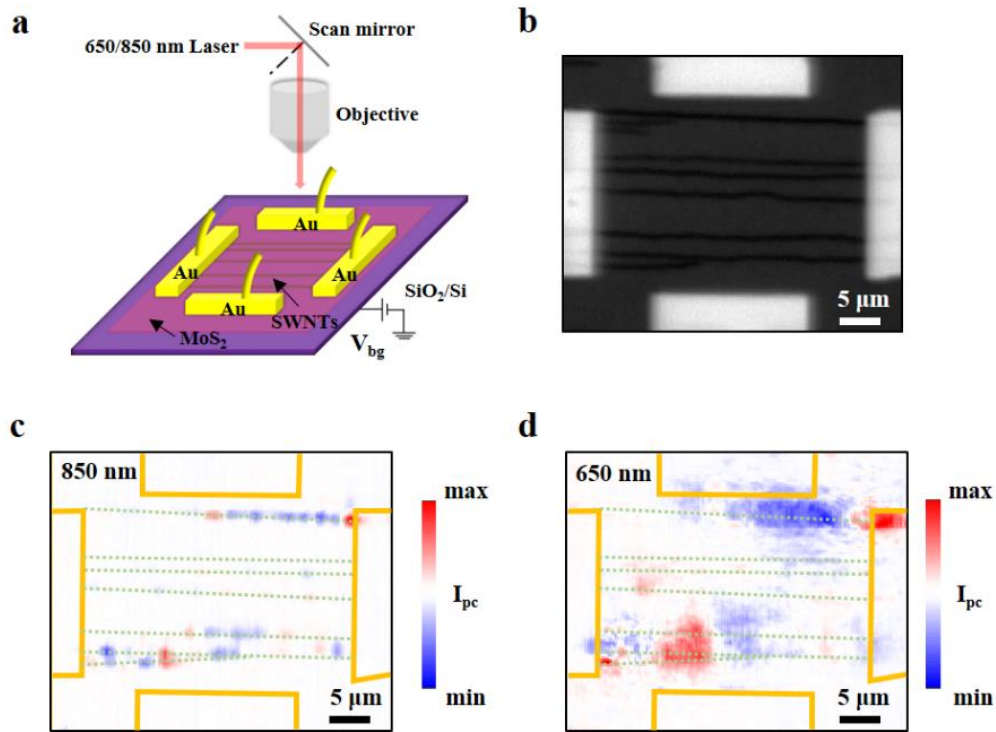
Figure 3.18 (a) Schematic diagram of scanning photocurrent measurement setup. (b) Reflection and scanning photocurrent images of a SWNT-MoS$_2$ transistor illuminated by (c) 850 nm and (d) 650 nm laser, respectively. Note: Electrodes and SWNTs are marked by golden solid lines and green dashed-lines from the reflection image, respectively.

To further explore the relative contributions of different materials to the overall photocurrent response, we performed polarization-dependent photocurrent measurements. As shown in the Figure 3.19a, the measured polarization dependence of the photoresponse in the hybrid is similar to that of a typical SWNT [33], where the maximum signal intensity observed along the SWNT direction ($\theta = 0°$). The polarization effect arises from the one-dimensional geometry of the SWNT, where a smaller part of the incident light can be coupled into the SWNT for the cross-polarized light. The optical selection rules are also important for the polarizability of a nanotube. This suggests that the photocurrent signals mainly result

from nanotubes.
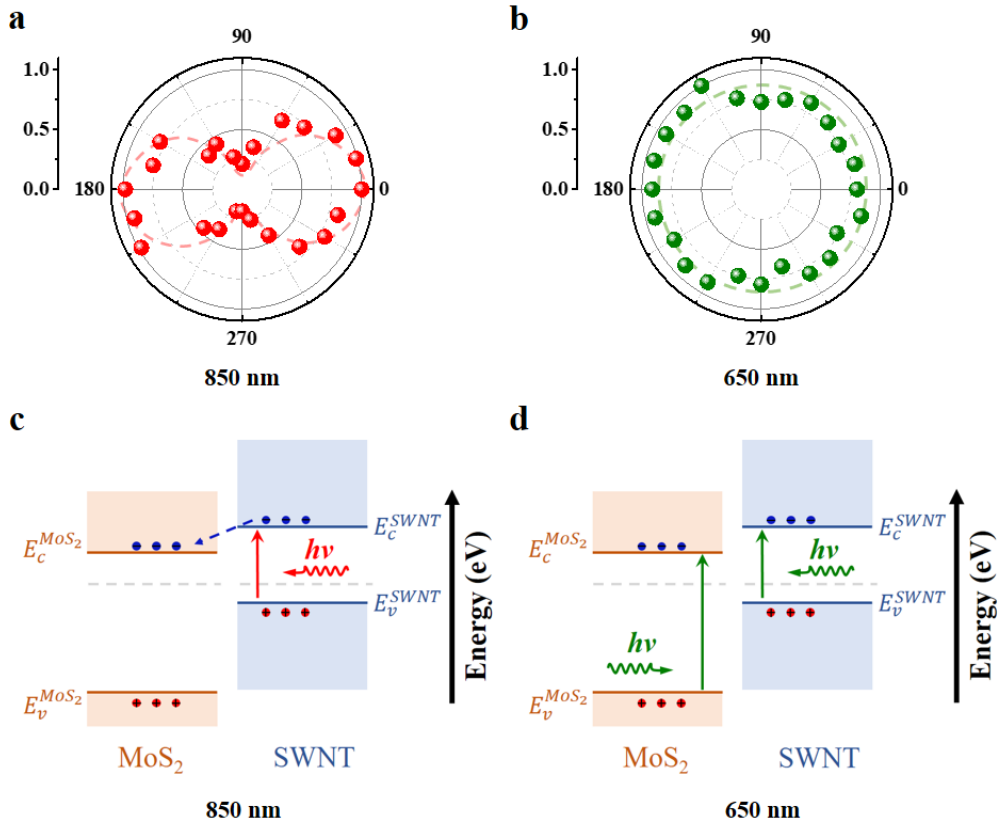
Figure 3.19 Normalized photocurrent intensities at a SWNT-MoS$_2$ interface as a function of (a) 850 nm and (b) 650 nm incident light polarization angle. Gate voltage and source-drain bias were 0 V during the measurements. Schematic illustrations of different mechanisms under (c) 850 nm and (d) 650 nm laser.

As illustrated in Figure 3.19c, a large conduction band offset forms at the SWNT-MoS$_2$ interface due to the Fermi level alignment. As a result, the photo-excited electrons in the conduction band of the SWNT can be injected to the conduction band of MoS$_2$, leading to photocurrent signals at the SNWT-MoS$_2$ interface. Here, we can effectively enhance the NIR photoresponse of MoS$_2$ films by doping SWNTs. On the other hand, the electrons in the valence bands of both MoS$_2$ and SWNTs can be excited to their conduction bands upon

illumination of 650 nm laser (Figure 3.19b). The polarization-dependent photocurrent measurements have shown that photocurrent signals at the SWNT-MoS$_2$ interface are isotropic (Figure 3.18d and Figure 3.19d), suggesting that the photocurrent responses mainly result from MoS$_2$ absorption and the hybrids inherit the optical properties from MoS$_2$ in the visible spectral region.

In summary, we developed a simple method to synthesize ultrathin SWNT-MoS$_2$ hybrids, in which a thin layer of MoS$_2$ helps visualize horizontally-aligned SWNT arrays under optical microscopes. Moreover, with the introduction of MoS$_2$ during the second growth, the electrical transfer characteristics of this hybrid changes from p-type for SWNTs to n-type for SWNT-MoS$_2$ hybrids, indicating that the hybrid materials inherit electrical transport properties from MoS$_2$ films. SWNT-MoS$_2$ hybrids also obtain unique optoelectronic properties from SWNTs in the NIR spectral region. This fundamental study may offer a new way to develop novel hybridized materials, which could provide promising applications for future broadband optoelectronics.

CHAPTER 4

GRAPHENE OPTOELECTRONIC PROBES

In this chapter, we report a graphene optoelectronic probe integrated neuron-glia co-culture microfluidic platform to study the electrical activities of individual synapses and spines of primary embryonic hippocampal neurons with high spatiotemporal resolution. Nanoscale graphene optoelectronic probes enable us to detect millivolt extracellular potential changes of individual synapses and spines during depolarization. The ultrafast feature of graphene photocurrent response allows for decoding a single waveform from the spontaneous bursts of individual synapses and spines at the microsecond level. In addition, the 2D nature of graphene makes it possible to investigate multiple synapses and spines at the same time. Our neurotechnology will provide a new approach for simultaneous spatial mapping of electrophysiological outcomes of individual synapses and spines in neuronal networks.

4.1 Existing Approaches

The central nervous system (CNS) is composed of billions of neurons with trillions of dendritic spines and synapses, through which information is stored and flows among neurons. Synapses, structurally composed of pre- and postsynaptic terminals, permit neurons to pass electrical or chemical signals to individual target cells. Emerging data indicate that individual synaptic connections are unique and can display different activities [175-177]. Thus, it is important to understand the relationships between the functional connectivity map of neuronal networks and the physiological or pathological functions of individual synapses and spines.

The existing approaches for measuring synaptic activity fall into three main

categories: electrophysiology, optical imaging, and microelectrode arrays. The common laboratory technique in electrophysiology is the patch-clamp recording. Several variations of this technique can be applied to study the behavior of individual ion channels, depending on the suction applied through the microelectrode to attach a piece of the plasma-membrane. If more suction is applied, the small patch of membrane in the electrode tip can be displaced, leaving the electrode sealed to the rest of the cell. This "whole-cell" mode allows very stable intracellular recording, as illustrated in Figure 4.1a and Figure 4.1b. From the patch-clamp recording, the membrane potential is about -70 mV at rest and about 20 mV when depolarized. Through this technique, the resulting electrical current, as low as pico-ampere scale (corresponding to flow rates of only 10^{-7} ions per second), can be measured with an ultrasensitive electronic amplifier with sub-millisecond temporal resolution; however, the size of electrodes in most recording is limited in more than one micrometer, which cannot be suitable for probing individual synapses.
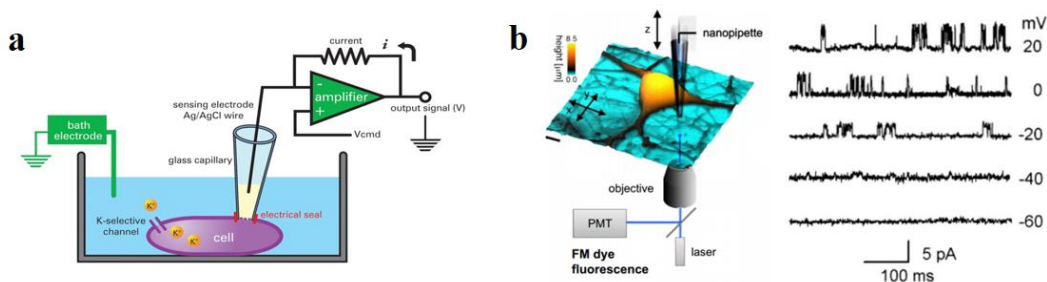
Figure 4.1 (a) Diagram of the whole cell patch clamp technique. (b) Schematic of the experimental set up shown with a typical topographical image of a live neuronal hippocampal culture (left) and current traces recorded in the cell-attached configuration with properties consistent with a Ca^{2+}-activated K^+ channel. Image (a) reprinted with permission from Ref [178]. Copyright © 2010 Discovery Medicine; image (b) reprinted with permission from Ref [179]. Copyright © 2013 Elsevier Inc.

Optical imaging, such as voltage sensitive dyes (VSDs) and calcium sensors, is feasible for neuroscientists to simultaneously obtain information about the source of neural activity as well as its time course, allowing to study neural activity and related functions of the brain. VSD imaging combining with patch-clamping technique, has advanced to record voltage changes in neuronal membranes, that is more analogous to responses recorded in whole cell current-clamp mode as mentioned above [180]. Calcium sensors offer high throughput and record the change of fluorescent intensity of axons and dendrites simultaneously in a relatively large sensing area. GCaMP6 sensors, for example, can measure the organization and dynamics of neural circuits over multiple spatial and temporal scales [181]. As illustrated in Figure 4.2, for different dyes as GCaMP6s and GCaMP6f, simultaneous fluorescence dynamics was recorded by an EMCCD camera while electrical spikes were stimulated through patch-clamping microelectrodes. However, the main disadvantage of calcium sensors or VSDs, in the common techniques of optical imaging, is their electrical sensitivity, which can be several orders of magnitude lower than patch-clamp techniques in electrophysiology.
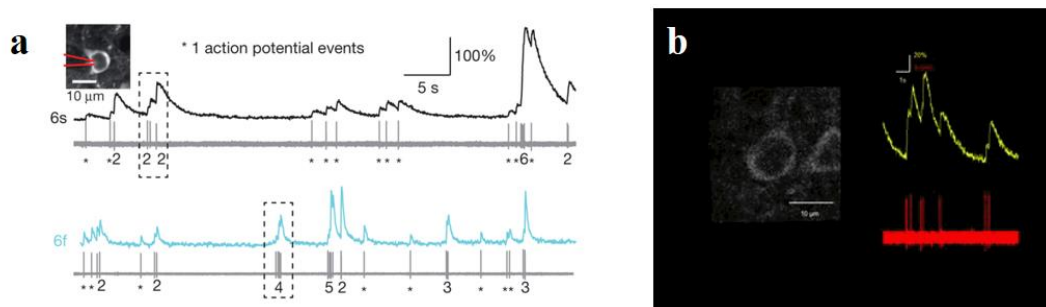
Figure 4.2 (a) Simultaneous fluorescence dynamics and spikes in a GCaMP6s (top) and GCaMP6f (bottom) expressing neuron and (b) a video clip showing simultaneous recording of spikes and GCaMP6s fluorescence signal of a L2/3 neuron in the visual cortex *in vivo*. Images (a)-(b) reprinted with permission from Ref [181]. Copyright © 2013 Nature Publishing Group.

Moreover, microelectrode arrays (MEAs), serving as neural interfaces, stimulate or connect neurons in the electronic circuitry. The electrodes on an MEA can transduce the change in voltage from the environment carried by ions into electronic currents when recording, or electronic currents into ionic currents through the media when stimulating. For example, as shown in Figure 4.3a, MEAs have been used as an effective tool to detect acute neurotoxicity [182]. Recently, high-density microelectrode arrays, such as nanowire transistor arrays, have been applied as smaller and more sensitive devices for neuronal detection [183]. Figure 4.3b gives an illustration of stimulating neuron through nanowires and obtaining the resulting responses. Even though their spatial resolution, temporal resolution, and electrical sensitivity are close to the range needed for electrical stimulation, low throughput in a small sensing area is not suitable for studying individual spines and synapses in a relative large network. Therefore, a different system is required to create a comprehensive high functionality microfluidic device capable of studying synaptic processes both at a single synapse level (submicron) and across a neuronal network (centimeter).
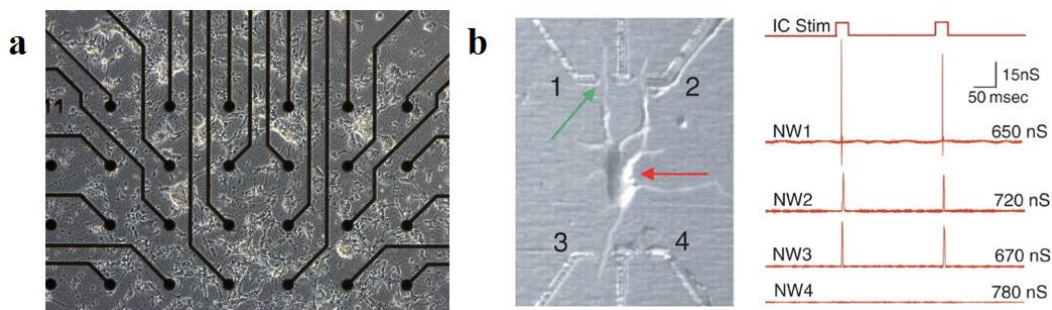
Figure 4.3 (a) Representative neuronal network of primary rat cortical culture on MEA chip. (b) Optical image of a cortex neuron connected to three of the four functional nanowire devices in the array (left) and trace of intracellular current stimulation and resulting nanowire electrical responses (right). Image (a) reprinted with permission from Ref [182]. Copyright © 2010 Elsevier Inc.; image (b) reprinted with permission from Ref [183]. Copyright © 2006 American Association for the Advancement of Science.

4.2 Graphene Biosensors
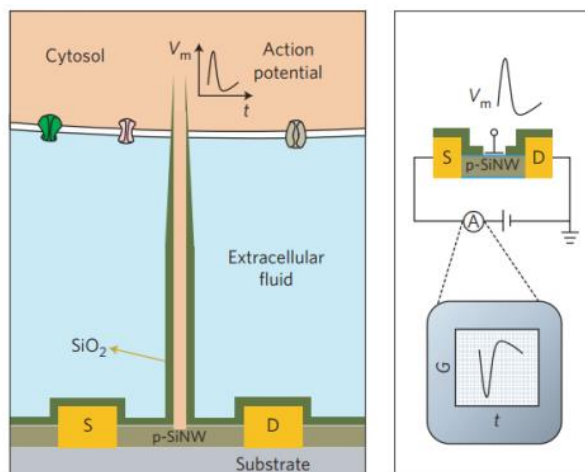
Figure 4.4 Schematic of a cell coupled to a BIT-FET (left) and the variation in device conductance G (right). S and D indicate source and drain electrodes. Image reprinted with permission from Ref [184]. Copyright © 2011 Nature Publishing Group.

FETs have attracted a lot of attention since they can record electrical signals inside

73

the cells. FETs can be made to be smaller than micropipettes and MEAs. Researchers have applied a new approach with a SiO_2 nanotube as a FET to bring contact with the cells, which allows to record the intracellular transmembrane potential [184]. The SiO_2 nanotube can stably record the full-amplitude intracellular action potential when it penetrates the cell membrane to form a tight seal (Figure 4.4). Their studies of cardiomyocyte cells demonstrate that FETs can be applied as a new measurement tool to investigate the cell membrane potentials.

Recently, graphene has gained significant interests from researchers due to its extraordinary electronic and optical properties. One unique advantage of graphene is its exposed volume to the environment, which maximizes the sensitivity to local change. Graphene ribbons with pores in nanometer size have been fabricated to record the ionic activities and detect the DNA translocations simultaneously [185] (Figure 4.5a). Not only is graphene well compatible for nanoscale biomolecules, but also it can be adaptive to detect target analytes in a large scale. Figure 4.5b shows that graphene devices attached with tooth enamel are capable to detect single bacterium [186]. In addition, graphene can adhere to cell membranes or tissue slices to achieve high electrical sensitivity because of its great strength and flexibility [187]. Graphene-based microelectrode arrays have been developed to apply to hippocampal slices, which enables to record high-frequency bursting activity and slow synaptic potentials [188] (Figure 4.5c). Furthermore, monolayer graphene can transmit more than 97% of incident light [189], making it compatible with optical imaging. Figure 4.5d illustrates the optogenetic activation of focal cortical areas under the graphene-based electrodes through a blue light, allowing for *in vivo* imaging of the cortical vasculature via fluorescence microscopy [190]. To summarize, all unique properties of graphene make it an ideal candidate for detecting electrical and electrochemical signals in neuronal research.
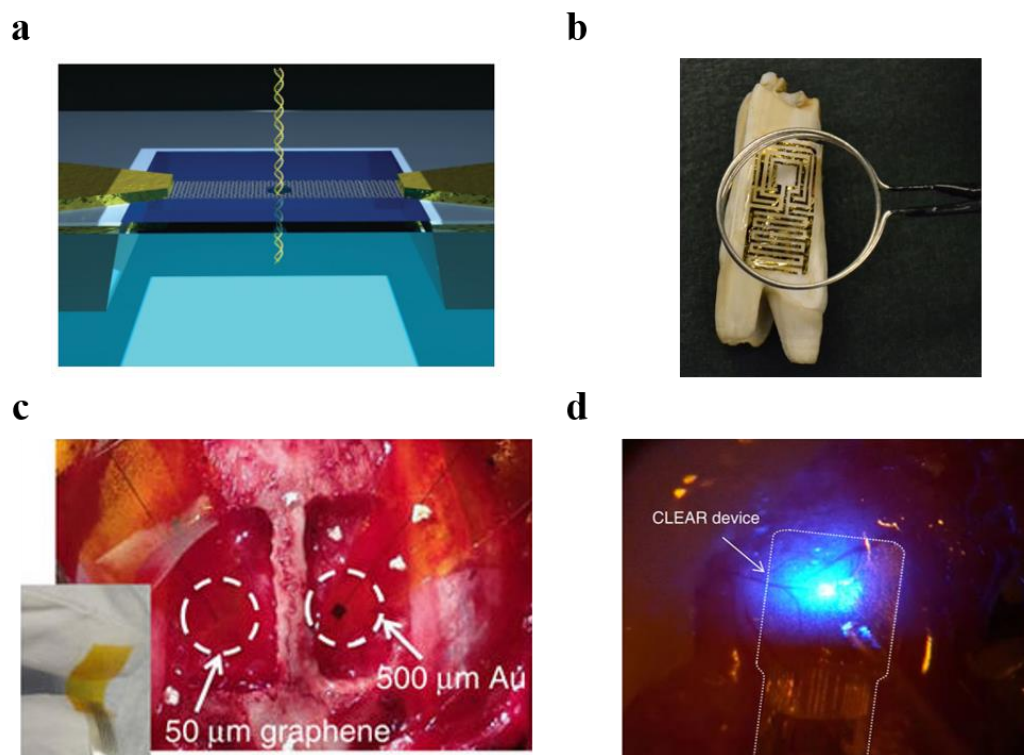
Figure 4.5 (a) Schematic of a nanopore in a graphene nanoribbon, through which a single DNA molecule is translocating. (b) Optical image of the graphene wireless sensor transferred onto the surface of a tooth. (c) Photograph of the single graphene electrode (left) and single Au electrode (right) placed on the cortical surface of hemisphere. The inset illustrates the flexibility of a graphene-based device. (d) Photograph of a blue light stimulus through the graphene-based device on the surface of a mouse brain. Image (a) reprinted with permission from Ref [185]. Copyright © 2013 Nature Publishing Group; image (b) reprinted with permission from Ref [186]. Copyright © 2012 Nature Publishing Group; image (c) reprinted with permission from Ref [188]. Copyright © 2014 Nature Publishing Group; image (d) reprinted with permission from Ref [190]. Copyright © 2014 Nature Publishing Group.

4.3 Experimental Methods

Through directly culturing primary hippocampal neurons on graphene FET arrays and probing the local electrical conductance change at the graphene-synapse junctions via

75

scanning photocurrent microscopy, we demonstrate the capability of mapping the electrical activities of neural networks with single synapse resolution (~ 500 nm, determined by the diffraction-limit of a laser spot). The ultrafast nature of graphene photocurrent response allows decoding a single waveform that may coincide with action potentials from the spontaneous bursts of individual synapses and spines with a temporal resolution at the tens of microsecond level. Importantly, we show that the 2D nature of graphene enables seamless recording of the millivolt extracellular potential changes of the entire neuronal network composed of randomly-distributed synapses/spines.

4.3.1 Device Fabrication and Characterization

Graphene transistors were fabricated on 170 µm-thick transparent coverslips. Electrodes were first defined by photolithography and evaporated with 5 nm Ti and 40 nm Au. High-quality graphene was synthesized via a standard CVD method [113]. Copper foil (Alfa Aesar, 0.025mm, 99.8%) with a grain size of ~ 100 µm was pretreated in a 5% nitric acid bath for 5 min to remove the oxidized coating and then cleaned by deionized water baths. After annealing in the presence of 200 sccm of hydrogen at 1000 °C for 1 h, the hydrogen flow was reduced to 100 sccm and 20 sccm of methane was introduced to the system to complete the graphene growth in 30 min. After that, PMMA layer was spin-coated on top of the copper foil to hold the graphene film. The PMMA-graphene film was separated from the copper foil through a wet etching process in iron chloride solution, and then transferred onto a pre-patterned coverslip. We then performed Raman spectroscopy measurements to inspect the quality and thickness of graphene on the coverslip with a 532 nm laser. As shown in Figure 4.6a, the 2D peak has a symmetric shape and 2D-to-G intensity ratio is about 2, indicating that the as-grown graphene has a monolayer structure [191]. Next,

graphene transistor arrays were sealed in a neuron-glia co-culture microfluidic platform [192] with a large gold pad that acted as an electrolyte-gate to modulate the electrochemical environment of graphene. Gate-dependent conductance measurement of a typical graphene transistor displayed p-type semiconducting characteristics (Figure 4.6d), consistent with previous reports of electrolyte-gated graphene transistors [193].

Spatially resolved scanning photocurrent measurements were performed in an Olympus microscope setup. A continuous-wave laser source ($\lambda = 785$ nm) was expanded and altered by nanometer-resolution scan mirrors. The laser beam was them focused by a 60 X oil-immersion objective (N.A. = 1.4) into a diffraction-limit spot (~ 500 nm) on a graphene transistor (Figure 4.6b). Under 785 nm illumination, electron-hole pairs were generated in graphene and then separated by Schottky-like barriers at graphene-electrode junctions or by a local potential gradient along the graphene (Figure 4.6c). Reflection images were simultaneously recorded by a silicon photodetector, which could be used to precisely locate the position of photocurrent responses.
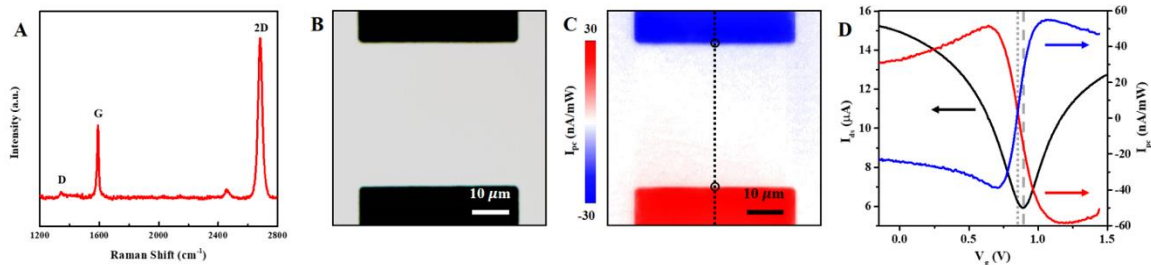
Figure 4.6 (a) Raman spectrum of graphene on a transparent coverslip. (b) Optical and (c) photocurrent images of a typical graphene transistor. (d) Electrical transport behavior (black curve, left) and photocurrent responses (red and blue curves, right) at the black circle regions of the graphene transistor in (c) as a function of V_g. The grey dashed and dotted lines indicate $V_g = V_{Dirac}$ and $V_g = V_{FB}$, respectively.

4.3.2 Cell Loading and Imaging

First, graphene-integrated microfluidic devices were UV sterilized to avoid any source of contamination during the fabrication process. Different chambers were separated for coating by activating the valve barriers with hydraulic pressure after injecting sterilized ddH$_2$O into the pressure chamber. The two inner neuronal chambers were coated with poly-L-lysine (PLL) while the two outer glial chambers were coated with type I collagen in sterile phosphate-buffered saline (PBS).

Second, cell suspension of glia that were isolated from old rat pup brains were loaded into the two outer culture chambers (25,000 cells/chamber). The devices were then incubated at 37°C to allow neurons to adhere to the PLL-coated glass surfaces. After neurons attached, the reservoirs were filled with supplemented neurobasal media. After 24 h, the pressure chamber of each device was deflated by releasing the clamps from the tubes, so the neuronal and the glial chambers were connected. Then, 250 μL of fresh neuron media were added to the glial

reservoirs and 150 µl of the same media were added to the neuronal reservoirs. The unequal volumes in the reservoirs created a passive pressure difference, which generated a steady flow of media from the glial chambers to the adjacent neuronal chambers, providing fresh glia-conditioned media for the neurons. Lastly, fresh neuron media were added to the devices every 24 h, and the collected media were removed from the waste reservoirs at the same time.

Neurons in graphene-integrated microfluidic devices at Days in Vitro (DIV) 8–13 in culture were prepared for live-cell imaging by replacing the neuron media with HBSS. Live-cell imaging was performed on a confocal system with 60X objective. During imaging, cells were maintained at 37°C using a temperature-controlled chamber. mCerulean, GFP and mCherry were excited with 404, 491 and 561 nm laser lines, respectively.

4.4 Results and Discussion

In our studies, we integrated graphene transistor arrays with a microfluidic neuron-glia co-culture platform (Figure 4.7a) that could dynamically image spine and synapse formation through separately transfecting two populations of neurons with pre- and post-synaptic markers [194, 195]. High-quality graphene was synthesized via a standard CVD deposition method [196] and transferred onto 170 µm thick transparent coverslips with pre-patterned gold electrodes [196], forming graphene FETs that were then aligned and bonded with the top microfluidic polydimethylsiloxane (PDMS) structure. Direct transfer of graphene prevents contamination during device fabrication to achieve ultraclean carbon surfaces; and the glass coverslip substrate allows for scanning photocurrent measurements from the lower surface to detect the local photoconductance of graphene (Figure 4.7b) via an oil immersion objective to achieve a diffraction limit of ~ 500 nm [197]. We used Raman spectroscopy to inspect the quality and thickness of graphene on a coverslip with a 532 nm laser. As shown in Figure 4.6a, the 2D peak has a symmetric shape and the 2D-to-G intensity

ratio is about 2, indicating that the as-grown graphene has a monolayer structure [191]. Next, we tested the electrical response of the graphene transistors in our microfluidic chambers by including a large gold pad that acted as an electrolyte gate to modulate the electrochemical environment of graphene. Gate-dependent conductance measurement of a typical graphene transistor displayed p-type semiconducting characteristics (Figure 4.6d), consistent with previous reports of electrolyte-gated graphene transistors [193].

To probe electrical activities of neuronal processes with these graphene FETs, we co-cultured primary embryonic hippocampal neurons with glia to maintain healthy cultures that make direct contact with graphene transistors. In our microfluidic platforms, the graphene transistors were positioned underneath a middle channel that was between two inner chambers with neurons (Figure 4.7a and Figure 4.7c). The neurons in these two chambers were separately transfected with plasmid constructs expressing either mCherry-synaptophysin (red, Figure 4.7d), a pre-synaptic marker, or mCerulean (blue, Figure 4.7e), which marks dendritic spines containing post-synaptic densities. Glia were loaded into the two outer chambers to support the growth and differentiation of the hippocampal neurons. The mid-channel and cell chambers are separated by PDMS valve barriers with microgrooves underneath them, which can be controlled to be either closed or open by the hydraulic pressure in a control chamber constructed on top of the cell culture layer. In the closed position, the valve barriers completely isolated the chambers for separate culture or treatment of each cell population [192]. When the valve barriers were in the open position, the microgrooves connected the chambers, allowing for interactions and communication between cells in different chambers. After 8 to 12 days in culture, neuronal processes extended toward the adjacent chambers and contacted each other in the mid-channel. We then used fluorescence microscopy to visualize synaptic contacts between mCherry-

synaptophysin (red) and mCerulean (blue) (Figure 4.7f-h).
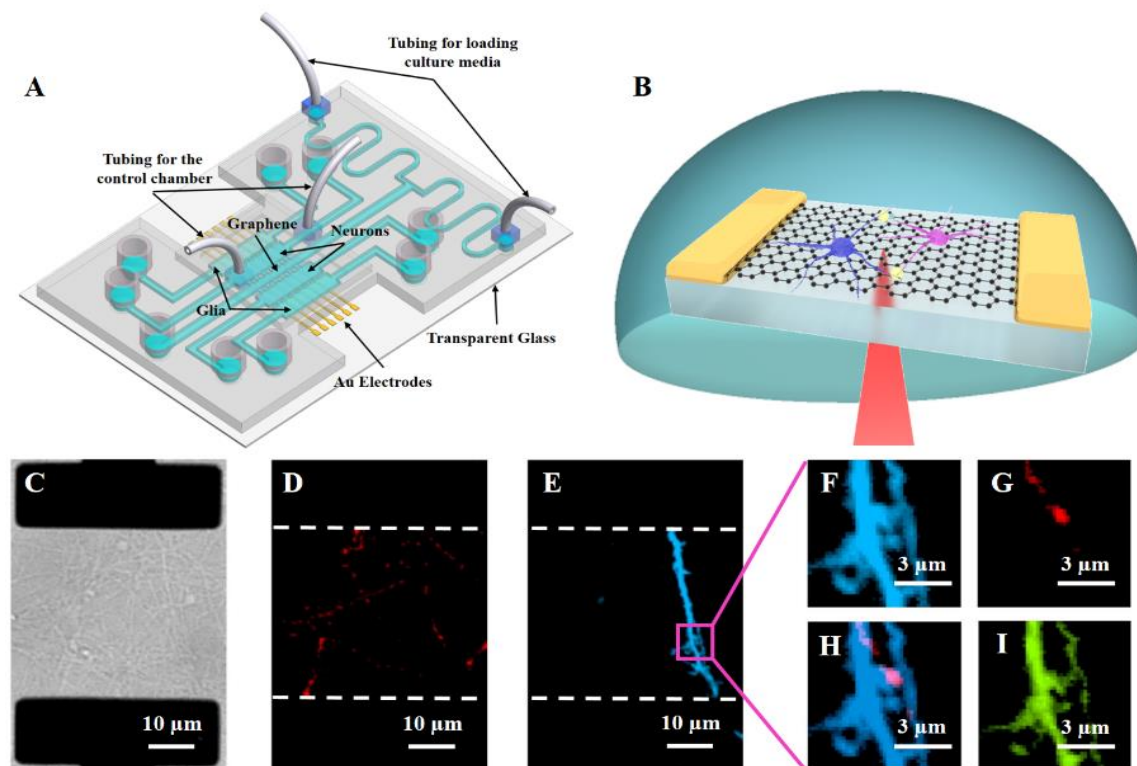
Figure 4.7 (a) Schematic of a four-chamber neuron-glia co-culture microfluidic device with integrated graphene transistors. (b) Schematic of scanning photocurrent measurements. A diffraction-limited laser spot passes through a transparent coverslip to scan over the graphene underneath neurons. (c) Differential interference contrast (DIC) of a graphene transistor underneath neural network. The two black rectangles are opaque Au electrodes that are underneath the graphene membrane. Neurons, at day 5 in culture, were differentially transfected with (d) mCherry-synaptophysin (red) and (e) mCerulean (blue), maintained in co-culture with glia. Zoom-in fluorescence images of a magenta square region in (e): (f) mCerulean (blue); (g) mCherry-synaptophysin (red); (h) overlay of mCerulean and mCherry-synaptophysin; and (h) GFP-GCaMP6s (green).

In addition, GFP-GCaMP6s (a fluorescence Ca^{2+} indicator, green, Figure 4.7i) was also used to characterize synaptic activities. Figure 4.8a presents a phase image of one neuron body cultured in the dish. When the media is switched from 4 mM K^+ to 90 mM K^+,

the fluorescence intensity of neuronal processes marked by red arrows increases at least 40% (Figure 4.8b and Figure 4.8c).
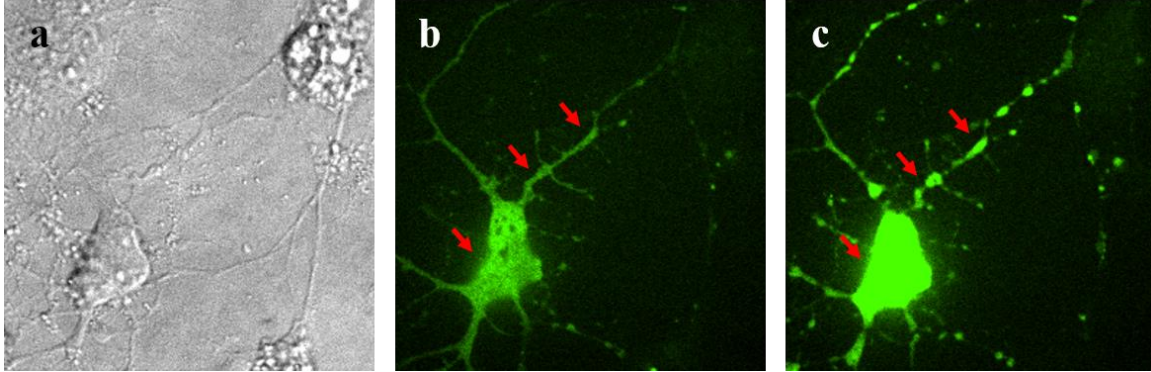
Figure 4.8 (a) Phase image of neurons in the dish. The corresponding fluorescence images in (b) 4 mM K^+ buffer and (c) 90 μ K^+ buffer. Dr. Mingjian Shi credits.

After locating individual spines and synapses using optical and fluorescence microscopy (Figure 4.9a-d), we measured the photocurrent response of the graphene transistor underneath these spines and synapses. Here the neuronal activity-initiated action potentials along their axons that could change local electrochemical environments, influencing the local charge carrier concentration of graphene and thus modifying its local energy band diagram (Figure 4.9f). When a diffraction-limited laser spot ($\lambda = 785$ nm) scanned over a graphene transistor through a piezo-controlled mirror with nanometer-scale spatial resolution, a photocurrent signal occurred wherever the graphene energy band bended; the built-in electric field separated photo-excited electron and hole pairs (EHPs), and thus produced an electrical current [198]. We extracted band diagrams ($E_F - E_{Dirac}$) through numerical integration of photocurrent profiles [198, 199]. The electron energy of graphene follows a linear dispersion near the Dirac point, with a Fermi energy of $E_F - E_{Dirac} \approx \hbar v_F \sqrt{\pi n}$, where $v_F \approx 10^6\, m/s$ is the Fermi velocity and n is the charge carrier

concentration [200]. We then calculated the local charge ($Q = ne$) of graphene from photocurrent data and derived a local potential ($V = Q/C$), where C is a combination of the electrostatic capacitance between the graphene and a synapse/spine and the quantum capacitance of the graphene. The minimum quantum capacitance $C_{Q,min}$ is about 6.5 $\mu F/cm^2$ [201] and the double layer capacitance of the electrolyte C_i is approximately 20 $\mu F/cm^2$ [201]. Thus, the total capacitance C is ~ 4.9 $\mu F/cm^2$. If we simply use the graphene transistor without the scanning photocurrent scheme as our sensing approach, then we face a major challenge that the local ion concentration change needs to provide enough charge to affect the conductance of the entire graphene membrane between the source and drain electrodes. In contrast, introducing scanning photocurrent microscopy allows for probing of the local conductance of a small area of graphene piece, which corresponds to a region of the diffraction-limited laser spot of about 0.5 μm in diameter. For such a small piece of graphene as an optoelectronic probe, the maximum corresponding capacitance is ~ 10 fF, leading to ultrahigh electrical sensitivity.
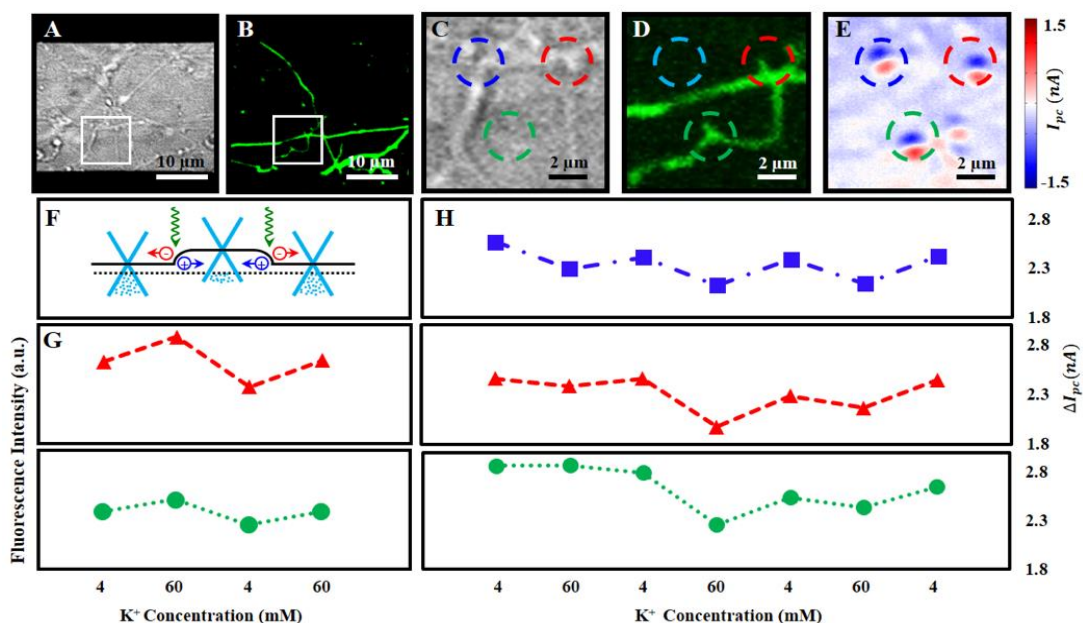
Figure 4.9 (a) DIC and (b) fluorescence (GFP-GCaMP6s, green) images of neurons, at day 8 in culture, on top of a graphene transistor. Zoom-in (c) DIC and (d) fluorescence images of the white square regions in (a) and (b). Three synapses/spines are marked by blue, red, and green circles, respectively. (f) Schematic of band structures of graphene. The black dotted line denotes the Fermi level and the solid line shows the graphene band diagram. A local electrochemical potential change induced by a synapse/spine results in the local carrier concentration changes of graphene, leading to the graphene energy band bending and subsequent photocurrent generation. (g) Fluorescence intensity changes when the neurons were exposed to 4 mM K^+, 60 mM K^+, 4 mM K^+, and 60 mM K^+, respectively. Red triangles and green spheres represent the fluorescence intensities of synapses/spines at spots of the corresponding color in (e). (h) Photocurrent responses of three graphene-synapse junctions upon three high-K^+ stimulation cycles (4-60-4-60-4-60-4). Blue squares, red triangles, and green spheres represent the photocurrent responses of graphene-synapse junctions at spots with the corresponding color in (f). $\varDelta I_{pc}$ is the difference between the maximum (red) and minimum (blue) photocurrent response.

Our results show remarkable photocurrent signals generated at spots where spines

and synapses were located (Figure 4.9e), indicating that our approach can be used to detect electrical activities of individual synapses and spines with submicron spatial resolution. We then compared our photocurrent scheme with traditional fluorescence-based imaging approaches. The local potential of neuronal membranes increased upon high-K^+ stimulation, which led to changes in both the fluorescence intensity of GFP-GCaMP6s (Figure 4.9g) and in the photocurrent response of graphene-synapse junctions (Figure 4.9h) as we switched between high-K^+ and low-K^+ media in the chamber (the total ionic concentration was kept as a constant), underscoring the validity of our approach. Interestingly, even though the photocurrent measurements follow the same general trend, the electrical responses of individual synapses vary from synapse-to-synapse during depolarization (Figure 4.9h), which is interesting and will be further explored. Note that after two depolarization cycles the fluorescence signal was photobleached, but the electrical response of individual spines and synapses could still be detected by photocurrent measurements. Importantly, we could derive the local extracellular membrane potential changes (~ 2 mV) during the depolarization from our photocurrent measurements. More details are explained in the appendix.
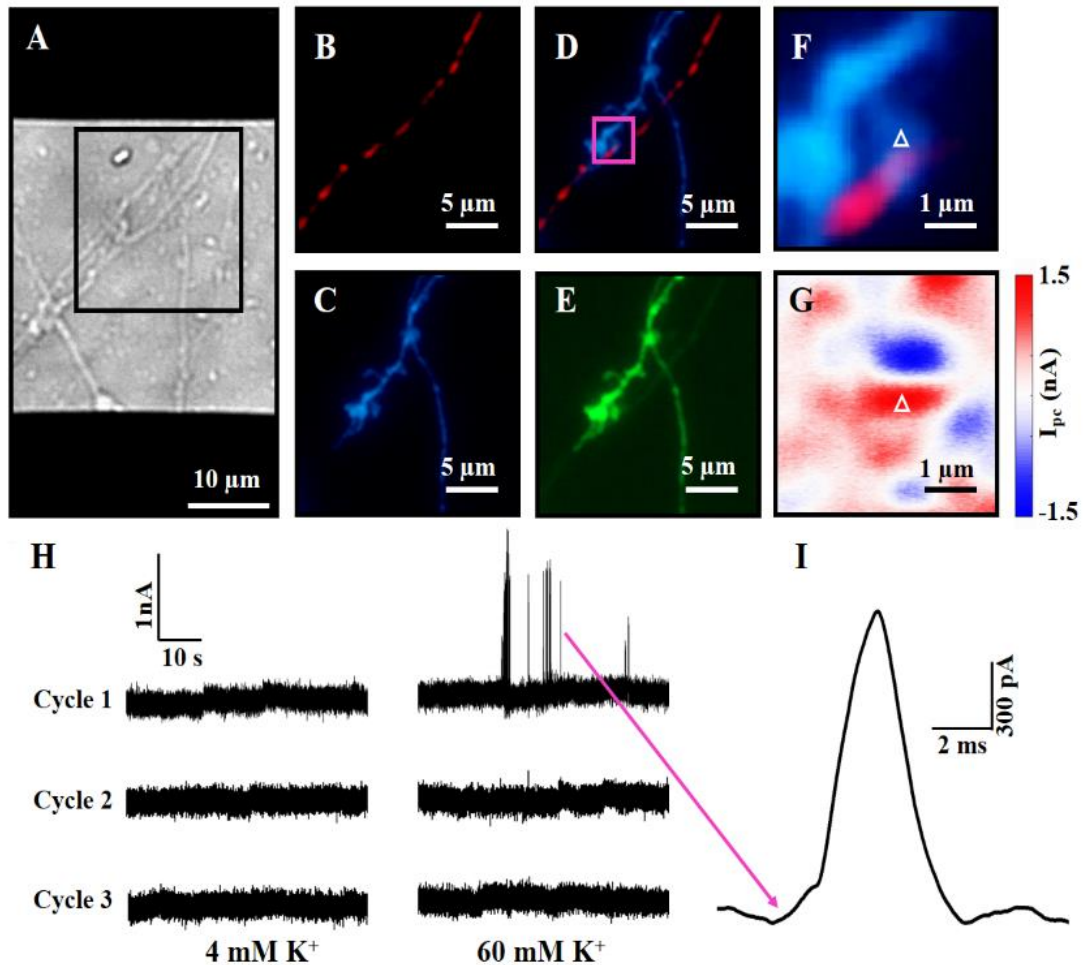
Figure 4.10 (a) DIC image of neurons, at day 9 in culture, atop a graphene transistor. Zoom-in fluorescence images of the black square region in (a): (b) mCherry-synaptophysin (red); (c) mCerulean (blue); (d) overlay of mCerulean and mCherry-synaptophysin; and (e) GFP-GCaMP6s (green). Detailed fluorescence (f) and photocurrent (g) images of the magenta square region in (d). (h) Photocurrent responses of a graphene-synapse junction (white triangles in (f) and (g)) upon three high-K^+ stimulation cycles (4-60-4-60-4-60). (i) Spontaneous waveform of a spike burst indicated by a magenta arrow in (h).

To examine the temporal resolution of graphene optoelectronic probes, we studied

spontaneous bursts by raising the extracellular K^+ concentration from 4 mM to 60 mM. In our experiments, DIC and fluorescence images were used to identify a synaptic contact (Figure 4.10a-f), and the laser beam was then focused on the corresponding graphene-synapse junction to collect the photocurrent responses every 50 µs to record the local electrical activity at the junction. As shown in Figure 4.10h, bursts occurred when the extracellular K^+ concentration increased to 60 mM; and these bursts disappeared when the extracellular K^+ concentration was reduced to 4 mM. We also found that no burst was observed in the second and third cycles, which could be due to the cytotoxic effect of high-K^+ concentration [202-205]. The high electrical sensitivity and temporal resolution of graphene optoelectronic probes also allowed us to decode the detailed spontaneous waveform of each burst. As shown in Figure 4.10i, the burst has a waveform with a width about 2-3 ms, whose shape is similar to an action potential with a maximum extracellular potential change of ~ 14 mV. More details are explained in the appendix.

Interestingly, synapses responded differently in the high-K^+ concentration media. For example, spontaneous bursts of another graphene-synapse junction, which was identified by DIC and photocurrent images (Figure 4.11a and Figure 4.11b), were observed at regular intervals with a frequency of 0.2 Hz (Figure 4.11c). After the extracellular K^+ concentration was reduced to 4 mM, the spontaneous bursts disappeared. We also found that the burst intensity and frequency decreased in the second 90 mM cycle, while no burst was observed in the third and fourth cycles. Close examination of the bursts reveals that each burst includes a series of peaks with widths of 2-10 ms, which is likely related to action potentials or postsynaptic responses.
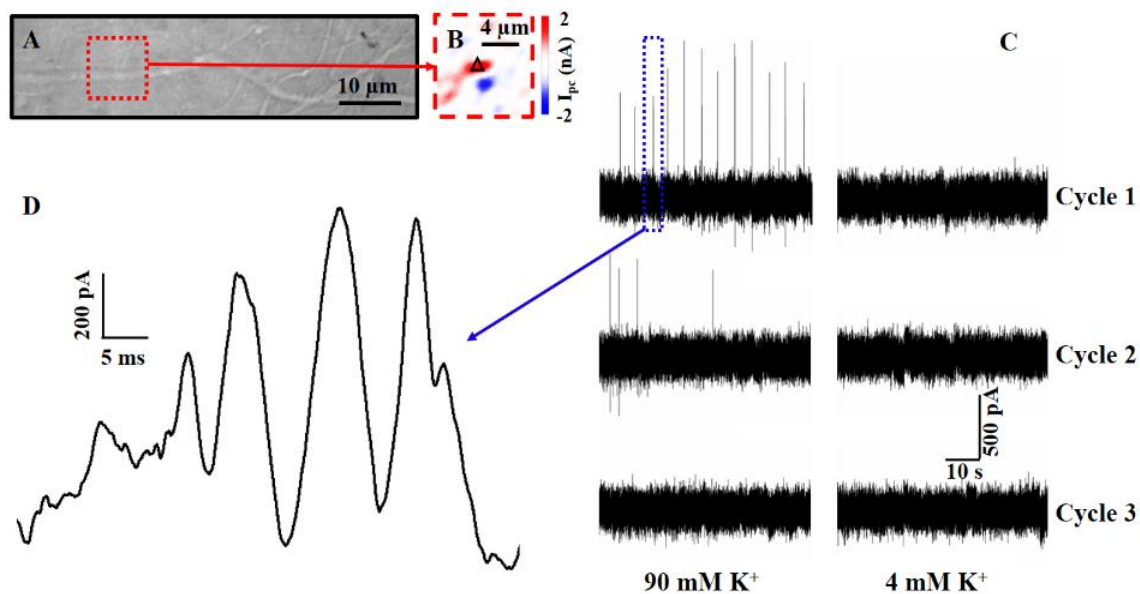
Figure 4.11 (a) DIC and (b) zoom-in photocurrent images of neurites, at day 8 in culture, on top of a graphene transistor. (c) Photocurrent responses of a graphene-synapse junction (a black triangle in (b)) upon three high-K$^+$ stimulation cycles (90-4-90-4-90-4). (d) Spontaneous waveform of a spike burst indicated by a blue dotted rectangular in (c).

In conclusion, by combining graphene transistor arrays with scanning photocurrent microscopy, we created a unique approach that can map electrical activities of neural networks with sub-micron spatial and tens of microsecond temporal resolution, high electrical sensitivity, and high throughput. We demonstrated the power of this sensing scheme by probing the electrical responses of individual spines and synapses in primary embryonic hippocampal neuron cultures at rest and during depolarization. Importantly, we were able to decode detailed waveforms of the spontaneous bursts of individual synapses during depolarization. Furthermore, the 2D nature of graphene allows continuous mapping of multiple randomly-distributed synapses and spines. As such, this new neurotechnology provides the capability of large-area mapping with a high spatiotemporal resolution to

explore neural networks with detailed information of activities and signal events at a single-synapse level. New knowledge gleaned using this powerful approach will undoubtedly lead to in-depth understanding of cognitive behavior and be instrumental in the development of new therapeutic approaches for treating neuronal and psychiatric disorders. Finally, this technology should also be able to probe many other cellular systems involving cell-cell interactions through electrical signaling.

CHAPTER 5

SUMMARY AND FUTURE WORK

5.1 Summary

In the past decades, a large variety of emerging technology has evolved greatly to explore the nanomaterial field, from carbon-based materials to TMDC family, from Scotch tape method to large-scale production and from single crystal to integrated hybrids. Owning to many fascinating properties of nanomaterials, a broad set of applications has been developed to create a huge amount of economic and industrial value, paving the way for future advances in electronics and optoelectronics.

In this dissertation, three appealing nanomaterials, CNT, graphene and MoS_2, have been thoroughly summarized in the aspects of structures, growth mechanisms, electronic/optoelectronic properties, extended applications. Combining these materials through multiple-cycle processes in a controlled fashion can create hybridized structures with enhanced properties that provide new ideas to design and fabricate novel materials and devices. In CHAPTER 2, we describe the synthesis of high-quality and uniform nanomaterials with advanced transfer techniques. Due to the outstanding mechanical properties of CNTs, we incorporated randomly-distributed CNT network into the graphene growth and produce novel hybrids without the assistant of polymer at transfer. This ultra-thin CNT-graphene films not only has enhanced mechanical strength (Figure 2.6c), but also high optical transmission and good electrical conductivity. At the junctions between two materials, interesting optoelectronic properties were investigated through scanning photocurrent microscopy, which might contribute to the unzipped nanoribbons stacking on top of graphene.

The linkage between two nanomaterials leading to novel and enhanced properties, inspires us to combine p-type SWNT arrays and n-type MoS_2 films. In CHAPTER 3, we studied the synthesis of SWNTs and the applicable potential of aligned SWNT transistors. Later, the synthesis and characterization of monolayer MoS_2 have been discussed, indicating the possibility of producing SWNT-MoS_2 hybrid by a multi-cycle process. This novel hybrid can be simply visualized under a microscope (Figure 3.16a) and shows enhanced Raman intensity at junctions (Figure 3.16c-e). Furthermore, the range of photoresponse can be broadened to NIR spectral region. The work presented in CHAPTER 2 and CHAPTER 3 provides new ways to the development of hybridized structures toward future optoelectronic applications.

We have introduced a lot of exciting breakthroughs in the applications of CNT, graphene and MoS_2 owing to their outstanding properties. In CHAPTER 4, the flexibility and compatibility of graphene integrated with scanning photocurrent microscopy, allows us to study the electrical and electrochemical signals of neuron synapses. This new technology covers three domains of knowledge: (a) graphene transistors and related optoelectronic measurements in the nanomaterial field; (b) design of microfluidic platform in the field of mechanical engineering; (c) culture and fluorescence of neurons in the biological field. We can electrically detect the neuronal activities with sub-micron spatial and tens of microsecond temporal resolution, high sensitivity and high throughput. The detailed waveform of signals for neurons at rest and during depolarization, can be decoded in real time and consistent with imaging microscopy by flowing different concentrations of K^+ in our microfluidic systems (Figure 4.10 and Figure 4.11). Our achievement of applying innovative nanomaterials call attention to current neuronal studies.

5.2 Future Work

We have made significant progress in the development of hybridized materials through CVD. However, abundant exciting opportunities are still available to further advance the capabilities and applications of the hybrids. The following paragraphs outline the potential directions of our current work.

In CHAPTER 2, we apply the randomly-distributed CNT networks to enhance the mechanical properties of graphene films. Instead, SWNT arrays or networks in certain oriented directions may be used as back bones to support graphene films. With the introduction of aligned nanotubes, it is advantageous to explore the junction area between graphene and nanotubes (or nanoribbons) using TEM and scanning photocurrent microscopy. However, the density of SWNT arrays and the influence of polymer contamination at transfer can pose challenges for this extended research. For SWNT-MoS_2 hybrids in CHAPTER 3, a controlled growth can be potentially performed to study the role of SWNTs as seeds in the MoS_2 growth process. The junction area between SWNT and MoS_2 films can also be characterized. Furthermore, the broadened properties in electronics and optoelectronics can provide new avenues for other hybridized structures such as SWNT integrated with WS_2/$MoSe_2$/WSe_2 films.

Finally, for graphene optoelectronic probes in CHAPTER 4, a significant amount of potential work can have notably impact on biosensing technology. For example, graphene can be patterned or replaced with other nanomaterials such as aligned SWNTs (Figure 3.9) to explore the neuronal activities. Additionally, the graphene probes can be adapted to studies activities of other cell types, such as tracking the migration of cancer cells in the sensing region or studying the electrical signals of mouse retina [206]. Furthermore, the in-depth understanding of identifying the patterns of signaling for activities of neurons can be

potentially explored by contemporary computational techniques such as Bayesian modeling or machine learning.

In conclusion, the current studies of nanomaterials have created many novel properties and practical applications even though many challenges still exist. Hopefully, the work presented in this dissertation will bring attention to future development of nanomaterials and nanotechnology.

APPENDIX

A.1 Recipe of 2D Graphene Growth

1. Check all the gauges of gases and report if the inner pressures are below 500 psi.

2. Prepare 5% Nitric Acid solution. The volume ratio of deionized water to nitric acid (70% concentration) is 13:1.

3. Treat the foil with 5% Nitric Acid solution for 3 ~ 5 minutes and deionized water bath three times each for 3 min. Dry the sample by nitrogen gun gently.

4. Slowly open the speed valve to pump down the system. Then turn on the pressure monitors in a small scale. Purge gas lines by flowing the Ar into the system.

5. Record the base pressure and humidity. Start to flow 200 sccm Ar for 5 minutes and then switch to 200 sccm H_2 flow. Set the temperature at 930 ^{o}C for one-hour annealing.

6. Change H_2 flow to 100 sccm when the annealing process is finished and add 20 sccm CH_4 to start the growth for 30 minutes. Start to flow 200 sccm Ar and move quartz boat out of the hot zone by magnetic stir bar.

7. Turn off the furnace and stop flowing CH_4 and H_2. Note that the 1:5 ratio of CH_4 to H_2 is optimized.

8. Insert the steel disk into the furnace gap in the cooling process. When temperature drops to 200 ^{o}C, slowly close the speed valve and turn off the pump.

9. Spin coat A2 PMMA for 4500 rpm for 45s and etch the sample by $FeCl_3$ overnight.

10. Transfer the sample into deionized water bath at least 3 times. Then transfer it to the desired substrate. Clean PMMA by acetone, IPA, deionized water, orderly.

A.2 Recipe of 3D Graphene Growth

1. Cut the nickel foam into the right size and place it into the quartz boat.

2. Follow the same procedures as 2D graphene growth except of acid pretreatment. Set up the growth temperature at 1000 °C and flow 500 sccm Ar and 200 sccm H_2 in the annealing process for 20 minutes.

3. Add 10 sccm CH_4 for 20 minutes growth. Turn off the gas and furnace and take the sample out.

4. Drop A2 PMMA on the foam sample and bake it at 170 °C for 2 minutes. And etch the sample by $FeCl_3$ for overnight.

5. Transfer the sample into deionized water bath at least 3 times. Clean PMMA by soaking the sample into acetone, IPA, deionized water, orderly. The acetone cleaning involves a heat process at 80 °C for 2 hours to remove PMMA. Figure A.1 shows a SEM image of a 3D structure of graphene foam after etching.
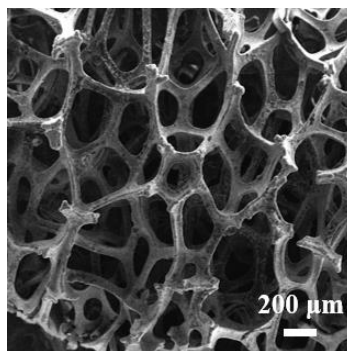
Figure A.1 SEM image of 3D graphene.

A.3 Recipe of Aligned SWNT Growth

1. Clean the quartz substrate by repetitively applying Scotch tapes. Use a diamond pen and cut a straight line as a marker. The spacing should be less than 1mm.

2. Spin the catalyst solution at 1000 rpm for 30 minutes before you start to glue the solution. The catalyst solution consists 15 mL ethanol, 60 mg PVP and 1.9 mg $CuCl_2$.

3. Glue the solution onto the tape at least 5 times.

4. Place the samples into the quartz boat and annealing them in the air at 685 °C for 30 minutes. After that, cool the samples down to room temperature.

5. Set up the furnace to ensure the ethanol flow into the system. Anneal the sample at 685 °C with the flow of 200 sccm H_2 for 30 minutes. Then raise the furnace temperature up to 815 °C.

6. When the furnace temperature is stabilized at 815 °C, add a flow of 50 sccm Ar through an ethanol bubbler into the furnace to complete the growth process for 30 minutes.

7. Add 200 sccm Ar from another channel and turn off the flow of 200 sccm H_2 and 50 sccm Ar. Turn off the furnace and take the samples out of the furnace until the temperature is under 250 °C.

8. Spin coat A2 PMMA for 4500 rpm for 45s. Etch the sample from quartz surface by a hot KOH solution at 70 °C for 3 minutes. Scratch the edge by a sharp tweezer will help speed the peel-off process and obtain a complete and flat film.

9. Transfer the sample into deionized water bath at least 3 times. Then transfer it to the desired substrate. Clean PMMA by acetone, IPA, deionized water, orderly. The acetone cleaning involves a heat process at 80 °C for 1 hour to remove PMMA.

A.4 Recipe of Monolayer MoS₂ Growth

1. Clean the quartz or SiO_2/Si substrate by a mixed piranha solution (30 mL H_2SO_4 and 10 mL H_2O_2).

2. Place ~ 300 mg MoO_3 and ~ 10 mg Sulfur into each boat and put the desired substrate face down to the MoO_3 powder.

3. The distance between Sulfur boat and MoO_3 ranges from 18-21 cm.

4. Flow 500 sccm Ar to purge the system for 20 minutes. Change the Ar flow to 10 sccm and ramp the furnace temperature to 650 °C by 20 minutes.

5. The growth process consists two parts. The first part is to let the furnace temperature stabilize for 5 minutes. The second part is to allow the furnace naturally cool to 450 °C, in which it usually takes ~ 10 minutes.

6. Open the furnace once the two parts are completed and purge the system by flowing 500 sccm Ar.

7. Turn off the furnace and take the samples out of the furnace until the temperature is under 100 °C.

8. Spin coat A2 PMMA for 4500 rpm for 45s. Etch the sample from the substrate surface by a hot KOH solution at 70 °C for 3 minutes. Scratch the edge by a sharp tweezer will help speed the peel-off process and obtain a complete and flat film.

9. Transfer the sample into deionized water bath at least 3 times. Then transfer it to the desired substrate. Clean PMMA by acetone, IPA, deionized water, orderly. The acetone cleaning involves a heat process at 80 °C for 1 hour to remove PMMA.

A.5 Transistor Fabrication

1. Design the pattern using L-editor or CAD software and obtain the mask after the Cr etching.

2. Prepare the coverslips or SiO_2/Si substrates and clean the surface with nitrogen flow.

3. Spin coat MCC primer20 (20% HMDS and 80% PM Acetate) at 4000 rpm for 45 seconds and spin coat JSR NFR016D2-55cp at 4000 rpm for 45 seconds.

4. Pre-bake the sample at 95 °C for 1.5 minutes and take the sample under exposure for 4 ~ 6.5 seconds.

5. Post-bake the sample at 115 °C for 1.5 minutes and soak it into developer (CD-26) for 1 minute. Then de-scum the sample through plasma for 1 minute.

6. Perform e-beam evaporation of 5 nm Ti/Cr and 40 nm Au.

7. Soak the device into an Acetone bath to complete the lift-off process for 10 minutes. Sonication can be used if needed. Clean the transistors with the following process applying IPA and water.

A.6 Nanotube Imaging with Sulfur Molecules

1. Synthesize horizontally-aligned SWNTs on ST-cut quartz substrates.

2. Perform the etching recipe as discussed in the recipe of aligned SWNT growth.

3. Transfer PMMA/SWNTs film onto water. Use a tweezer to scratch the edges if the film sticks to the quartz surface. At least two DI water baths are preferred.

4. Prepare PDMS substrate and treat it in O_2 plasma chamber for 10 seconds. Transfer the sample onto PDMS substrate and leave it dry at least 2 hours.

5. Clean PMMA by shooting Acetone/IPA for 1 minute each and dry the sample naturally.

6. Preheat the sulfur on a hot plate at 130 °C for 10 minutes. Treat SWNTs/PDMS in O_2 plasma chamber for 10s and place the sample on top of a sulfur container. This coating process can be taken for 3 ~ 10 minutes.

7. Observe the sample under optical microscope. Keep coating the sulfur if needed. Below is a microscope image of coating sulfur molecules to visualize SWNTs.
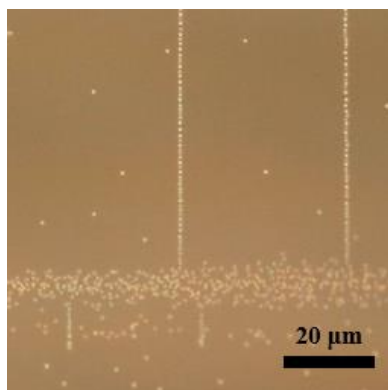
Figure A.2 Optical image of SWNTs with sulfur molecules.

A.7 Calculation of Local Potential Changes via Scanning Photocurrent Measurements[1]

Since photocurrent signals are proportional to the local potential gradients, we can extract band diagrams ($E_F - E_{Dirac}$) of graphene through numerical integration of photocurrent profiles[198, 199]. Based on a simple capacitor model, we obtained an expression for the energetic difference $\Delta E = E_F - E_{Dirac} \approx \hbar v_F \sqrt{\pi n} = \hbar v_F \sqrt{\pi \frac{C}{e} |V_g - V_{Dirac}|}$, where $v_F \approx 10^6 \, m/s$ is the Fermi velocity, n is the charge carrier concentration, and C is the combination of the electrostatic capacitance between a graphene and a synapse/spine and the quantum capacitance of the graphene[200]. The minimum quantum capacitance $C_{Q,min}$ is about $6.5 \, \mu F/cm^2$ [201], and the double layer capacitance of the electrolyte C_i is approximately $20 \, \mu F/cm^2$ [207]. Thus, the total capacitance C is $\sim 4.9 \, \mu F/cm^2$.

As shown in Figure 4.6d, the minimum conductance for a typical graphene transistor is observed to be $V_{Dirac} \sim 0.893 \, V$, leading to $\Delta E(V_g = V_g^{Global} = 0) \approx 0.4864 \, eV$. Moreover, almost no photocurrent is observed for the flat band condition at $V_{FB} \sim 0.850 \, V$. This allows us to estimate the constant energetic offset at the graphene-electrode contacts: $\phi_{FB} = \Delta E(V_g = V_{FB}) \approx 0.1067 \, eV$.

On the other hand, we can extract the band diagrams by numerical integration from the photocurrent profiles across the drain and source electrodes (Figure A.3a and Figure A.3b). The integrated difference across the drain and source is $\Delta \phi_{PC}^{Global} \approx 2.4880$, corresponding to the energetic difference $\Delta E(V_g = V_g^{Global} = 0) \approx 0.4864 \, eV$. Based on

---

[1] Yuchen Zhang credits.

this relationship, we can calculate the local energetic difference induced by neurons. Figure A.3d and Figure A.3f show the photocurrent measurements of a typical graphene-synapse junction (blue circle in Figure 4.9) at rest (4 mM K$^+$) and during depolarization (60 mM K$^+$), respectively. As illustrated in Figure A.3f and Figure A.3g, the local integrated difference of the graphene-synapse at rest (during depolarization) is $\Delta\phi_{PC}^{4\ mM} \approx 0.0460$ ($\Delta\phi_{PC}^{60\ mM} \approx$ 0.0430), corresponding to an energetic difference of $\Delta E^{4\ mM} \approx 0.4954\ eV$ ($\Delta E^{60\ mM} \approx$ 0.4948 eV). We then calculate the local carrier concentration $n = \left(\frac{\Delta E}{\hbar v_F}\right)^2 / \pi$ and derive a local carrier concentration change of $\sim 6.7 \times 10^{10}\ cm^{-2}$, corresponding to a local potential change of $\sim 2\ mV$.
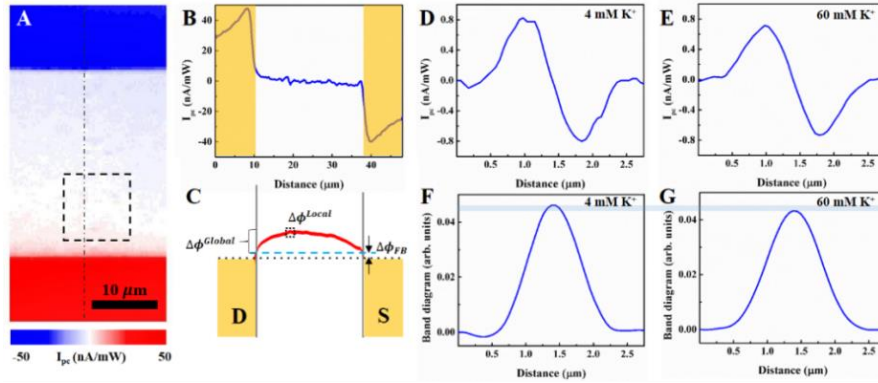
Figure A.3 (a) Photocurrent image of a graphene transistor underneath neurons. The dotted square region is the same region illustrated in Figure 4.9e. (b) Photocurrent profile and (c) integrated difference along the dashed line in (a). The yellow shaded regions indicate Au electrodes. Photocurrent profiles and integrated difference in 4 mM K$^+$ (d, f) and 60 mM K$^+$ media (e, g) of a graphene-synapse junction circled by a black line in (c) and a blue line in Figure 4.9e.

Similarly, we can estimate the local potential change from the temporal photocurrent

measurements, where we assume the integrated difference is proportional to the photocurrent intensity, which is illustrated in our spatial photocurrent measurements. The burst peaks in Figure 4.10i and Figure 4.11d correspond to local potential changes of 14 mV and 11 mV, respectively.

REFERENCES

1.   Hubler, A.W. and O. Osuagwu, *Digital Quantum Batteries: Energy and Information Storage in Nanovacuum Tube Arrays.* Complexity, 2010. **15**(5): p. 48-55.

2.   *Carbon Nanotube.* 2018 [cited 2018 30 April]; Available from: https://en.wikipedia.org/wiki/Carbon_nanotube.

3.   Ficek, R., et al., *Carbon nanotubes synthesized by plasma enhanced CVD: Preparation for measurements of their electrical properties for application in pressure sensor.* 2006 International Symposium on Communications and Information Technologies,Vols 1-3, 2006: p. 42-+.

4.   Jones, D.E.H., *Science of fullerenes and carbon nanotubes - Dresselhaus,MS, Dresselhaus,G, Eklund,PC.* Nature, 1996. **381**(6581): p. 384-384.

5.   Wildoer, J.W.G., et al., *Electronic structure of atomically resolved carbon nanotubes.* Nature, 1998. **391**(6662): p. 59-62.

6.   Saifuddin, N., A.Z. Raziah, and A.R. Junizah, *Carbon Nanotubes: A Review on Structure and Their Interaction with Proteins.* Journal of Chemistry, 2013.

7.   Hammel, E., et al., *Carbon nanofibers for composite applications.* Carbon, 2004. **42**(5-6): p. 1153-1158.

8.   Kumar, M., *Carbon Nanotube Synthesis and Growth Mechanism.* Carbon Nanotubes - Synthesis, Characterization, Applications, 2011: p. 147-170.

9.   Journet, C., et al., *Large-scale production of single-walled carbon nanotubes by the electric-arc technique.* Nature, 1997. **388**(6644): p. 756-758.

10.   Ebbesen, T.W. and P.M. Ajayan, *Large-Scale Synthesis of Carbon Nanotubes.* Nature, 1992. **358**(6383): p. 220-222.

11.   Thess, A., et al., *Crystalline ropes of metallic carbon nanotubes.* Science, 1996. **273**(5274): p. 483-487.

12.   Ding, L., et al., *Selective Growth of Well-Aligned Semiconducting Single-Walled Carbon Nanotubes.* Nano Letters, 2009. **9**(2): p. 800-805.

13.   Su, M., B. Zheng, and J. Liu, *A scalable CVD method for the synthesis of single-walled carbon nanotubes with high catalyst productivity.* Chemical Physics Letters, 2000. **322**(5): p. 321-326.

14.   Bower, C., et al., *Nucleation and growth of carbon nanotubes by microwave plasma chemical vapor deposition.* Applied Physics Letters, 2000. **77**(17): p. 2767-2769.

15.   Fan, S.S., et al., *Self-oriented regular arrays of carbon nanotubes and their field emission properties.* Science, 1999. **283**(5401): p. 512-514.

16.   Kong, J., A.M. Cassell, and H.J. Dai, *Chemical vapor deposition of methane for single-walled carbon nanotubes.* Chemical Physics Letters, 1998. **292**(4-6): p. 567-574.

17.   Wei, H., et al., *Carbon Nanotube Circuits: Opportunities and Challenges.* Design, Automation & Test in Europe, 2013: p. 619-624.

18.   Goudah, G., S.M.A. Suliman, and E.A. Elfaki, *Carbon Nanotubes: Challenges and Opportunities.* 2013 International Conference on Computing, Electrical and Electronics Engineering (Icceee), 2013: p. 74-81.

19.   Dai, H.J., *Carbon nanotubes: opportunities and challenges.* Surface Science, 2002. **500**(1-3): p. 218-241.

20.   Yuan, D.N., et al., *Horizontally aligned single-walled carbon nanotube on quartz from a large variety of metal catalysts.* Nano Letters, 2008. **8**(8): p. 2576-2579.

21.   Zhou, W.W., et al., *Synthesis of High-Density, Large-Diameter, and Aligned Single-Walled Carbon Nanotubes by Multiple-Cycle Growth Methods.* Acs Nano, 2011. **5**(5): p. 3849-3857.

22.   Martel, R., et al., *Ambipolar electrical transport in semiconducting single-wall carbon nanotubes.* Physical Review Letters, 2001. **87**(25).

23.   Lin, Y.M., et al., *High-performance dual-gate carbon nanotube FETs with 40-nm gate length.* Ieee Electron Device Letters, 2005. **26**(11): p. 823-825.

24.   Chen, Z.H., et al., *The role of metal-nanotube contact in the performance of carbon nanotube field-effect transistors.* Nano Letters, 2005. **5**(7): p. 1497-1502.

25.   Derycke, V., et al., *Controlling doping and carrier injection in carbon nanotube transistors.* Applied Physics Letters, 2002. **80**(15): p. 2773-2775.

26.   Collins, P.G., et al., *Extreme oxygen sensitivity of electronic properties of carbon nanotubes.* Science, 2000. **287**(5459): p. 1801-1804.

27.   Freitag, M., et al., *Photoconductivity of single carbon nanotubes.* Nano Letters, 2003. **3**(8): p. 1067-1071.

28.   Balasubramanian, K., et al., *Photoelectronic transport imaging of individual semiconducting carbon nanotubes.* Applied Physics Letters, 2004. **84**(13): p. 2400-2402.

29.   Freitag, M., et al., *Imaging of the schottky barriers and charge depletion in carbon nanotube transistors.* Nano Letters, 2007. **7**(7): p. 2037-2042.

30.   Lee, J.U., *Photovoltaic effect in ideal carbon nanotube diodes.* Applied Physics Letters, 2005. **87**(7).

31.   Freitag, M., et al., *Scanning photovoltage microscopy of potential modulations in carbon nanotubes.* Applied Physics Letters, 2007. **91**(3).

32.   Balasubramanian, K., et al., *Photocurrent imaging of charge transport barriers in carbon nanotube devices.* Nano Letters, 2005. **5**(3): p. 507-510.

33.   Barkelid, M., G.A. Steele, and V. Zwiller, *Probing Optical Transitions in Individual Carbon Nanotubes Using Polarized Photocurrent Spectroscopy.* Nano Letters, 2012. **12**(11): p. 5649-5653.

34.   Goze, C., et al., *Elastic and mechanical properties of carbon nanotubes.* Synthetic Metals, 1999. **103**(1-3): p. 2500-2501.

35.   Salvetat, J.P., et al., *Mechanical properties of carbon nanotubes.* Applied Physics a-Materials Science & Processing, 1999. **69**(3): p. 255-260.

36. Hanson, G.W., *Fundamental transmitting properties of carbon nanotube antennas.* Ieee Transactions on Antennas and Propagation, 2005. **53**(11): p. 3426-3435.

37. Wu, Z.C., et al., *Transparent, conductive carbon nanotube films.* Science, 2004. **305**(5688): p. 1273-1276.

38. Kumar, M. and Y. Ando, *Chemical Vapor Deposition of Carbon Nanotubes: A Review on Growth Mechanism and Mass Production.* Journal of Nanoscience and Nanotechnology, 2010. **10**(6): p. 3739-3758.

39. Zhang, Q., et al., *Carbon Nanotube Mass Production: Principles and Processes.* Chemsuschem, 2011. **4**(7): p. 864-889.

40. Chen, J., et al., *Solution properties of single-walled carbon nanotubes.* Science, 1998. **282**(5386): p. 95-98.

41. Zheng, M., et al., *DNA-assisted dispersion and separation of carbon nanotubes.* Nature Materials, 2003. **2**(5): p. 338-342.

42. Gong, K.P., et al., *Nitrogen-Doped Carbon Nanotube Arrays with High Electrocatalytic Activity for Oxygen Reduction.* Science, 2009. **323**(5915): p. 760-764.

43. Fan, Z.J., et al., *A Three-Dimensional Carbon Nanotube/Graphene Sandwich and Its Application as Electrode in Supercapacitors.* Advanced Materials, 2010. **22**(33): p. 3723-+.

44. Slobodian, P., et al., *Multi-wall carbon nanotube networks as potential resistive gas sensors for organic vapor detection.* Carbon, 2011. **49**(7): p. 2499-2507.

45. Li, J., et al., *Carbon nanotube sensors for gas and organic vapor detection.* Nano Letters, 2003. **3**(7): p. 929-933.

46. Robinson, J.A., et al., *Role of defects in single-walled carbon nanotube chemical sensors.* Nano Letters, 2006. **6**(8): p. 1747-1751.

47. Wei, J.Q., et al., *Double-walled carbon nanotube solar cells.* Nano Letters, 2007. **7**(8): p. 2317-2321.

48. Rowell, M.W., et al., *Organic solar cells with carbon nanotube network electrodes.* Applied Physics Letters, 2006. **88**(23).

49. Baughman, R.H., A.A. Zakhidov, and W.A. de Heer, *Carbon nanotubes - the route toward applications.* Science, 2002. **297**(5582): p. 787-792.

50. Lee, N.S., et al., *Application of carbon nanotubes to field emission displays.* Diamond and Related Materials, 2001. **10**(2): p. 265-270.

51. Lee, S.W., et al., *High-power lithium batteries from functionalized carbon-nanotube electrodes.* Nature Nanotechnology, 2010. **5**(7): p. 531-537.

52. Reddy, A.L.M., et al., *Coaxial MnO2/Carbon Nanotube Array Electrodes for High-Performance Lithium Batteries.* Nano Letters, 2009. **9**(3): p. 1002-1006.

53. Dalton, A.B., et al., *Super-tough carbon-nanotube fibres - These extraordinary composite fibres can be woven into electronic textiles.* Nature, 2003. **423**(6941): p. 703-703.

54.   An, K.H., et al., *Electrochemical properties of high-power supercapacitors using single-walled carbon nanotube electrodes.* Advanced Functional Materials, 2001. **11**(5): p. 387-392.

55.   Cao, Q., et al., *Medium-scale carbon nanotube thin-film integrated circuits on flexible plastic substrates.* Nature, 2008. **454**(7203): p. 495-U4.

56.   Shulaker, M.M., et al., *Carbon nanotube computer.* Nature, 2013. **501**(7468): p. 526-+.

57.   Wei, Z.Q., et al., *Nanoscale Tunable Reduction of Graphene Oxide for Graphene Electronics.* Science, 2010. **328**(5984): p. 1373-1376.

58.   Torrisi, F., et al., *Inkjet-Printed Graphene Electronics.* Acs Nano, 2012. **6**(4): p. 2992-3006.

59.   Dean, C.R., et al., *Boron nitride substrates for high-quality graphene electronics.* Nature Nanotechnology, 2010. **5**(10): p. 722-726.

60.   Xia, F.N., et al., *Photocurrent Imaging and Efficient Photon Detection in a Graphene Transistor.* Nano Letters, 2009. **9**(3): p. 1039-1044.

61.   de Abajo, F.J.G., et al., *Graphene Plasmonics.* Fourth International Workshop on Theoretical and Computational Nanophotonics (Tacona-Photonics 2011), 2011. **1398**.

62.   Vakil, A. and N. Engheta, *Transformation Optics Using Graphene.* Science, 2011. **332**(6035): p. 1291-1294.

63.   Blees, M.K., et al., *Graphene kirigami.* Nature, 2015. **524**(7564): p. 204-+.

64.   Zang, J.F., et al., *Multifunctionality and control of the crumpling and unfolding of large-area graphene.* Nature Materials, 2013. **12**(4): p. 321-325.

65.   Rafiee, M.A., et al., *Enhanced Mechanical Properties of Nanocomposites at Low Graphene Content.* Acs Nano, 2009. **3**(12): p. 3884-3890.

66.   Lee, C., et al., *Measurement of the elastic properties and intrinsic strength of monolayer graphene.* Science, 2008. **321**(5887): p. 385-388.

67.   Bolotin, K.I., et al., *Ultrahigh electron mobility in suspended graphene.* Solid State Communications, 2008. **146**(9-10): p. 351-355.

68.   Hedberg, J. *Graphene on Substrate*. 2015 [cited 2018 30 April]; Available from: http://www.jameshedberg.com/scienceGraphics.php?sort=graphene&id=graphene-lattice-onSubstrate-3Dmodel.

69.   Zande, A.v.d., *The Structure and Mechanics of Atomically-Thin Graphene Membranes*. 2011, Cornell University.

70.   Dreyer, D.R., R.S. Ruoff, and C.W. Bielawski, *From Conception to Realization: An Historial Account of Graphene and Some Perspectives for Its Future.* Angewandte Chemie-International Edition, 2010. **49**(49): p. 9336-9344.

71.   Novoselov, K.S., et al., *A roadmap for graphene.* Nature, 2012. **490**(7419): p. 192-200.

72.   Lee, H.C., et al., *Synthesis of Single-layer Graphene: A Review of Recent*

Development. 5th International Conference on Recent Advances in Materials, Minerals and Environment (Ramm) & 2nd International Postgraduate Conference on Materials, Mineral and Polymer (Mamip), 2016. **19**: p. 916-921.

73.   Wu, T.R., et al., *Fast growth of inch-sized single-crystalline graphene from a controlled single nucleus on Cu-Ni alloys.* Nature Materials, 2016. **15**(1): p. 43-+.

74.   Bhaviripudi, S., et al., *Role of Kinetic Factors in Chemical Vapor Deposition Synthesis of Uniform Large Area Graphene Using Copper Catalyst.* Nano Letters, 2010. **10**(10): p. 4128-4133.

75.   Li, X.S., et al., *Large-Area Graphene Single Crystals Grown by Low-Pressure Chemical Vapor Deposition of Methane on Copper.* Journal of the American Chemical Society, 2011. **133**(9): p. 2816-2819.

76.   Hao, Y.F., et al., *The Role of Surface Oxygen in the Growth of Large Single-Crystal Graphene on Copper.* Science, 2013. **342**(6159): p. 720-723.

77.   Farmer, D.B., et al., *Utilization of a Buffered Dielectric to Achieve High Field-Effect Carrier Mobility in Graphene Transistors.* Nano Letters, 2009. **9**(12): p. 4474-4478.

78.   Avouris, P., *Graphene: Electronic and Photonic Properties and Devices.* Nano Letters, 2010. **10**(11): p. 4285-4294.

79.   Bae, S., et al., *Roll-to-roll production of 30-inch graphene films for transparent electrodes.* Nature Nanotechnology, 2010. **5**(8): p. 574-578.

80.   Lin, Y.M., et al., *Wafer-Scale Graphene Integrated Circuit.* Science, 2011. **332**(6035): p. 1294-1297.

81.   Kim, K.S., et al., *Large-scale pattern growth of graphene films for stretchable transparent electrodes.* Nature, 2009. **457**(7230): p. 706-710.

82.   Wang, X., L.J. Zhi, and K. Mullen, *Transparent, conductive graphene electrodes for dye-sensitized solar cells.* Nano Letters, 2008. **8**(1): p. 323-327.

83.   Miao, X.C., et al., *High Efficiency Graphene Solar Cells by Chemical Doping.* Nano Letters, 2012. **12**(6): p. 2745-2750.

84.   Merchant, C.A., et al., *DNA Translocation through Graphene Nanopores.* Nano Letters, 2010. **10**(8): p. 2915-2921.

85.   Garaj, S., et al., *Graphene as a subnanometre trans-electrode membrane.* Nature, 2010. **467**(7312): p. 190-U73.

86.   Schedin, F., et al., *Detection of individual gas molecules adsorbed on graphene.* Nature Materials, 2007. **6**(9): p. 652-655.

87.   Jariwala, D., et al., *Emerging Device Applications for Semiconducting Two-Dimensional Transition Metal Dichalcogenides.* Acs Nano, 2014. **8**(2): p. 1102-1120.

88.   Wang, Q.H., et al., *Electronics and optoelectronics of two-dimensional transition metal dichalcogenides.* Nature Nanotechnology, 2012. **7**(11): p. 699-712.

89.   Chhowalla, M., et al., *The chemistry of two-dimensional layered transition metal dichalcogenide nanosheets.* Nature Chemistry, 2013. **5**(4): p. 263-275.

90.   Radisavljevic, B., et al., *Single-layer MoS2 transistors.* Nature Nanotechnology, 2011. **6**(3): p. 147-150.

91.   Mak, K.F., et al., *Atomically Thin MoS2: A New Direct-Gap Semiconductor.* Physical Review Letters, 2010. **105**(13).

92.   Fleischauer, P.D., *Effects of Crystallite Orientation on Environmental Stability and Lubrication Properties of Sputtered Mos2 Thin-Films.* Asle Transactions, 1984. **27**(1): p. 82-88.

93.   Gacem, K., et al., *High quality 2D crystals made by anodic bonding: a general technique for layered materials.* Nanotechnology, 2012. **23**(50).

94.   Feng, C.Q., et al., *Synthesis of molybdenum disulfide (MoS2) for lithium ion battery applications.* Materials Research Bulletin, 2009. **44**(9): p. 1811-1815.

95.   Yao, Y.G., et al., *High-Concentration Aqueous Dispersions of MoS2.* Advanced Functional Materials, 2013. **23**(28): p. 3577-3583.

96.   Wang, S.S., et al., *Shape Evolution of Monolayer MoS2 Crystals Grown by Chemical Vapor Deposition.* Chemistry of Materials, 2014. **26**(22): p. 6371-6379.

97.   Samad, L., et al., *Layer-Controlled Chemical Vapor Deposition Growth of MoS2 Vertical Heterostructures via van der Waals Epitaxy.* Acs Nano, 2016. **10**(7): p. 7039-7046.

98.   Ling, X., et al., *Role of the Seeding Promoter in MoS2 Growth by Chemical Vapor Deposition.* Nano Letters, 2014. **14**(2): p. 464-472.

99.   Zhan, Y.J., et al., *Large-Area Vapor-Phase Growth and Characterization of MoS2 Atomic Layers on a SiO2 Substrate.* Small, 2012. **8**(7): p. 966-971.

100.   Liu, K.K., et al., *Growth of Large-Area and Highly Crystalline MoS2 Thin Layers on Insulating Substrates.* Nano Letters, 2012. **12**(3): p. 1538-1544.

101.   Wu, S.F., et al., *Vapor-Solid Growth of High Optical Quality MoS2 Monolayers with Near-Unity Valley Polarization.* Acs Nano, 2013. **7**(3): p. 2768-2772.

102.   Kang, K., et al., *High-mobility three-atom-thick semiconducting films with wafer-scale homogeneity.* Nature, 2015. **520**(7549): p. 656-660.

103.   Choi, W., et al., *Recent development of two-dimensional transition metal dichalcogenides and their applications.* Materials Today, 2017. **20**(3): p. 116-130.

104.   Wu, C.C., et al., *Elucidating the Photoresponse of Ultrathin MoS2 Field-Effect Transistors by Scanning Photocurrent Microscopy.* Journal of Physical Chemistry Letters, 2013. **4**(15): p. 2508-2513.

105.   Pu, J., et al., *Highly Flexible MoS2 Thin-Film Transistors with Ion Gel Dielectrics.* Nano Letters, 2012. **12**(8): p. 4013-4017.

106.   Li, H., et al., *Fabrication of Single- and Multilayer MoS2 Film-Based Field-Effect Transistors for Sensing NO at Room Temperature.* Small, 2012. **8**(1): p. 63-67.

107.   Xiao, J., et al., *Exfoliated MoS2 Nanocomposite as an Anode Material for Lithium Ion Batteries.* Chemistry of Materials, 2010. **22**(16): p. 4522-4524.

108. Chang, K. and W.X. Chen, *L-Cysteine-Assisted Synthesis of Layered MoS2/Graphene Composites with Excellent Electrochemical Performances for Lithium Ion Batteries.* Acs Nano, 2011. **5**(6): p. 4720-4728.

109. Kim, S.M., et al., *The effect of copper pre-cleaning on graphene synthesis.* Nanotechnology, 2013. **24**(36).

110. Gardiner, D.J., *Practical Raman spectroscopy.* Springer-Verlag, 1989.

111. Vidano, R.P., et al., *Observation of Raman Band Shifting with Excitation Wavelength for Carbons and Graphites.* Solid State Communications, 1981. **39**(2): p. 341-344.

112. Ferrari, A.C., et al., *Raman spectrum of graphene and graphene layers.* Physical Review Letters, 2006. **97**(18).

113. Li, X.S., et al., *Large-Area Synthesis of High-Quality and Uniform Graphene Films on Copper Foils.* Science, 2009. **324**(5932): p. 1312-1314.

114. Geim, A.K., *Graphene: Status and Prospects.* Science, 2009. **324**(5934): p. 1530-1534.

115. Geim, A.K. and K.S. Novoselov, *The rise of graphene.* Nature Materials, 2007. **6**(3): p. 183-191.

116. Bethune, D.S., et al., *Cobalt-Catalyzed Growth of Carbon Nanotubes with Single-Atomic-Layerwalls.* Nature, 1993. **363**(6430): p. 605-607.

117. Iijima, S. and T. Ichihashi, *Single-Shell Carbon Nanotubes of 1-Nm Diameter (Vol 363, Pg 603, 1993).* Nature, 1993. **364**(6439): p. 737-737.

118. Novoselov, K.S., et al., *Two-dimensional gas of massless Dirac fermions in graphene.* Nature, 2005. **438**(7065): p. 197-200.

119. Novoselov, K.S., et al., *Electric field effect in atomically thin carbon films.* Science, 2004. **306**(5696): p. 666-9.

120. Zhou, X.J., et al., *Band structure, phonon scattering, and the performance limit of single-walled carbon nanotube transistors.* Physical Review Letters, 2005. **95**(14).

121. Balandin, A.A., et al., *Superior thermal conductivity of single-layer graphene.* Nano Letters, 2008. **8**(3): p. 902-907.

122. Pop, E., et al., *Thermal conductance of an individual single-wall carbon nanotube above room temperature.* Nano Letters, 2006. **6**(1): p. 96-100.

123. Peigney, A., et al., *Specific surface area of carbon nanotubes and bundles of carbon nanotubes.* Carbon, 2001. **39**(4): p. 507-514.

124. Peng, L.W., et al., *Transparent, Conductive, and Flexible Multiwalled Carbon Nanotube/Graphene Hybrid Electrodes with Two Three-Dimensional Microstructures.* Journal of Physical Chemistry C, 2012. **116**(8): p. 4970-4978.

125. Tung, V.C., et al., *Low-Temperature Solution Processing of Graphene-Carbon Nanotube Hybrid Materials for High-Performance Transparent Conductors.* Nano Letters, 2009. **9**(5): p. 1949-1955.

126.   Hong, T.K., et al., *Transparent, Flexible Conducting Hybrid Multi layer Thin Films of Multiwalled Carbon Nanotubes with Graphene Nanosheets.* Acs Nano, 2010. **4**(7): p. 3861-3868.

127.   Lin, X.Y., et al., *Development of an ultra-thin film comprised of a graphene membrane and carbon nanotube vein support.* Nature Communications, 2013. **4**.

128.   Nair, R.R., et al., *Fine Structure Constant Defines Visual Transparency of Graphene.* Science, 2008. **320**(5881): p. 1308.

129.   Yan, Z., et al., *Rebar Graphene.* ACS Nano, 2014. **8**(5): p. 5061-5068.

130.   Jarrahi, Z., et al., *Enhanced photoresponse in curled graphene ribbons.* Nanoscale, 2013. **5**(24): p. 12206-12211.

131.   Cao, Y.H., R.L. Flores, and Y.Q. Xu, *Curling graphene ribbons through thermal annealing.* Applied Physics Letters, 2013. **103**(18).

132.   Hong, T., et al., *Thermal and optical properties of freestanding flat and stacked single-layer graphene in aqueous media.* Applied Physics Letters, 2014. **104**(22).

133.   Liang, F., et al., *A Convenient Route to Functionalized Carbon Nanotubes.* Nano Letters, 2004. **4**(7): p. 1257-1260.

134.   Nikolaev, P., et al., *Gas-phase catalytic growth of single-walled carbon nanotubes from carbon monoxide.* Chemical Physics Letters, 1999. **313**(1-2): p. 91-97.

135.   Liang, F., et al., *A convenient route to functionalized carbon nanotubes.* Nano Letters, 2004. **4**(7): p. 1257-1260.

136.   Xu, Y.Q., et al., *Vertical array growth of small diameter single-walled carbon nanotubes.* Journal of the American Chemical Society, 2006. **128**(20): p. 6560-6561.

137.   Tsetseris, L. and S.T. Pantelides, *Graphene nano-ribbon formation through hydrogen-induced unzipping of carbon nanotubes.* Applied Physics Letters, 2011. **99**(14).

138.   Fantini, C., et al., *Optical transition energies for carbon nanotubes from resonant Raman spectroscopy: Environment and temperature effects.* Physical Review Letters, 2004. **93**(14).

139.   Souza, A.G., et al., *Stokes and anti-Stokes Raman spectra of small-diameter isolated carbon nanotubes.* Physical Review B, 2004. **69**(11).

140.   Avouris, P., Z.H. Chen, and V. Perebeinos, *Carbon-based electronics.* Nature Nanotechnology, 2007. **2**(10): p. 605-615.

141.   Xu, X.D., et al., *Photo-Thermoelectric Effect at a Graphene Interface Junction.* Nano Letters, 2010. **10**(2): p. 562-566.

142.   He, X., et al., *Wafer-scale monodomain films of spontaneously aligned single-walled carbon nanotubes.* Nat Nano, 2016. **11**(7): p. 633-638.

143.   Kang, L.X., et al., *Growth of Horizontal Semiconducting SWNT Arrays with Density Higher than 100 tubes/mu m using Ethanol/Methane Chemical Vapor Deposition.* Journal of the American Chemical Society, 2016. **138**(21): p. 6727-6730.

144.   Liu, J., et al., *Chirality-controlled synthesis of single-wall carbon nanotubes using*

vapour-phase epitaxy. Nature Communications, 2012. **3**.

145.   Ding, L., D.N. Yuan, and J. Liu, *Growth of high-density parallel arrays of long single-walled carbon nanotubes on quartz substrates.* Journal of the American Chemical Society, 2008. **130**(16): p. 5428-+.

146.   Vazquez, G., E. Alvarez, and J.M. Navaza, *Surface-Tension of Alcohol Plus Water from 20-Degrees-C to 50-Degrees-C.* Journal of Chemical and Engineering Data, 1995. **40**(3): p. 611-614.

147.   Park, R.S., et al., *Hysteresis in Carbon Nanotube Transistors: Measurement and Analysis of Trap Density, Energy Level, and Spatial Distribution.* Acs Nano, 2016. **10**(4): p. 4599-4608.

148.   Li, H., et al., *From Bulk to Monolayer MoS2: Evolution of Raman Scattering.* Advanced Functional Materials, 2012. **22**(7): p. 1385-1390.

149.   Najmaei, S., et al., *Vapour phase growth and grain boundary structure of molybdenum disulphide atomic layers.* Nature Materials, 2013. **12**(8): p. 754-759.

150.   Splendiani, A., et al., *Emerging Photoluminescence in Monolayer MoS2.* Nano Letters, 2010. **10**(4): p. 1271-1275.

151.   Hong, T., et al., *Plasmonic Hot Electron Induced Photocurrent Response at MoS2-Metal Junctions.* Acs Nano, 2015. **9**(5): p. 5357-5363.

152.   Liu, B.L., et al., *High-Performance Chemical Sensing Using Schottky-Contacted Chemical Vapor Deposition Grown Mono layer MoS2 Transistors.* Acs Nano, 2014. **8**(5): p. 5304-5314.

153.   van der Zande, A.M., et al., *Grains and grain boundaries in highly crystalline monolayer molybdenum disulphide.* Nature Materials, 2013. **12**(6): p. 554-561.

154.   Jeon, J., et al., *Layer-controlled CVD growth of large-area two-dimensional MoS2 films.* Nanoscale, 2015. **7**(5): p. 1688-1695.

155.   Lee, Y.H., et al., *Synthesis and Transfer of Single-Layer Transition Metal Disulfides on Diverse Surfaces.* Nano Letters, 2013. **13**(4): p. 1852-1857.

156.   Lopez-Sanchez, O., et al., *Ultrasensitive photodetectors based on monolayer MoS2.* Nature Nanotechnology, 2013. **8**(7): p. 497-501.

157.   Deng, Y.X., et al., *Black Phosphorus-Monolayer MoS2 van der Waals Heterojunction p-n Diode.* Acs Nano, 2014. **8**(8): p. 8292-8299.

158.   Hong, T., et al., *Anisotropic photocurrent response at black phosphorus-MoS2 p-n heterojunctions.* Nanoscale, 2015. **7**(44): p. 18537-18541.

159.   Roy, K., et al., *Graphene-MoS2 hybrid structures for multifunctional photoresponsive memory devices.* Nature Nanotechnology, 2013. **8**(11): p. 826-830.

160.   Rodin, A.S., A. Carvalho, and A.H. Castro Neto, *Strain-Induced Gap Modification in Black Phosphorus.* Physical Review Letters, 2014. **112**(17).

161.   Li, L.K., et al., *Black phosphorus field-effect transistors.* Nature Nanotechnology, 2014. **9**(5): p. 372-377.

162.   Avouris, P., *Carbon nanotube electronics and photonics.* Physics Today, 2009. **62**(1): p. 34-40.

163.   Avouris, P., M. Freitag, and V. Perebeinos, *Carbon-nanotube photonics and optoelectronics.* Nature Photonics, 2008. **2**(6): p. 341-350.

164.   Gabor, N.M., et al., *Extremely Efficient Multiple Electron-Hole Pair Generation in Carbon Nanotube Photodiodes.* Science, 2009. **325**(5946): p. 1367-1371.

165.   Mizuno, K., et al., *A black body absorber from vertically aligned single-walled carbon nanotubes.* Proceedings of the National Academy of Sciences of the United States of America, 2009. **106**(15): p. 6044-6047.

166.   Wang, R., T. Hong, and Y.Q. Xu, *Ultrathin Single-Walled Carbon Nanotube Network Framed Graphene Hybrids.* Acs Applied Materials & Interfaces, 2015. **7**(9): p. 5233-5238.

167.   Zhang, R.F., et al., *Optical visualization of individual ultralong carbon nanotubes by chemical vapour deposition of titanium dioxide nanoparticles.* Nature Communications, 2013. **4**.

168.   Wang, J.T., et al., *Vapor-Condensation-Assisted Optical Microscopy for Ultralong Carbon Nanotubes and Other Nanostructures.* Nano Letters, 2014. **14**(6): p. 3527-3533.

169.   Ago, H., et al., *Controlled van der Waals Epitaxy of Mono layer MoS2 Triangular Domains on Graphene.* Acs Applied Materials & Interfaces, 2015. **7**(9): p. 5265-5273.

170.   Zhang, W.J., et al., *Ultrahigh-Gain Photodetectors Based on Atomically Thin Graphene-MoS2 Heterostructures.* Scientific Reports, 2014. **4**.

171.   Buscema, M., et al., *The effect of the substrate on the Raman and photoluminescence emission of single-layer MoS2.* Nano Research, 2014. **7**(4): p. 561-571.

172.   Ling, X., et al., *Can Graphene be used as a Substrate for Raman Enhancement?* Nano Letters, 2010. **10**(2): p. 553-561.

173.   Ding, L., et al., *Direct Observation of the Strong Interaction Between Carbon Nanotubes and Quartz Substrate.* Nano Research, 2009. **2**(11): p. 903-910.

174.   Liu, B., et al., *High-Performance Chemical Sensing Using Schottky-Contacted Chemical Vapor Deposition Grown Monolayer MoS2 Transistors.* ACS Nano, 2014. **8**(5): p. 5304-5314.

175.   Trommershauser, J., et al., *Heterogeneous presynaptic release probabilities: functional relevance for short-term plasticity.* Biophys J, 2003. **84**(3): p. 1563-79.

176.   Reyes, A., et al., *Target-cell-specific facilitation and depression in neocortical circuits.* Nat Neurosci, 1998. **1**(4): p. 279-85.

177.   Markram, H., Y. Wang, and M. Tsodyks, *Differential signaling via the same axon of neocortical pyramidal neurons.* Proc Natl Acad Sci U S A, 1998. **95**(9): p. 5323-8.

178.   Clare, J.J., *Targeting Ion Channels for Drug Discovery.* Discovery Medicine, 2010. **46**: p. 253-260.

179.   Novak, P., et al., *Nanoscale-Targeted Patch-Clamp Recordings of Functional*

Presynaptic Ion Channels. Neuron, 2013. **79**(6): p. 1067-1077.

180.   Carlson, G.C. and D.A. Coulter, *In vitro functional imaging in brain slices using fast voltage-sensitive dye imaging combined with whole-cell patch recording.* Nature Protocols, 2008. **3**(2): p. 249-255.

181.   Chen, T.W., et al., *Ultrasensitive fluorescent proteins for imaging neuronal activity.* Nature, 2013. **499**(7458): p. 295-+.

182.   Hogberg, H.T., et al., *Application of micro-electrode arrays (MEAs) as an emerging technology for developmental neurotoxicity: Evaluation of domoic acid-induced effects in primary cultures of rat cortical neurons.* Neurotoxicology, 2011. **32**(1): p. 158-168.

183.   Patolsky, F., et al., *Detection, stimulation, and inhibition of neuronal signals with high-density nanowire transistor arrays.* Science, 2006. **313**(5790): p. 1100-1104.

184.   Duan, X.J., et al., *Intracellular recordings of action potentials by an extracellular nanoscale field-effect transistor.* Nature Nanotechnology, 2012. **7**(3): p. 174-179.

185.   Traversi, F., et al., *Detecting the translocation of DNA through a nanopore using graphene nanoribbons.* Nature Nanotechnology, 2013. **8**(12): p. 939-945.

186.   Mannoor, M.S., et al., *Graphene-based wireless bacteria detection on tooth enamel.* Nature Communications, 2012. **3**.

187.   Lee, C., et al., *Measurement of the elastic properties and intrinsic strength of monolayer graphene.* Science, 2008. **321**(5887): p. 385-8.

188.   Kuzum, D., et al., *Transparent and flexible low noise graphene electrodes for simultaneous electrophysiology and neuroimaging.* Nature Communications, 2014. **5**.

189.   Bae, S., et al., *Roll-to-roll production of 30-inch graphene films for transparent electrodes.* Nat Nanotechnol, 2010. **5**(8): p. 574-8.

190.   Park, D.W., et al., *Graphene-based carbon-layered electrode array technology for neural imaging and optogenetic applications.* Nature Communications, 2014. **5**.

191.   Ferrari, A.C. and D.M. Basko, *Raman spectroscopy as a versatile tool for studying the properties of graphene.* Nature Nanotechnology, 2013. **8**(4): p. 235-246.

192.   Shi, M.J., et al., *Glia co-culture with neurons in microfluidic platforms promotes the formation and stabilization of synaptic contacts.* Lab on a Chip, 2013. **13**(15): p. 3008-3021.

193.   Cohen-Karni, T., et al., *Graphene and nanowire transistors for cellular interfaces and electrical recording.* Nano Lett, 2010. **10**(3): p. 1098-102.

194.   Gao, Y., et al., *A versatile valve-enabled microfluidic cell co-culture platform and demonstration of its applications to neurobiology and cancer biology.* Biomed Microdevices, 2011. **13**(3): p. 539-48.

195.   Majumdar, D., et al., *Co-culture of neurons and glia in a novel microfluidic platform.* J Neurosci Methods, 2011. **196**(1): p. 38-44.

196.   Li, X., et al., *Large-area synthesis of high-quality and uniform graphene films on*

copper foils. Science, 2009. **324**(5932): p. 1312-1314.

197.   Xu, Y.Q., A. Barnard, and P.L. McEuen, *Bending and Twisting of Suspended Single-Walled Carbon Nanotubes in Solution.* Nano Letters, 2009. **9**(4): p. 1609-1614.

198.   Mueller, T., et al., *Role of contacts in graphene transistors: A scanning photocurrent study.* Physical Review B, 2009. **79**(24).

199.   Zhang, Y., et al., *Probing electrical signals in the retina via graphene-integrated microfluidic platforms.* Nanoscale, 2016.

200.   Das Sarma, S., et al., *Electronic transport in two-dimensional graphene.* Reviews of Modern Physics, 2011. **83**(2): p. 407-470.

201.   Xia, J.L., et al., *Measurement of the quantum capacitance of graphene.* Nature Nanotechnology, 2009. **4**(8): p. 505-509.

202.   Ramnath, R.R., K. Strange, and P.A. Rosenberg, *Neuronal Injury Evoked by Depolarizing Agents in Rat Cortical Cultures.* Neuroscience, 1992. **51**(4): p. 931-939.

203.   Schramm, M., S. Eimerl, and E. Costa, *Serum and Depolarizing Agents Cause Acute Neurotoxicity in Cultured Cerebellar Granule Cells - Role of the Glutamate Receptor Responsive to N-Methyl-D-Aspartate.* Proceedings of the National Academy of Sciences of the United States of America, 1990. **87**(3): p. 1193-1197.

204.   Takahashi, M., S.Y. Liou, and M. Kunihara, *Ca2+-Dependent and Cl--Dependent, Nmda Receptor-Mediated Neuronal Death Induced by Depolarization in Rat Hippocampal Organotypic Cultures.* Brain Research, 1995. **675**(1-2): p. 249-256.

205.   Rothman, S.M., *The Neurotoxicity of Excitatory Amino-Acids Is Produced by Passive Chloride Influx.* Journal of Neuroscience, 1985. **5**(6): p. 1483-1489.

206.   Zhang, Y.C., et al., *Probing electrical signals in the retina via graphene-integrated microfluidic platforms.* Nanoscale, 2016. **8**(45): p. 19043-19049.

207.   Randin, J.P. and E. Yeager, *Differential Capacitance Study of Stress/Annealed Pyrolytic Graphite Electrodes.* Journal of the Electrochemical Society, 1971. **118**(5): p. 711-&.